

# Advanced 3D Monte Carlo Algorithms for Biophotonic and Medical Applications

Lewis McMillan



University of  
St Andrews

This thesis is submitted in partial fulfillment for the degree of  
PhD  
at the  
University of St Andrews

August 2019



# Declaration

I, Lewis McMillan, hereby certify that this thesis, which is approximately 34832 words in length, has been written by me, that it is the record of work carried out by me, or principally by myself in collaboration with others as acknowledged, and that it has not been submitted in any previous application for a higher degree.

I was admitted as a research student in September 2015 and as a candidate for the degree of PhD in September 2015; the higher study for which this is a record was carried out in the University of St Andrews between 2015 and 2019.

Date ..... Signature of candidate .....

I hereby certify that the candidate has fulfilled the conditions of the Resolution and Regulations appropriate for the degree of PhD in the University of St Andrews and that the candidate is qualified to submit this thesis in application for that degree.

Date ..... Signature of supervisor .....

Date ..... Signature of supervisor .....



# Abstract

The Monte Carlo radiation transfer (MCRT) method can simulate the transport of light through turbid media. MCRT allows the simulation of multiple anisotropic scattering events, as well as a range of microphysics such as polarisation, and fluorescence. This thesis concerns the development of several MCRT algorithms to solve various biophotonic and medical problems. Modelling of tissue ablation, autofluorescent signals, and a theoretical quasi-wave/particle MCRT model were developed as part of this thesis.

Tissue ablation can be used to treat acne scarring and Rhinophyma, it can also be used to help enhance topical drug delivery. Currently depth of ablation is not easily elucidated from a given laser or laser power setting. Therefore, a numerical tissue ablation model is developed using MCRT, a heat diffusion model, and a numerical tissue damage model to assess ablation crater depth and thermal damage to the surrounding tissue.

Autofluorescence is the natural fluorescence of biological structures in tissue. Autofluorescence can be used as a biomarker of several diseases including: cardiovascular diseases, Alzheimers and diabetes. However, the origin of the signal is not completely clear. The effect of tissue optics on the signal, which fluorophores contribute to the signal and by how much, and how different locations on the body can effect the signal are all not well understood. This thesis presents a study of the effect of tissue optics on the autofluorescent signal. As part of this study AmoebaMCRT was created to determine the relative concentrations of fluorophores for a given autofluorescent signal.

Finally, we developed an extension to the MCRT method that allows the simulation of quasi-wave/particles. This method relies on the Huygens-Fresnel principle and the tracking of the phase of each individual photon packet. The extension,  $\varphi$ MC, allows the modelling of complex beams that require the wave properties of light such as arbitrary order Bessel beams, and Gaussian beams. We then use  $\varphi$ MC to predict which beam, Bessel or Gaussian, preforms “better” in a highly turbid medium.



# Acknowledgements

First of all, thank you to Tom and Kenny for allowing me the opportunity to undertake this PhD and for all their support and encouragement over the course of my thesis. If it weren't for you both keeping me on the straight and narrow I'm sure I would still be coding instead of writing. I also swear my code is now bug free...

Thank you to Ian for getting me access to Wardlaw and Kennedy computer clusters. Most of this work wouldn't be possible without it.

Thank you to Isla for answering all my stupid questions over the past three years, and for being a good source of moral support. Thank you also for allowing me to be a part of code and cake, which I thoroughly enjoyed, both the baking and the talks.

Thank you to all at Ninewells for making me feel welcome every time I took up space in your research office. Especially thank you to Luke, Paul, and Ewan for letting me collaborate with you, and for your good company at the conferences we attended together.

McConnells

Thank you to my family for your support throughout my last nine years at St Andrews.

Kathleen smells

For Lil and Marion.

# Contents

<b>Declaration</b>	iii
<b>Abstract</b>	v
<b>Acknowledgements</b>	vii
<b>Abbreviations</b>	xi
<b>List of Figures</b>	xv
<b>1 Introduction</b>	1
1.1 Monte Carlo Method . . . . .	2
1.2 Synopsis and Thesis Objectives . . . . .	4
<b>2 Monte Carlo Radiation Transport Technique</b>	7
2.1 Introduction . . . . .	7
2.2 Monte Carlo Radiation Transport Algorithm . . . . .	7
2.2.1 Introduction and Background . . . . .	7
2.2.2 Optical Properties . . . . .	11
2.2.3 MCRT Algorithm . . . . .	15
2.2.4 Code Details . . . . .	20
2.3 Validation of MCRT Code . . . . .	23
2.4 Conclusion . . . . .	24
<b>3 Computational Modelling of Tissue Ablation</b>	25
3.1 Introduction and Background . . . . .	25
3.2 Methods . . . . .	26
3.2.1 Monte Carlo radiation transport (MCRT) . . . . .	26
3.2.2 Heat Transport . . . . .	27
3.2.3 Tissue Damage . . . . .	33
3.2.4 Validation . . . . .	36
3.3 <i>In silico</i> results . . . . .	38
3.3.1 Introduction . . . . .	38
3.3.2 Results . . . . .	39
3.4 Application of Model for Spy Disposal . . . . .	47
3.5 Conclusion . . . . .	48
<b>4 Quasi-wave/particle Monte Carlo Algorithm, <math>\varphi MC</math></b>	51
4.1 Introduction . . . . .	51

4.2	Theory . . . . .	52
4.2.1	Complex Phase Tracking . . . . .	52
4.2.2	Huygens-Fresnel Principle . . . . .	53
4.2.3	Validation of Phase Tracking Algorithm . . . . .	55
4.3	Gaussian Beams . . . . .	59
4.4	Bessel Beams . . . . .	62
4.4.1	Theory . . . . .	63
4.4.2	Validation . . . . .	64
4.5	Higher Order Bessel Beams . . . . .	70
4.6	Comparison . . . . .	73
4.6.1	Discussion . . . . .	76
4.7	Conclusion . . . . .	77

# Abbreviations

$T_a$  ablation temperature.

**AMR** adaptive mesh refinement.

**BPM** beam propagation methods.

**BPM** beam propagation method.

**CDF** cumulative distribution function.

**FDM** finite difference method.

**FDTD** finite difference time domain.

**HOBBs** higher order Bessel beams.

**K-M theory** Kubelka-Munk theory.

**MCRT** Monte Carlo radiation transfer.

**MPI** Message-passing interface.

**OCT** optical coherence tomography.

**PDF** probability density function.

**PDT** photo-dynamic therapy.

**PSTD** pseudo-spectral time-domain.

**RTE** radiative transfer equation.

# List of Figures

- 1.1 Sample Buffon needle experiment. 100 needles are dropped on a  $10 \times 10$  cm area with lines spaced 1.5 cm apart. If a needle lands on a line it is recorded and coloured blue, else it is red. This simulation gave a value of  $\pi \approx 3.10$ .
- 1.2 Illustration of the rejection method for determining  $\pi$  from the area of a circle inscribed within a square. The ratio of the area of the circle to the square is  $\frac{\pi}{4}$ . Thus the ratio of darts landing in the circle to those that land outside the circle is  $\pi \approx \frac{4N_{inner}}{N_{total}}$ , where  $N_{total}$  is the total number of darts, and  $N_{inner}$  is the total number of darts that land in the circle. Using 200 darts gave a value of  $\pi \approx 3.12$ .
- 1.3 Example of randomly sampling from a spectrum. Figure shows 100 random samples drawn to recreate a solar spectrum.
- 1.4 Computer generated imagery using ray tracing. The Monte Carlo method is used to “compute radiance along ray paths between lights and the camera”, to generate CGI images [29].
- 2.1 Energy flow through area  $dA$  within solid angle  $d\Omega$  in a direction  $\hat{s}$ . Adapted from [33, 34].
- 2.2 Cylindrical volume element,  $ds \, dA$ , with solid angle  $d\Omega$  in direction  $\hat{s}$  and solid angle  $d\Omega'$  in direction  $\hat{s}'$ . Energy flowing through this element is used to derive the radiation transfer equation. Adapted from [33, 34].
- 2.3 Figure shows the g factor for the Henyey-Greenstein phase function, for various configurations of back, forward or isotropic scattering. Arrow indicates the photons initial direction before scattering.
- 2.4 Examples of wavelength dependent absorption coefficients for some common tissue chromophores [45, 49–57].
- 2.5 Flowchart of the Monte Carlo radiation transport algorithm as described in this section.
- 2.6 Example of a possible voxel model, with three different layers, various holes due to ablative pixel beam lasers ( see Chapter 3). Each voxel can represent a different optical/thermal property of the tissue medium.
- 2.7 Illustration of photon propagation through a 2D grid.  $d_{x1}$ , and  $d_{y1}$  are the distances to the voxel walls in the x and y directions in the  $\mu_1$  voxel. In this case  $S_1 = d_{x1}$  as  $d_{x1}$  is smaller than  $d_{y1}$ , thus the photon hits the voxel wall in the  $x$  direction. For the  $\mu_5$  voxel,  $d_y$  is smaller, thus the photon hits the voxel wall in the  $y^{th}$  direction.
- 2.8 Illustration of rotating the centre of mass frame to the lab frame.  $\mathbf{n}$  is the direction vector of the photon before scattering, and  $\mathbf{n}_s$  is the scattered direction vector.  $\theta$  and  $\varphi$  are the scattering angles.  $z_s$  is in the same direction as  $\mathbf{n}$ .

- 2.9 Source code hierarchy, showing the relationship between different modules. Green is the entry point for the simulation. Red are the data modules, light blue are the routine modules, and grey are the external dependencies.
- 2.10 Performance of the parallelisation of the MCRT code using MPI.
- 2.11 Figure shows the fluence as a function of depth. Figure also shows comparison to the Jacques MCRT simulation and the MCRT as described in this chapter.
- 3.1 Flowchart of the tissue ablation algorithm.
- 3.2 Red lines are packet paths within a voxel. Black lines packet paths out with the voxel. Red packet paths, weighted by  $\mu_a$ , are summed up to calculate the absorbed energy within each voxel.
- 3.3 Finite difference method stencil for simple explicit scheme.
- 3.4 Computational domain decomposition. Total computational domain (red outline) is evenly divided between cores in the CPU. This is done via layers of the domain in the z direction. Information is passed to/from cores via the “halo swap” process (see Fig. 3.5).
- 3.5 Halo swapping. Process A updates the area in red and blue on the left. It updates the blue area which is sent to process B as B’s “halo”. Process B cannot update its own halo, but rather updates the halo for process A.
- 3.6 Figure shows the speed up gained by parallelisation of the heat simulation using the “halo swapping” technique, for various sizes of computational domain (voxels). Data taken from a Intel Xeon E3-1245 v5, 8 cores @ 3.5GHz machine.
- 3.7 Ablation of a dog aorta, as viewed under a microscope. Steam vacuoles are clearly visible on either side of the ablation area. Carbonisation is also evident at the edges of the ablation fronts. Adapted from [81].
- 3.8 Temperature profiles of the cube for various times, comparing between analytical solution and numerical method.
- 3.9 Simulation of 81 pixel beams. Figure a) shows a slice through the optical properties at the end of the simulation in the z-y plane. Figure b) shows the optical properties in the x-y plane at the top surface. Yellow is unchanged tissue, and purple is completely ablated tissue. Figure shows that the ablation craters do not overlap one another.
- 3.10 Simulation of 70 W CO<sub>2</sub> ablative laser, with a circular beam profile. Crater depths as a function of pixel beam energy for various ablation temperature ( $T_a$ )’s.
- 3.11 Simulation of 70 W CO<sub>2</sub> ablative laser, with a Gaussian beam profile. Crater depths as a function of pixel beam energy for various  $T_a$ ’s.
- 3.12 Temperature bore hole through centre of medium as a function of time, for  $T_a=500\text{ }^{\circ}\text{C}$ . Laser power is also plotted for comparison.
- 3.13 Figure shows the maximum horizontal extent of thermal damage as a function of energy per pixel beam, for different  $T_a$ ’s.
- 3.14 Tissue thermal damage around the ablation crater (white). Thermal tissue damage values of 3 refer to 3<sup>rd</sup> degree burns, 2 to 2<sup>nd</sup>, and 1 to 1<sup>st</sup> degree burns respectively. P is the power in Watts,  $T_a$  is the ablation temperature in Kelvin, and  $E_p$  is the energy per pixel beam in mJ.
- 3.15 Figure show the time taken for 1<sup>st</sup>, 2<sup>nd</sup>, and 3<sup>rd</sup> to occur as a function of depth, for a range of  $T_a$ ’s at 400 mJ.
- 3.16 Figure show the time taken for 1<sup>st</sup>, 2<sup>nd</sup>, and 3<sup>rd</sup> to occur as a function of depth, for a range of  $T_a$ ’s at 50 mJ.
- 3.17 Comparison of the different pulse profiles trialled for a pulselength of 0.2 s.

- 3.18 Comparison of various pulse shapes for the pixel beams. Figure shows ablation depths for  $T_a=500\text{ }^{\circ}\text{C}$ .
- 3.19 Comparison of ablation depths for different initial temperatures in porcine skin.
- 3.20 Comparison of maximum horizontal damage distance for different initial porcine skin temperatures.
- 3.21 Comparison of different voxel temperatures after ablation. Half refers to setting the temperature of a voxel to half that of the ablation temperature. Room refers to room temperature, and ablation leaves the temperature at the ablation temperature.
- 3.22 Still image of the iconic laser scene in the film Goldfinger. Copyrights Eon Productions.
  
- 4.1 Example of phase calculation when a photon has travelled a distance  $l$ . The figure also shows an example of interference between two photons via addition of the complex amplitudes at the point  $P_0$ .
- 4.2 Illustration of the Huygens-Fresnel principle. At  $t_0$  a wave is incident on an aperture. Times  $t_1$ ,  $t_2$ , and  $t_3$  show the evolution of the wavefront using the Huygens-Fresnel principle. Dashed lines illustrate the wavefront position at the previous time step, and is the source of the Huygens-Fresnel wavelets.
- 4.3 Comparison of theory and simulation for the double slit experiment. Top image shows a slice through the computed image and the expected profile from theory. For clarity only every 5<sup>th</sup> MCRT data point is plotted. Bottom image shows the computed image.
- 4.4 Geometry of the square aperture used in the validation.
- 4.5 Comparison of theory and simulation for diffraction through a square aperture in the Fresnel and Fraunhofer regimes.
- 4.6 Illustration of a Gaussian beam focusing to its waist then diverging away. Image shows the various defined properties of a Gaussian beam along side the radius of curvature changing direction at the waist.
- 4.7 Simulation setup of focusing a Gaussian beam through a lens. Lens is convex-plano and is modelled on ThorLabs LA4249 UV fused silica lens [136].  $L_t$  is the lens thickness,  $D$  is the  $\frac{1}{e^2}$  input beam diameter,  $W_d$  is the working distance or back focal length,  $2 \cdot z_{max}$  is the depth of the medium, and  $w_0$  is the beam waist.
- 4.8 Results of *in-silico* experiment of focusing a Gaussian beam though a convex-plano lens.
- 4.9 Slice through the real part of the complex electric field of the *in-silico* experiment as in Fig. 4.7. Figure shows the radius of curvature changing direction at the waist as predicted by theory.
- 4.10 Illustration of  $\varphi MC$ 's ability to model spherical aberrations. Top image generated using same setup as in Fig. 4.7, but with  $D = 1.5\text{ mm}$  within  $\varphi MC$ . Image shows the elongated focus and characteristic interference pattern behind the focus. Bottom image shows illustration of rays traced through a lens which suffers from spherical aberration.
- 4.11 Geometry of a Bessel beam, generated by an axicon lens.  $\beta$  is the angle with the optical axis, and the angle of the conical waves.  $\alpha$  is the axicon angle.
- 4.12 Comparison of theoretical and MCRT simulation of a Bessel beams, with intensity normalised. The results from  $\varphi MC$  show good agreement with the theory.
- 4.13 Bessel beam in the far field. Bessel beams in the far field becomes a ring beam. Image shows a slice of intensity through the medium.

- 4.14 Illustration of the Bessel beams self-healing property. Highly absorbing cube placed near the top of the medium. Figure shows that the Bessel beam forms further down the optical axis. a) shows side on view with the obstacle at 0.02 mm, b) shows top down view at surface of the simulated b=medium before the obstacle, c) shows top down view in the middle of the obstacle, and d) shows the top down view after the Bessel beam has “healed”.
- 4.15 Experimental set-up for propagating a Bessel beam through a cuvette filled with varying concentrations of Intralipid 20%. Bessel beam is imaged by an 20 $\times$  objective lens and a Grasshopper 3 camera.
- 4.16 Scattering properties of 20% Intralipid [151].
- 4.17 Comparison of experimental and simulation data for propagation of a Bessel beam produced by an axicon, through mediums of various turbidity. Images a) to g) is the data from  $\varphi MC$ , and h) to n) are the experimental data. Volumes along the top are the volume of Intralipid in each solution as in Table 4.1. All images are cropped so they are the same size and normalised to the maximum value in each image.
- 4.18 Line graph plots of slices taken through the generated and experimental images as shown in Fig. 4.17.
- 4.19 Comparison of a larger medium, 2 mm<sup>3</sup> versus that of a smaller medium, 0.5 mm  $\times$  0.5 mm  $\times$  2.00 mm. The figure shows that the smaller medium gives a better signal to noise ratio, whilst still accurately modelling the experiment.
- 4.20 Helical delay element attached to an axicon. The Axicon introduces a radial delay in addition to that of the helical element. If the input beam is a Gaussian, the output beam is a higher order Bessel beam,  $l > 0$ .
- 4.21 Higher order Bessel beams (HOBBS). a) to d) show the phase shift due to the helical element. e) to h) show line plots of the simulation data compared to the theory. i) to l) and m) to p) show the higher order Bessel beam images for theory and simulation data respectively.
- 4.22 First comparison of Bessel and Gaussian beams with equal power used to generate both beams. Plots taken at the Gaussian beams focus. The maxima at the sides of the Gaussian beam in the 0.0 $\mu$ L plot are due to simulation effects, mainly the small size of the medium not allowing photons from further off the optical axis to interfere destructively.
- 4.23 First comparison of Bessel and Gaussian beams, with equal power used to generate both beams. Plots taken at the bottom of the simulated medium.
- 4.24 Second comparison of Bessel and Gaussian beams for the case where the power given to each beam, yields the same maximum at the Gaussian beams focus. These plots are taken from the Gaussian beams focus.
- 4.25 Comparisons of unequal powered beams at the bottom of scattering medium.
- 4.26 Illustration of how a Bessel beam becomes degraded due to scattering. Top image shows how two photons propagate through the axicon and constructively interfere to produce a Bessel beams. Bottom image shows how scattering can affect this process.



# Chapter 1

## Introduction

This thesis is concerned with the development of several Monte Carlo radiation transfer (MCRT) algorithms for biophotonic and medical applications. The MCRT method allows the simulation of light propagation through turbid medium whilst undergoing multiple anisotropic scattering, absorption and a range of other micro-physics (see Chapter 2 for full discussion of the theory). MCRT was invented at the end of WW II for the purpose of calculating the paths of neutrons through various media [1–4]. As the codes developed around this period focused on modelling the transport of protons, gamma rays and other nuclear particles, it was a small leap to modelling the dose received by a patient undergoing radiation therapy [5]. However, the jump to modelling light transport in skin would take a further two decades [6], and another decade until it became popular and the *de-facto* gold standard in light tissue interaction modelling [7,8]. It has since been used to optimise photo-dynamic therapy, quantifying DNA damage from UV light sources, and modelling treatment of port wine stain removal amongst various other medical treatments and diagnoses methods [9–11]. The real power of the MCRT method is that it allows the tailoring of the model to the patient. This means that medical treatment can be personalised to each individual patient rather than an average corpus of patients.

Personalised medicine entails having fine grained knowledge of the patient down to the genome level, to understand how various drugs or treatments will affect the patient. One particular area of research in personalised medicine is into the so called “digital twin”. A digital twin as defined by A. El Saddik as [12]:

“... is a digital replica of a living or non-living physical entity.”

Digital twins are currently heavily used in engineering to predict when various machinery will need to undergo maintenance. Digital twins operate by modelling their physical counterpart. This model is updated via information from their physical counterpart which allows the digital twin to predict its physical counterparts future behaviour. Companies like Phillips use this in their MRI machines to help schedule downtime, and predict which parts the engineer will need on site, both of which minimises the downtime of the machine which is import for the hospital/clinic [13].

At the heart of the digital twin method, is the ability to accurately model the object or living thing being studied. This can be straightforward when the twin in question is a machine, as sensors can usually be attached to the various components to get feed back on the machine’s operation. Machines also have the bonus of (normally) being well understood so that modelling them is usually relatively straightforward. However, this is not as easy when dealing with living

systems. First, we still do not have a complete understanding of the biology within humans. Therefore, modelling a human accurately is not possible as various assumptions and approximations have to be made. Second, to get accurate information on what is happening inside a patient, generally either ionising radiation needs to be used, or cameras inserted into the patient. Both of these cannot be done for indefinite periods without causing harm or discomfort. Therefore, continuous information on the inner functions of the body is not possible. One area where information is more readily available is the skin. Information on the skin function or dysfunction is normally diagnosed with light. Light is also used in various treatments such as photodynamic therapy and tissue ablation, over various internal and external sites on the body. Light's interaction over the whole spectrum, from the UV to the infrared, is readily modelled with techniques such as MCRT. MCRT allows a digital twin model of the individual patient skin to be simulated. This can then be used to tailor treatment regimes for the individual patient, or to predict treatment outcomes for specific patients. The use of simulation techniques like MCRT allow testing *in-silico*, and can negate the need to test on humans or animals. MCRT is already heavily used to plan radiation therapy treatments [14, 15], though this has yet make the leap to light-tissue interaction modelling.

## 1.1 Monte Carlo Method

The Monte Carlo method is a numerical analysis technique based upon random numbers, which are used to calculate unknown variables in problems [16, 17].

The earliest use of the method is in Buffon's needle experiment of the 18<sup>th</sup> century [18–20]. Buffon asked the question;

"Suppose we have a floor made of parallel strips of wood, each the same width, and we drop a needle onto the floor. What is the probability that the needle will lie across a line between two strips?"

The solution to this question is: for a needle length  $l$ , strip separation  $s$ , where  $x$  is the distance from the needle to the closest line, and  $\theta$  is the angle of the needle with respect to the wood strips. Then using a simple geometrical argument, a needle crosses a strip if  $x \leq \frac{l}{2} \sin\theta$ .

$x$  is distributed uniformly in  $[0, \frac{s}{2}]$ , and  $\theta$  in  $[0, \frac{\pi}{2}]$ . Therefore the probability density function for  $x$  is  $p(x) = \frac{2}{s}$ , and  $\theta$  is  $p(\theta) = \frac{2}{\pi}$ . The probability density function (PDF), is a function of a variable that gives the probability for a variable to take a given value. The PDF is normalised over the whole range of the variable, in this case  $x$ , and  $\theta$ . Thus, as  $x$  and  $\theta$  are independent variables, giving a joint probability of  $p(x, \theta) = \frac{4}{s\pi}$ . So the probability of a needle of length  $l$  crossing a line ( $l < s$ ) is:

$$P = \int_0^{\frac{\pi}{2}} \int_0^{\frac{l}{2} \sin\theta} \frac{4}{s\pi} dx d\theta = \frac{2l}{s\pi} \quad (1.1)$$

Equation (1.1) can be used to carry out a Monte Carlo estimation of  $\pi$ . A simple rearrangement yields:  $\pi = \frac{2l}{sP}$  where  $P$  is the ratio of needles crossing the line to the total number dropped. Laplace was the first to suggest that Buffon's needle experiment could be used to estimate  $\pi$  [19]. Figure 1.1 shows an example of a simulation of Buffon's needle experiment.

There are various different approaches to using the Monte Carlo method to obtain randomly sampled variables. One analytical way of achieving this is the inverted sampling method. The inverted sampling method can be summarised by the following steps for drawing a sample  $X_i$  from an arbitrary PDF  $p(x)$ :

1. Compute the cumulative distribution function (CDF)  $P(x) = \int_0^x p(x')dx'$

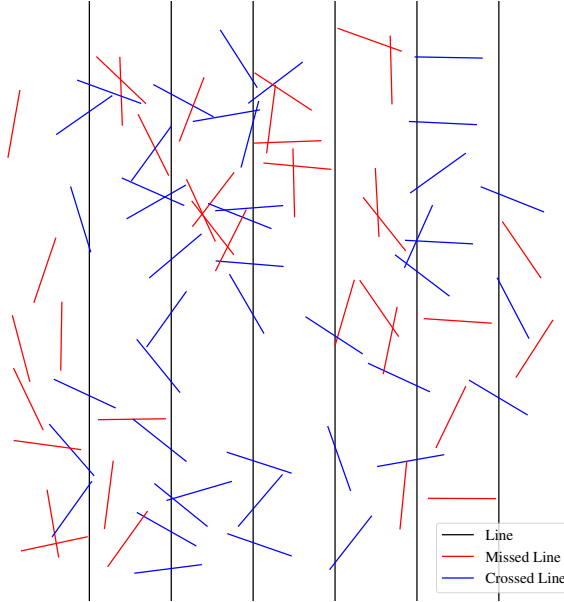


**Figure 1.1:** Sample Buffon needle experiment. 100 needles are dropped on a  $10 \times 10$  cm area with lines spaced 1.5 cm apart. If a needle lands on a line it is recorded and coloured blue, else it is red. This simulation gave a value of  $\pi \approx 3.10$ .

2. Compute the inverse  $P^{-1}(x)$
3. Obtain a uniformly distributed random number  $\xi$  in the range  $[0.,1.)$
4. Finally, compute  $X_i = P^{-1}(\xi)$

If a given problem cannot use the inverted sampling method, as it may not be possible to get a PDF or analytically invert the CDF, then the rejection method can be used. The rejection method is essentially a dart throwing method. This means that points are randomly chosen and compared to the function. If the point lies under the function then the point is accepted, if it lies above the function then it is rejected. For example, if a function,  $f(x)$  that does not have an analytical PDF, we can use a PDF  $p(x)$  such that  $f(x) < cp(x)$  where  $c$  is a constant. Therefore sampling from  $p(x)$ , and if the sampled point lies under  $f(x)$  it is accepted, else it is rejected. Figure 1.2 shows an example of this process.

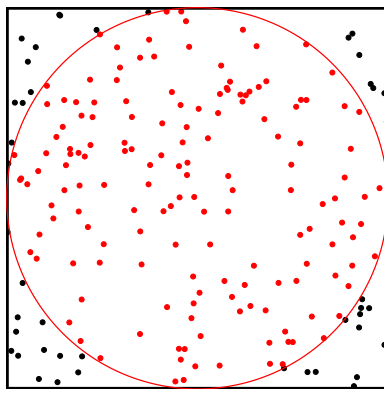


**Figure 1.2:** Illustration of the rejection method for determining  $\pi$  from the area of a circle inscribed within a square. The ratio of the area of the circle to the square is  $\frac{\pi}{4}$ . Thus the ratio of darts landing in the circle to those that land outside the circle is  $\pi \approx \frac{4N_{inner}}{N_{total}}$ , where  $N_{total}$  is the total number of darts, and  $N_{inner}$  is the total number of darts that land in the circle. Using 200 darts gave a value of  $\pi \approx 3.12$

One common use of the Monte Carlo method, is to randomly sample from a spectrum. To generate a random sample from a spectrum, first the CDF of the spectrum must be calculated. This is done by first normalising the PDF, where the PDF in this case is the spectrum itself. It is normalised such that the sum of the PDF is unity. The CDF is then just the cumulative sum of the PDF. Then using the above method as described above, a random number is drawn,  $\xi$ , and the bracketing values in the CDF are found. We then interpolate to get the x value corresponding to  $\xi$ . Figure 1.3 shows the result of this process for  $5 \times 10^6$  random samples.

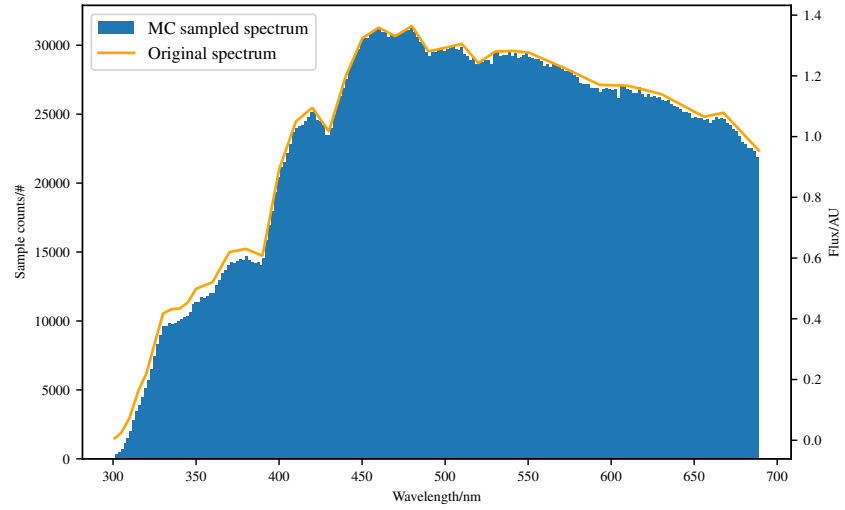


**Figure 1.3:** Example of randomly sampling from a spectrum. Figure shows 100 random samples drawn to recreate a solar spectrum.

The Monte Carlo method is used in various different disciplines. Ranging from use in the financial sector to analyse investments and stocks by simulating the sources of uncertainty which affect their values [21, 22], use in statistical analysis [23], and in modern computer generated images (see Fig. 1.4) [24, 25]. It is also widely used in astronomy [26, 27] and medicine [11, 28], to simulate the propagation of radiation through scattering (turbid) media. This technique, Monte Carlo radiation transfer (MCRT), is what makes up the bulk of this thesis and is described in depth in the following sections.

## 1.2 Synopsis and Thesis Objectives

Chapter 2 details the MCRT method that is used for the bulk of this thesis. Presented in this chapter is the theory behind the MCRT method along with why it is considered the *de-facto* standard in light-tissue interaction modelling. This chapter also presents a discussion on how the MCRT method is translated into code. Details of speed up techniques such as parallelisation are also presented. Finally, to ensure that the code is accurate, it is validated against another MCRT code.

Chapter 3 details the tissue ablation model developed as part of this thesis. The tissue ablation model was created to predict the depth of ablation craters in tissue for a given laser power. The model could also be used to help optimise treatment regimes in cosmetic and medical procedures. The numerical tissue ablation model consists of 3 numerical methods: MCRT to model the light transport in the tissue, numerical heat model to model the heat diffusion within

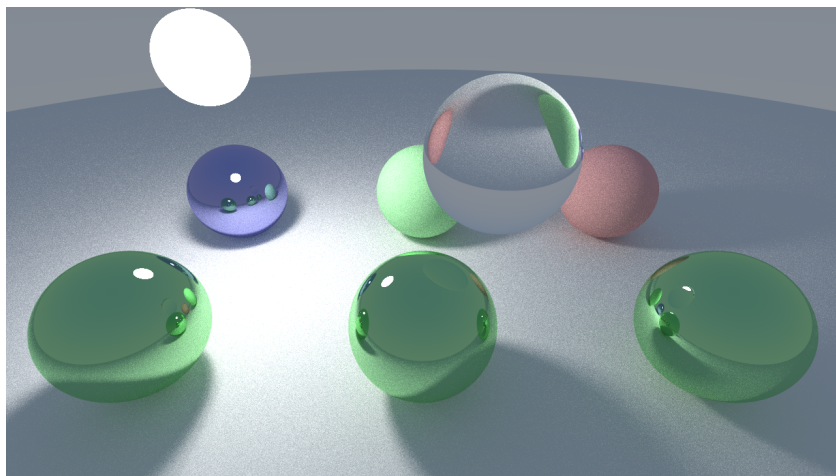


**Figure 1.4:** Computer generated imagery using ray tracing. The Monte Carlo method is used to “compute radiance along ray paths between lights and the camera”, to generate CGI images [29].

the tissue, and a numerical tissue damage model to assess the damage to the tissue due to the laser. The predictive power of the method is demonstrated by the way of optimising spy disposal. Discussion of the model, alongside validation of the model against theoretical and experimental evidence is presented.

Chapter 4 presents an adaptation to the regular Monte Carlo model so that it can model wave like properties of photons including diffraction and interference. The new algorithm is validated against several common experiments that exhibit the wave like behaviour of light, including: diffraction by slits and apertures. The algorithm is then used to model Bessel beams and shows their “self-healing” effect. Gaussian beam are also modelled using this new algorithm. The algorithm is also validated against real experimental data, taken by collaborators at the University of Dundee. Finally the algorithm is used to compare Bessel beams and Gaussian beam in highly turbid media, to determine which beam can image deepest.

Chapter 5 details the modelling of a novel biomarker for cardiovascular disease, autofluorescence. The theoretical groundwork for the biomarker is presented, along with discussion of how MCRT can model fluorescence. Presented alongside this is ameombaMCRT, a Monte Carlo radiation transfer simplex algorithm used to determine concentrations of fluorophores in different layers of tissue for a given spectrum.

Finally, a study of how tissue optics affect the autofluorescent signal is presented which investigates the effect of blood, melanin, and skin thickness can have on the autofluorescent signal. This includes the effect of blood, melanin, and the skin thickness at different sites on the body can affect the signal.

Finally, chapter 6 concludes this thesis and presents possible future avenues of research that could be undertaken.



# Chapter 2

# Monte Carlo Radiation Transport Technique

## 2.1 Introduction

This chapter will provide an overview of the Monte Carlo radiation transport method (MCRT) method and compares it to other light transport methods. Details of the MCRT code developed during this project and used as the basis of the results reported in subsequent chapters, validation of code, and details of computational speed up are also presented.

## 2.2 Monte Carlo Radiation Transport Algorithm

### 2.2.1 Introduction and Background

The technique that makes up the bulk of this thesis is the MCRT technique. This method was developed at the end of the Second World War at the Los Alamos National Laboratory, for the purpose of calculating neutron diffusion through shielding material [1–4]. It has since found a myriad of applications from light transport through dusty galactic clouds [30], calculating doses for radiotherapy [31] to light transport through tissue [32].

The theory that governs the transport of radiation through a medium is the radiative transfer equation (RTE). Before describing MCRT which is a numerical simulation of the RTE, the theory of radiation transport must be examined.

#### Radiative Transfer

Transport of radiant energy through turbid media can be modelled analytically using the RTE. The RTE models the radiative losses and gains by a beam of radiation as it propagates, including: loss of energy due to absorption, loss/gain of energy due to scattering, and energy gain due to emission. Before deriving the RTE, definitions of some terms and physical quantities is required.

The first term is spectral irradiance,  $L_\nu$ . Spectral irradiance is defined as the energy flow in a direction  $\hat{\mathbf{n}}$ , for a solid angle  $d\Omega$ , per unit time per unit temporal frequency bandwidth. Irradiance is defined as the spectral irradiance over a small frequency range  $[\nu, \nu + \Delta\nu]$ :

$$L(\vec{r}, \hat{s}, t) = L_\nu(\vec{r}, \hat{s}, t)\Delta\nu \quad (2.1)$$

Where:

- $\vec{r}$  is the position;
- $\hat{n}$  is the unit normal vector;
- $t$  is the time;
- and  $L(\vec{r}, \hat{s}, t)$  is the irradiance [ $W m^{-2} sr^{-1}$ ].

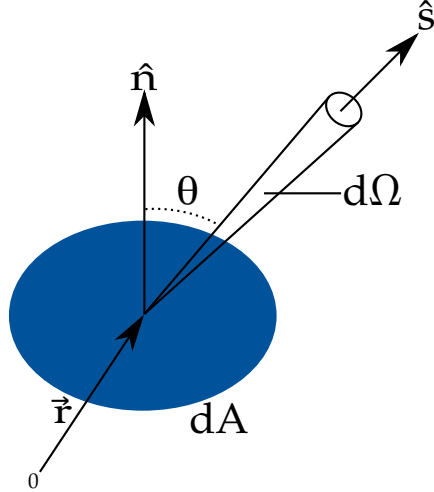


**Figure 2.1:** Energy flow through area  $dA$  within solid angle  $d\Omega$  in a direction  $\hat{s}$ . Adapted from [33, 34].

The irradiance can be used to determine the energy,  $dE$ , transported across an area  $dA$ , in a solid angle  $d\Omega$  in a time  $dt$  (see Fig. 2.1) is:

$$dE = L(\vec{r}, \hat{s}, t) \cdot \cos(\theta) \ dA \ d\Omega \ dt \quad (2.2)$$

Where:

- $\hat{n}$  is the unit normal to  $dA$ ;
- and  $\cos(\theta)$  is the angle between  $\hat{n}$  and  $\hat{s}$ .

Irradiance can also be used to determine the fluence rate,  $\phi$ , which is defined as the energy flow per unit time, independent of the flow direction.

$$\phi(\vec{r}, t) = \int_{4\pi} L(\vec{r}, \hat{s}, t) \ d\Omega \quad (2.3)$$

Where:

- $\phi$  is the fluence rate [ $W m^{-2}$ ].

Solving the RTE yields the irradiance which gives the distribution of light in the medium, information on the state of the system, and all the physical properties of it.

With the irradiance defined, as well as the other quantities that follow, the RTE can be derived [33, 34]. First considering the conservation of energy, as shown in Eq. (2.4).

$$dP = -dP_{div} - dP_{ext} + dP_{scatt} + dP_{src} \quad (2.4)$$

Where:

- $dP$  is the total change in energy in the volume  $dA ds$  within the solid angle,  $d\Omega$ , per unit

time (see Fig. 2.2);

$dP_{div}$  is the energy loss due to the divergence of the radiation beam per unit time;

$dP_{ext}$  is the energy loss due to absorption and scattering within the volume  $dA ds$  within the solid angle,  $d\Omega$ ;

$dP_{scatt}$  is the energy gain due to scattering from  $\hat{s}'$  into  $d\Omega$  per unit time;

and  $dP_{src}$  is the energy gain due to emission within the medium, per unit time.

The total change in energy,  $dP$ , in the volume element within the solid angle  $d\Omega$  is equal to:

$$dP = \frac{1}{c} \frac{\partial L(\vec{r}, \hat{s}, t)}{\partial t} dA ds d\Omega \quad (2.5)$$

Where  $c$  is the speed of light.

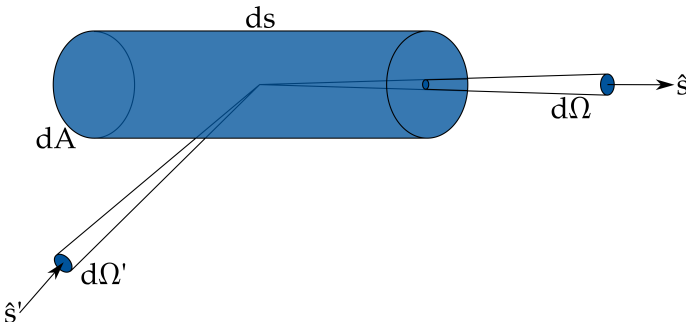


**Figure 2.2:** Cylindrical volume element,  $ds dA$ , with solid angle  $d\Omega$  in direction  $\hat{s}$  and solid angle  $d\Omega'$  in direction  $\hat{s}'$ . Energy flowing through this element is used to derive the radiation transfer equation. Adapted from [33, 34].

The first loss term,  $dP_{div}$ , is the energy loss due to divergence of the radiation beam. This is modelled as:

$$dP_{div} = \frac{\partial L}{\partial s} d\Omega dV \quad (2.6)$$

$$= \hat{s} \cdot \nabla L(\vec{r}, \hat{s}, t) d\Omega dV \quad (2.7)$$

$dP_{ext}$  is the second loss term, and accounts for energy loss due to scattering and absorption in the volume element within the solid angle  $d\Omega$ . This is modelled as:

$$dP_{ext} = \mu_t ds L(\vec{r}, \hat{s}, t) dA d\Omega \quad (2.8)$$

Where  $\mu_t$  is the extinction coefficient [ $m^{-1}$ ], see Section 2.2.2 for further details.

The first energy gain term,  $dP_{src}$ , is due to emission in the volume element within the solid angle  $d\Omega$  from a source,  $S(\vec{r}, \hat{s}, t)$  [ $Wm^{-3}sr^{-1}$ ].

$$dP_{src} = S(\vec{r}, \hat{s}, t) dV d\Omega \quad (2.9)$$

The second energy gain term, and final term, is due to the incident energy on the volume element within the solid angle  $d\Omega$  in direction  $\hat{s}$  due to scattering from any direction  $\hat{s}'$ .

$$dP_{scatt} = N_s dV \left( \int_{4\pi} L(\vec{r}, \hat{s}', t) P(\hat{s}', \hat{s}) \sigma_s d\Omega' \right) d\Omega \quad (2.10)$$

$$= \mu_s dV \left( \int_{4\pi} L(\vec{r}, \hat{s}', t) P(\hat{s}', \hat{s}) d\Omega' \right) d\Omega \quad (2.11)$$

Where:

$N_s$  is the number density of scatterers [ $\#m^{-3}$ ];

$P(\hat{s}', \hat{s})$  is the scattering phase function (see Section 2.2.2 for further discussion); and  $\sigma_s$  is the cross section of the scatterers [ $m^2$ ], thus  $\mu_s = N_s \sigma_s$ , where  $\mu_s$  is the scattering coefficient [ $m^{-1}$ ].

Finally substituting Eqs. (2.5), (2.7) to (2.9) and (2.11) into Eq. (2.4) yields the RTE:

$$\frac{1}{c} \frac{\partial L(\vec{r}, \hat{s}, t)}{\partial t} + s \cdot \nabla L(\vec{r}, \hat{s}, t) = -\mu_t L(\vec{r}, \hat{s}, t) + \mu_s \int_{4\pi} p(\hat{s}, \hat{s}') L(\vec{r}, \hat{s}', t) d\Omega' + S(\vec{r}, \hat{s}, t) \quad (2.12)$$

In general, the RTE is hard to solve in arbitrary 3D geometries, however there are several approximations, and numerical methods available. The diffusion approximation, Kubelka-Munk theory (K-M theory), and MCRT are the common methods used to approximate or solve the RTE.

### Kubelka-Munk Theory

K-M theory was originally developed to calculate the light distribution in thin layered materials, such as paint or paper [35]. The theory is rather simple and makes many assumptions about the medium and the incident light. The main assumptions of K-M theory are: only scattering and absorption take place in the medium, the incident light is already diffuse, the medium is uniform with only isotropic scattering, no external or internal reflections, and the medium is planar and infinitely wide [36–38].

These assumptions make K-M theory poor for modelling light-tissue interactions. This is because in tissue, scattering is not isotropic but rather forward biased (see Section 2.2.2). Tissue is rarely, planar and infinitely wide. Tissue also has some reflections at its external and internal boundaries, due to changes in refractive indices. Many medical and biophotonic treatments/methods use laser light which is not diffuse. Finally, tissue can also exhibit fluorescence, which the K-M theory is not able to model, along with polarization. K-M theory does have some positive aspects. K-M theory is good at calculating the diffuse reflectance of simple media, and can be used to roughly estimate calculations. Though it is not well suited for modelling light-tissue applications [39].

### Diffusion Approximation

The diffusion approximation for the RTE is where the irradiance is separated into two components:

$$L(\vec{r}, \hat{s}) = L_c(\vec{r}, \hat{s}) + L_d(\vec{r}, \hat{s}) \quad (2.13)$$

Where  $L_c$  is the unscattered contribution, which satisfies Beer's law\*, and  $L_d$  is the diffuse contribution. The  $L_d$  component is expanded using Legendre polynomials and truncated. The

---

\*Beer's law (or Beer-Lambert law) states that the transmission,  $T$ , is equal to  $e^{-\mu L}$ , where  $L$  is the distance and  $\mu$  is the attenuation coefficient.

diffusion approximation also has several assumptions and restrictions. The main assumption is that scattering dominates over absorption, and that the scattering is nearly isotropic. This restricts the types of scattering the diffusion approximation can model, though using similarity relations can partially model scattering in tissue [40, 41].

The diffusion approximation is computationally fast, and simple to implement. However, it is poor at modelling light-tissue interactions due to its assumptions and restrictions, mainly the inaccurate modelling near the boundaries of the medium and its lack of modelling fluorescence and other microphysics. Though it can be used to speed up MCRT in mediums where scattering dominates [42, 43].

## MCRT

The final method, MCRT, is numerically equivalent to the RTE [33]. MCRT is a flexible method, it can model arbitrary 3D geometries, various microphysics including fluorescence and polarisation. MCRT can also model various different light sources, from collimated laser beams to diffuse light sources. The only downside noted in the literature is that the MCRT can be expensive computationally. However, with computational power growing faster with time, this is less of a problem going forward.

The next several sections give an in depth description of the MCRT method and its flexibility, along with a description of the code used in this thesis to solve various medical and biophotonic problems.

### 2.2.2 Optical Properties

Before an in-depth description of the MCRT method is outlined, a discussion of the optical properties of materials is presented, which the MCRT method requires to simulate the transport of photons in a medium.

Optical properties of a medium are the properties that describe how light is transported through that medium. Usually the optical properties of a medium are defined by three main parameters: the scattering ( $\mu_s$ ), anisotropy ( $g$ ), and absorption ( $\mu_a$ ) coefficients.

#### Scattering

The scattering coefficient, along with the anisotropy value (see [Anisotropy](#)), define how light is scattered in a medium. The main scatterers in the deeper layers of the skin are filamentous proteins such as collagen and elastin [44]. In the upper layers of the skin, the main scatterers are keratins and various chromophores such as melanin. The size of the scatterers affect how light is scattered and into which direction that light is scattered into.

The scattering of light within tissue is usually defined as  $\mu_s$  or  $\mu'_s$ : the scattering coefficient and the reduced scattering coefficient, where  $\mu'_s = \mu_s(1 - g)$ . The scattering coefficient is defined such that the probability of transmission without scattering and neglecting absorption in a path length L is:

$$T = e^{-\mu_s L} \quad (2.14)$$

This gives units of inverse length for the scattering coefficient (usually measured in  $cm^{-1}$  in medical applications). The reduced scattering coefficient is often given in place of the scattering coefficient, as the reduced coefficient is more easily measured than the “normal” coefficient [45].

## Anisotropy

Anisotropy is the degree of deviation that light undergoes at each scattering event. The anisotropy value is taken from the phase function for the medium. The phase function is defined as the angular distribution of light intensity scattered by a particle. The phase function,  $\Phi(\theta, \phi)$ , is usually normalised over all angles:

$$\int_{\Omega} \Phi(\theta, \phi) d\Omega = 1 \quad (2.15)$$

Where  $\theta$ , and  $\phi$  are the usual polar and azimuthal spherical angles, and  $d\Omega = \sin \theta d\theta d\phi$ . Thus, for Rayleigh and isotropic scattering, their phase functions are:

$$\Phi_{isotropic}(\theta, \phi) = \frac{1}{4\pi} \quad (2.16)$$

$$\Phi_{Rayleigh}(\theta, \phi) = \frac{3}{8\pi}(1 + \cos^2(\theta)) \quad (2.17)$$

For simplicity, the phase function is usually cast as the anisotropy value  $g$ , which is defined as the average angle of deflection:

$$g = \langle \cos(\theta) \rangle = \int_{\Omega} \cos \theta \Phi(\theta, \phi) d\Omega \quad (2.18)$$

The anisotropy factor,  $g$ , can take on any value from  $-1$  to  $1$ . Where a value of  $-1$  is totally back scattering,  $0$  is isotropic scattering, and  $1$  is totally forward scattering (see Fig. 2.3).

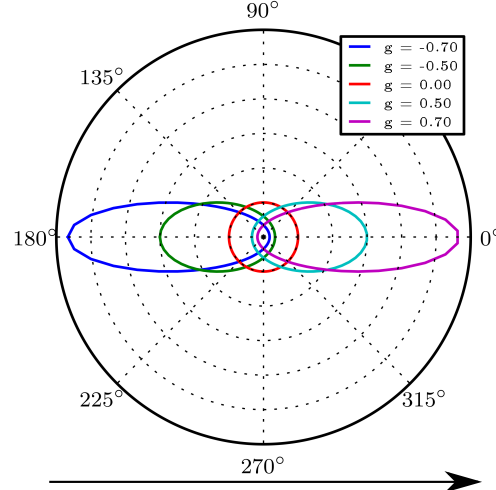


**Figure 2.3:** Figure shows the  $g$  factor for the Henyey-Greenstein phase function, for various configurations of back, forward or isotropic scattering. Arrow indicates the photons initial direction before scattering.

There are many phase functions that can be used to model the anisotropy factor in a medium. The standard phase function in biological tissue is the Henyey-Greenstein phase function. The Henyey-Greenstein phase function, was originally created to model scattering of diffuse radiation in the galaxy [46, 47]. It has since become the *de-facto* phase function for biological tissue. This

is due to the phase functions relative simplicity and due to it being regarded as a “good” phase function for approximating scattering in biological tissue [48]. The Henyey-Greenstein phase function is shown in Eq. (2.19):

$$\Phi_{H.G}(\theta, \phi) = \frac{1}{4\pi} \frac{1 - g^2}{(1 + g^2 - 2g \cos(\theta))^{\frac{3}{2}}} \quad (2.19)$$

The Henyey-Greenstein phase function will be adopted as the phase function for the whole of this thesis.

## Absorption

Absorption of light by a medium is defined by the absorption coefficient  $\mu_a$ . The absorption coefficient is defined in a similar fashion to the scattering coefficient, by considering the probability of transmission without absorbing and neglecting scattering in a path length L:

$$T = e^{-\mu_a L} \quad (2.20)$$

This, again like the scattering coefficient, gives inverse distance for the unit of the absorption coefficient (and usually measured in units of  $cm^{-1}$ ).

There are various sources of absorbers in tissue including blood, water, fat, melanin,  $\beta$ -carotene, and bilirubin. These chromophores can all contribute, depending on the wavelength, with some more absorbing than others, as shown in Fig. 2.4. The absorbed photons can then be remitted as fluorescence or absorbed as heat.

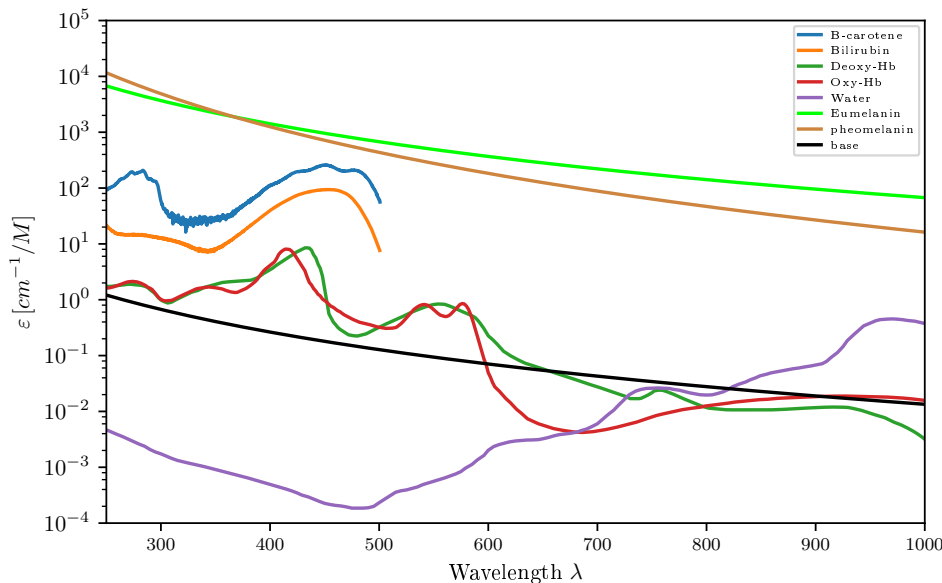


**Figure 2.4:** Examples of wavelength dependent absorption coefficients for some common tissue chromophores [45, 49–57].

## Derived Parameters

There are also some derived parameters that are useful to be defined. These are the albedo and the total attenuation coefficient.

The total attenuation coefficient is defined as the sum of the scattering coefficient and the absorption coefficient:

$$\mu_t = \mu_s + \mu_a \quad (2.21)$$

The albedo, or scattering probability, is defined as the ratio of the scattering coefficient to the total attenuation coefficient:

$$a = \frac{\mu_s}{\mu_a + \mu_s} = \frac{\mu_s}{\mu_t} \quad (2.22)$$

## Other Parameters

The preceding subsection described the optical properties that this thesis will use in every chapter. However, there are other optical properties that can be used to define a medium. These other parameters generally are used to model microphysics such as Raman scattering, polarization, fluorescence or reflection/refraction. This section will give a brief overview of these other optical properties.

### Fluorescence

Fluorescence occurs when a photon is absorbed by a fluorescent molecule and re-emitted with a new wavelength. Fluorescence is a reactively common phenomena, and is heavily utilised in biophotonics and medicine, to image, or monitor molecules in tissue. Again the optical property that models fluorescence is a coefficient that gives the probability of absorption and re-emission of a photon by a certain molecule. Usually this is in the form of an absorption coefficient or extinction coefficient. The extinction coefficient is a measurement of absorption in terms of the concentration of the absorber. Thus, if a medium has many fluorophores, then the total absorption coefficient is the bulk absorption of the medium plus the contribution from the fluorophores as in Eq. (2.23):

$$\mu_a = \ln(10) \sum_i C_i \varepsilon_i \quad (2.23)$$

Where  $C_i$  is the concentration of the  $i^{th}$  fluorophore, and  $\varepsilon_i$  is the extinction coefficient of the  $i^{th}$  fluorophore.

Fluorescence will be described in more depth in ??.

### 2.2.3 MCRT Algorithm

This section will provide an in depth description of the MCRT algorithm for the propagating photons through a spherical medium with optical properties  $\mu_s$ , and  $\mu_a$ . The subsequent section provides details of how the MCRT algorithm is implemented in the Fortran programming language, along with the various code details, such as the parallelisation of the code.

Figure 2.5 shows a flow chart of the MCRT algorithm described in this chapter.

#### Medium and Grid Set-up

The first step of any MCRT algorithm, is to set-up the medium the photons will propagate through. There are a variety of ways the medium can be set-up. For this section, it is assumed that the medium is an isotropic sphere, radius  $R$ , and centred at the origin. For simplicity one wavelength is considered,  $\lambda$ . As the MCRT algorithm presented here is run on a 3D Cartesian grid, the grid is setup before creating the spherical medium. The grid is composed of  $n_x \times n_y \times n_z$  voxels<sup>†</sup>, where each voxel can have its own optical properties. The grid is setup by first setting an array that stores the locations of the voxel boundary walls in the  $x$ ,  $y$ , and  $z$  directions. The next step is to setup the actual medium. This is achieved by discretising the medium onto a grid. For this example a sphere is inscribed into a cubic volume, by setting the optical properties of a voxel to that of the medium if the sphere encloses that voxel. The voxels out with sphere are set to that of the ambient medium. An example of a voxelised medium can be seen in Fig. 2.6.

#### Photon Launch and Initialisation

The second step in the MCRT algorithm, is to initialise the photon. Initialisation of the photon involves setting its initial position and direction. Again, how this is done depends on the experiment being simulated. Here the photon is initialised to the centre of the sphere. The initial direction is sampled isotropically, and set accordingly:

---

<sup>†</sup>A voxel is a 3D pixel

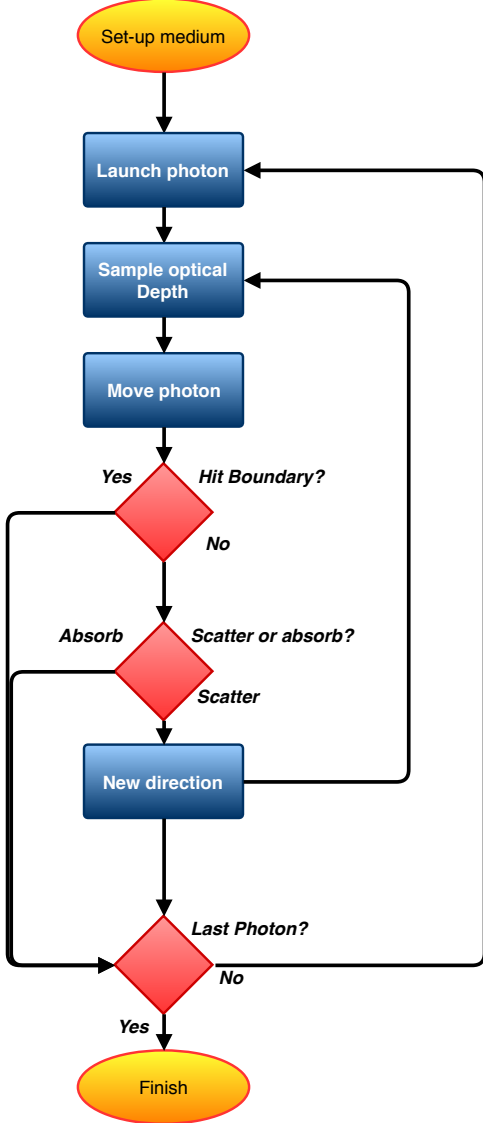


**Figure 2.5:** Flowchart of the Monte Carlo radiation transport algorithm as described in this section.

$$n_{xp} = \sin \theta \cdot \cos \phi \quad (2.24)$$

$$n_{yp} = \sin \theta \cdot \sin \phi \quad (2.25)$$

$$n_{zp} = \cos \theta \quad (2.26)$$

With  $\theta$  and  $\phi$  sampled uniformly between  $[0, \cos^{-1}(2\xi - 1)]$  and  $[0, 2\pi\xi]$  respectively, where  $\xi$  is a random number in the range  $[0,1)$ .

The next step is to launch a photon packet. Depending on the source of photon packets for a given simulation, this step varies from simulation to simulation. The general idea of launching a photon packet is that the packet is given an initial direction vector and position (which consists of a physical position and a voxel position)<sup>‡</sup>:

$$\text{direction} = \begin{bmatrix} n_{xp} \\ n_{yp} \\ n_{zp} \end{bmatrix} \quad (2.27)$$

$$\text{position} = [x_p, y_p, z_p] \quad (2.28)$$

$$\text{voxel} = [x_{cell}, y_{cell}, z_{cell}] \quad (2.29)$$

To set the direction vectors, the components of the direction vectors must be first set. The packets position is tracked using a Cartesian coordinate system, however for ease of computation for calculating scattering angles (see [Photon Interaction Event](#)), the direction vectors are computed in a spherical system thus the direction vectors are in Eqs. (2.24) to (2.26).

$\theta$  and  $\phi$  are generated dependent on the photon source used. The individual sine and cosine terms are saved for use in the scattering routines (see [Photon Interaction Event](#)). The position is then set according to the light source used. For this example the photons are released from the origin of the sphere. Using this position the voxel the packet is in is calculated.

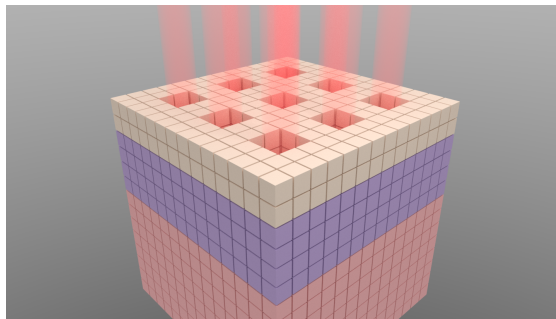


**Figure 2.6:** Example of a possible voxel model, with three different layers, various holes due to ablative pixel beam lasers ( see Chapter 3). Each voxel can represent a different optical/thermal property of the tissue medium.

### Photon Propagation

The next step in the algorithm is moving a packet to the next interaction point. The probability that a packet will interact over a distance  $dL$  is  $\mu_t dL$ , where  $\mu_t$  is the total extinction coefficient (see [Optical Properties](#)). Thus, the probability of travelling  $dL$  without any interaction is  $1 -$

---

<sup>‡</sup>all variables given in this section are the same as they are in the code.

$\mu_t dL$ . Therefore, over a distance  $L$  with  $N$  segments of length  $L/N$  the probability of travelling  $L$  before any interaction:

$$P(L) = (1 - \mu_t \frac{L}{N}) \cdot (1 - \mu_t \frac{L}{N}) \dots (1 - \mu_t \frac{L}{N}) = (1 - \mu_t \frac{L}{N})^N \quad (2.30)$$

$$P(L) = \lim_{N \rightarrow \infty} (1 - \mu_t \frac{L}{N})^N = e^{-\mu_t L} = e^{-\tau} \quad (2.31)$$

Where  $\tau$  is the number of mean free paths in a distance  $L$ . Eq. (2.31) is now a PDF for the distance a packet will travel before an interaction occurs. To be able to get a random optical depth, the PDF has to be able to be sampled from either analytically or via the rejection method. Using the Monte Carlo method described in Section 1.1, with  $\xi$  as our random number, gives:

$$\xi = \int_0^\tau e^{-\tau'} = 1 - e^{-\tau} \rightarrow \tau = -\ln(1 - \xi) \quad (2.32)$$

As  $\xi$  is symmetric about 0.5,  $1 - \xi$  can be substituted for  $\xi$  yielding:

$$\tau = -\ln(\xi) \quad (2.33)$$

$\tau$  is now the optical distance, however this needs to be converted into a physical distance so that the photon packet can be moved. From our definition of  $\tau$  we know that  $\tau = \int_0^L \mu_t dS$ , and if the medium is smooth and homogeneous (i.e not a gridded medium):

$$L = \frac{\tau}{\mu_t} \quad (2.34)$$

Therefore, to update the packets position it is simply:

$$x_p = x_p + L \cdot n_{xp} \quad (2.35)$$

$$y_p = y_p + L \cdot n_{yp} \quad (2.36)$$

$$z_p = z_p + L \cdot n_{zp} \quad (2.37)$$

However, as the code in this thesis is a 3D gridded Cartesian code, the method of updating and moving the packets position is slightly adjusted. As stated in [Medium and Grid Set-up](#), the medium has been discretised onto a grid, so that each voxel can have a different  $\mu_t$ , thus Eq. (2.34) becomes:

$$L = \frac{\tau}{\mu_{t,\zeta}} \quad \zeta = (x, y, z) \quad (2.38)$$

with  $\mu_{t,\zeta}$  the attenuation coefficient for the  $\zeta^{th}$  voxel.

Moving the photon through a voxelised medium is more involved than propagating a photon through a non voxelised medium. This is because the voxel the photon is in needs to be updated as the photon moves from voxel to voxel. The first step of moving the photon through a voxelised medium is drawing a random optical depth. This optical depth will be the full optical depth the photon travels before an interaction event. The generation of a random optical depth is as outlined above,  $\tau = -\ln(\xi)$ . As the photon travels through the voxel grid, a running total of the current optical distance travelled is kept. This is then compared to the randomly generated optical depth. When the running total optical depth equals the randomly generated optical depth the photon propagation is stopped, and the photon undergoes an interaction.

We then calculate the distance to the nearest voxel boundary in the  $x$ ,  $y$ , and  $z$  directions. The distance is calculated for each direction. Equation (2.39) shows for the  $x$  direction:

$$d_x = \frac{x_{face} - x_{cur}}{n_{xp}} \quad (2.39)$$

Where  $d_x$  is the distance to the nearest wall in the  $x$  direction.  $x_{face}$  is the voxel wall position in the  $x$  direction, and  $n_{xp}$  is the  $x$  direction vector. With three distances calculated,  $[d_x, d_y, d_z]$ , the minimum of these is thus the distance to the nearest voxel wall.

The next step is to calculate the optical depth for this distance. The optical depth is found by rearranging Eq. (2.38) for  $\tau$ , with  $L$  now the distance to the nearest wall. With the optical distance to the nearest wall calculated, the next step is to determine if there is “enough” optical distance left to travel the full distance to the nearest wall. Therefore, the running total optical distance is compared to the randomly generated optical distance. If the running total + the new optical distance to the nearest wall, is less than the randomly generated optical depth, then the photon travels to the nearest wall. The photon is then placed in the next voxel by a distance  $\delta$ , where  $\delta$  is just larger than machine precision. If the running total + the new optical distance to the nearest wall is greater than the generated optical distance then an interaction event occurs in the current voxel. The distance to the interaction event is calculated and the photon moved to this location.

Figure 2.7 illustrates this whole process for a 2D example.

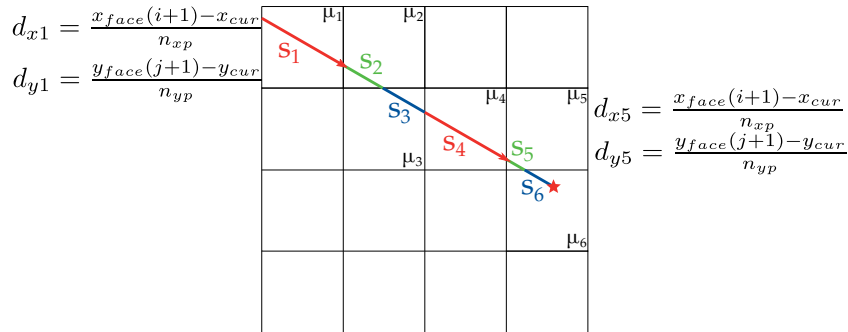


**Figure 2.7:** Illustration of photon propagation through a 2D grid.  $d_{x1}$ , and  $d_{y1}$  are the distances to the voxel walls in the  $x$  and  $y$  directions in the  $\mu_1$  voxel. In this case  $S_1 = d_{x1}$  as  $d_{x1}$  is smaller than  $d_{y1}$ , thus the photon hits the voxel wall in the  $x$  direction. For the  $\mu_5$  voxel,  $d_y$  is smaller, thus the photon hits the voxel wall in the  $y^{th}$  direction.

This whole process is repeated until the photon undergoes an interaction event or leaves the voxel medium. The next step in the algorithm is the interaction event, which can consist of either: scattering, absorbing or another microphysics phenomena.

### Photon Interaction Event

The next section of the algorithm is to decide how the photon interacts with the medium, either via scattering or absorption. There are other interaction events that can occur, however descriptions of these are left for the chapters that detail these behaviours.

To decide whether a packet scatters or absorbs a random number,  $\xi$ , is generated and compared against the albedo,  $a$ . If  $\xi < a$  then the packet scatters, otherwise it is absorbed.

## Packet Absorption

If the interaction event is a photon packet absorption, then the algorithm terminates the photon packets and starts the next photon packet, see [Termination](#).

## Packet Scattering

If the interaction event is a packet scattering, then the packet is scattered into a new direction and the above processes are carried out until a termination clause is met, see [Termination](#).

Depending on the medium being simulated, it can either be isotropic or anisotropic scattering. For the isotropic case, new  $\cos(\theta)$  and  $\phi$  angles are sampled uniformly, and the direction vectors set as in section [Photon Launch and Initialisation](#). For the case where the scattering is anisotropic the calculation of the scattering angles,  $\theta$  and  $\phi$ , is more complicated. The random sampling of the scattering angles,  $\theta$  and  $\phi$ , are valid in the “centre of mass” frame containing the scatter, incident and scattered ray. The photons position is updated in the lab frame, thus the direction vectors also have to be updated in the lab frame. This means that the scattering angles need to be rotated into the lab frame. For the isotropic case we assume that the scattering is also isotropic in the lab frame, thus the new direction vector is easily calculated. However, this is not the case for anisotropic scattering, as the centre of mass frame has to be rotated into the lab frame.

Figure 2.8 and Eq. (2.40) show how this process is achieved. Where  $\mathbf{n} = (n_x, n_y, n_z)$ ,  $\mathbf{n}_s = (n_x^{new}, n_y^{new}, n_z^{new})$ ,  $\theta_s$  is chosen from the phase function Eq. (2.41), and  $\varphi_s = 2\pi\xi$  with  $\xi$  being a random number in the range 0 to 1.

$$\begin{aligned} n_x^{new} &= \frac{\sin\theta_s}{\sin\theta} (n_x n_y \cos\varphi_s - n_y \sin\varphi_s) + n_x \cos\theta_s \\ n_y^{new} &= \frac{\sin\theta_s}{\sin\theta} (n_y n_z \cos\varphi_s + n_x \sin\varphi_s) + n_y \cos\theta_s \\ n_z^{new} &= -\sin\theta_s \cos\varphi_s + n_z \cos\theta_s \end{aligned} \quad (2.40)$$

$$\cos\theta_s = \frac{1 + g^2 - \left(\frac{1-g^2}{(1-g+2g\xi)^{3/2}}\right)^2}{2g} \quad (2.41)$$

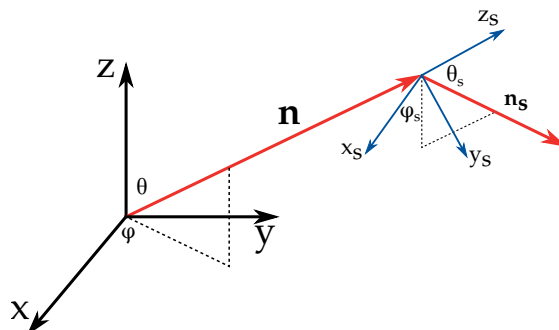


**Figure 2.8:** Illustration of rotating the centre of mass frame to the lab frame.  $\mathbf{n}$  is the direction vector of the photon before scattering, and  $\mathbf{n}_s$  is the scattered direction vector.  $\theta$  and  $\varphi$  are the scattering angles.  $z_s$  is in the same direction as  $\mathbf{n}$ .

## Termination

The final section of the MCRT algorithm is to check if it should be terminated. This is a simple check to see if there are any more photons to run. If there are more photons to run then the algorithm goes back to the [Photon Launch and Initialisation](#) section and continues from there. If there are no more photons the algorithm terminates and any results are written out.

## Scored Quantities

As MCRT is a computational method, a wealth of information is able to be recorded during the simulation. From the paths of individual photons, to average scattering angles and more. However, it is not practical to record all this information for every simulation, as this would lead to inefficient simulations, and expensive data storage solutions. Thus, for a given problem only the pertinent information is stored.

One important recorded variable is fluence. Fluence is the number of photons entering a sphere per unit cross section area [17]. In practice the average fluence per area is used, Eq. (2.42), as this is easier to calculate in an MCRT code. Lucy showed that the average fluence per area is proportional to the sum of the path length through a volume [58]:

$$J_i = \frac{L}{NV_\varsigma} \sum l \quad (2.42)$$

Where:

$J_i$  is the mean intensity such that the fluence is  $\Phi = 4\pi J [W m^{-2}]$ ;

$L$  is the luminosity or power of the light source [ $W$ ];

$N$  is the total number of photon packets [-];

$V_\varsigma$  is the volume of the  $\varsigma^{th}$  voxel [ $m^3$ ];

and  $l$  is the path length of a photon packet through the  $\varsigma^{th}$  voxel [ $m$ ].

Most chapters in this thesis make use of Eq. (2.42) or modified versions of it as the main scored quantity, e.g. to determine absorbed energy.

Other common scored quantities are the exit location of a photon, the wavelength of an exiting photon or the distribution of photon packet absorption.

### 2.2.4 Code Details

This section describes the implementation of the MCRT and of the parallelisation the code.

#### Code

All code in this thesis is written in modern Fortran<sup>§</sup>. All subroutines and functions are contained in modules (with the exception of the main program—main.f90). This is done to be able to “hide” data from subroutines and functions, and to arrange the code that relates to other parts of the code in the same file. Having the code in modules also allows the use of runtime allocation of memory for arrays. This enables the user to specify the size of arrays depending on the need of the user for the problem at hand.

Modules are classified into three different types: data, routines, and dependencies. Data modules are modules that contain no function or routines, but store variables that can be accessed anywhere in the program when required. Routine modules contain the subroutines and functions

---

<sup>§</sup>modern Fortran is considered anything past Fortran 95 [59].

used in the code. Finally dependency modules are the modules that have not been written by me, and thus the code depends upon them to run.

Figure 2.9 show the relationship between the various modules, for a basic version of the MCRT as described in [MCRT Algorithm](#).

Using Fig. 2.9 as a reference each module contains:

`mepolar.f90` is the entry point of the code. It calls all other subroutines and functions, as well as setting up various variables and printing progress.

`ch_opt` is the module where the optical properties are set or changed.

`gridset_mod` is where the optical properties grid and voxel walls are set.

`subs` contains general purpose routines that are used in various different parts of the code.

`writer_mod` contains routines that write out the results of the simulation.

`inttau2` is the module that contains the routines that propagate the photon through the voxel grid.

`sourceph_mod` contains the routines that initialise the photon position and direction.

`stokes_mod` contains the routine that calculates the scattering direction after a scattering event.

`iarray` is a data module that contains all the arrays in the code.

`constants` is a data module that contains all the constants and filepaths needed in the code.

`ieee_arithmetic` is an external dependency that gives various arithmetic checking routines such as `is_nan()`.

`vector_class` is a module that contains the vector type, and all its associated operations such as cross and dot products of vectors.

`photon_vars` is a data module that contains the data pertaining to each photon, such as wavelength or energy.

Finally, `opt_prop` contains the data about the current optical properties such as the albedo and absorption coefficient.

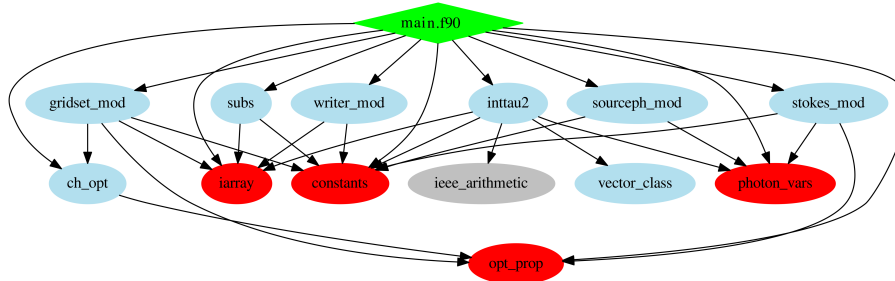


**Figure 2.9:** Source code hierarchy, showing the relationship between different modules. Green is the entry point for the simulation. Red are the data modules, light blue are the routine modules, and grey are the external dependencies.

## Parallelisation of the MCRT Algorithm

As mentioned in the previous sections, MCRT can be computationally intensive, especially when dealing with highly scattering mediums. Fluorescence can also cause simulations times to dras-

tically increase as photons are no longer “killed” off, but rather re-emitted at a new wavelength. Other optical processes such as Raman scattering are highly unlikely events, which again can lead to a dramatic increase in simulation times, as many photons are required to be simulated to get “good” statistics.

Fortunately MCRT is classed as an “embarrassingly parallel” problem<sup>¶</sup>. This means that it is trivial to parallelise in comparison to other algorithms. The reason that MCRT is classed as “embarrassingly parallel”, is that the algorithm can be split up onto separate processors, with little need for communication between them. In reality this means that  $n$  copies of the algorithm can run on  $n$  cores in a processor, with communication taking place at the start and end of each simulation run.

All the code in this thesis is parallelised using Message-passing interface (MPI) [61, 62], with the only communication taking place at the end, where the results are collated on to all processes. The one exception to this is in Chapter 3, where the heat diffusion calculation needs communication between the processes during the calculation.

The parallel efficiency of a code depends on the problem and the number of photon packets run. To determine the speedup of a given problem, Amdahl’s law is used [63]:

$$speedup = \frac{1}{(1 - P) + P/N} \quad (2.43)$$

Where  $P$  is the fraction of the code that is parallel, and  $N$  is the number of cores the code is run on. The consequence of Amdahl’s law is as  $N$  tends to infinity the speedup tends to a maximum:

$$speedup_{max} = \frac{1}{1 - P} \quad (2.44)$$

The value of  $P$  varies from problem to problem and the number of photon packets run. Figure 2.10 shows the results of the profiling of the code, for various numbers of cores. This test consisted of running the same number of photons, in a highly scattering medium of size  $2\text{ cm}^3$ . This yielded a  $P$  of  $0.999010 \pm 0.000045$  and a maximum speedup of 1010.1.

---

<sup>¶</sup>However, this is not true for all MCRT applications. For example, using the Bjorkman & Wood [60] immediate temperature corrections method, turns MCRT into a different class of parallel problem [26].

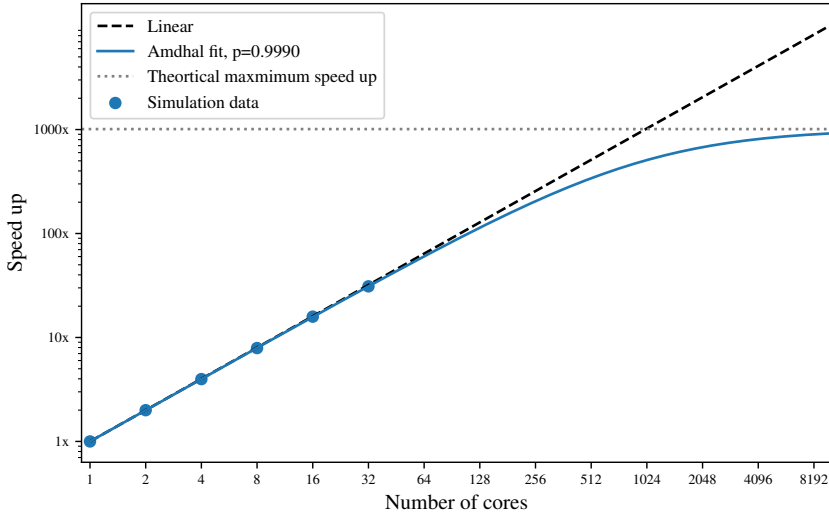


**Figure 2.10:** Performance of the parallelisation of the MCRT code using MPI.

## 2.3 Validation of MCRT Code

As the Monte Carlo method is an algorithm that depends upon random numbers, it is sometimes hard to ensure the correct result is obtained. Or to put it another way:

“Monte Carlo is easy to do wrong!” G.W. Collins III [64]

Thus, the code has to be validated against various theoretical/experimental and other simulations, to determine whether the results are correct.

The main benchmark of the MCRT code is a comparison against an expression for fluence as a function of depth [65]. This expression has also been fitted to by other MCRT simulations [66].

$$\Psi(z) = \Psi_0(C_1 e^{-k_1 z/\delta} - C_2 e^{-k_2 z/\delta}) \quad (2.45)$$

Where:

$\Psi(z)$  is the penetration of the incident light, or equivalently the fluence rate [ $W\text{ cm}^{-2}$ ];

$\Psi_0$  is a normalisation constant [ $W\text{ cm}^{-2}$ ];

$C_n$  and  $k_n$  are fitted coefficients [-];

and  $\delta$  is the optical penetration depth, defined as  $\delta = 1/\sqrt{3\mu_a(\mu_a + \mu_s(1-g))}$ , [cm].

Jacques *et al.*, in their simulation used two different wavelengths, 420 nm and 630 nm. The medium in the simulation is an infinitely wide slab with a depth of 1 cm, with uniform optical properties. The medium has a refractive index of 1.38. The  $g$  value is in the range 0.7 — 0.9, and the optical properties are as in Table 2.1.

Wavelength/nm	Absorption	Scattering	Penetration			$\delta/cm$	
	$\mu_a/cm^{-1}$	$\mu_s(1-g)/cm^{-1}$	C1	k1	C2		
420	1.8	82	5.76	1.00	1.31	10.2	0.047
630	0.23	21	6.27	1.00	1.18	14.4	0.261

**Table 2.1:** Table of optical properties and determined coefficients from Jacques *et al.* [66].

Using these values Jacques *et al.* calculated values for  $C_1$ ,  $C_2$ ,  $k_1$  and  $k_2$  using their MCRT code. The above optical properties and medium dimensions<sup>||</sup> are recreated in the code and a value of 0.9 was chosen for  $g$ . 8 million photons were run for the simulation. This yielded the result as in Fig. 2.11.

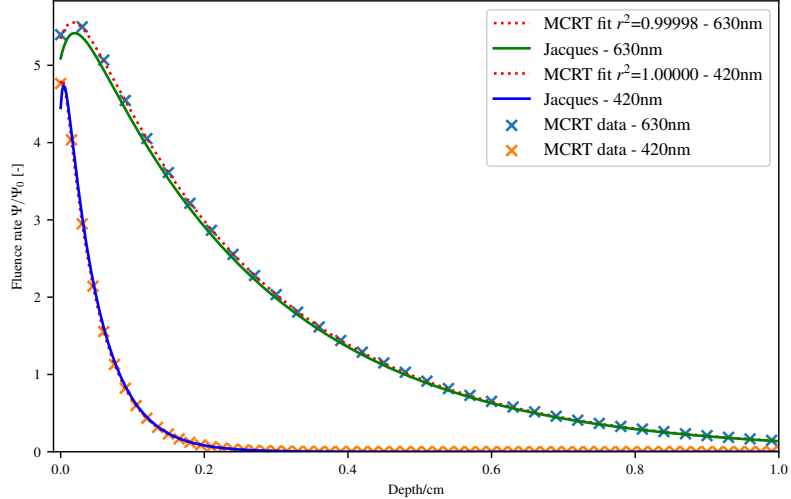


**Figure 2.11:** Figure shows the fluence as a function of depth. Figure also shows comparison to the Jacques MCRT simulation and the MCRT as described in this chapter.

Fitting Eq. (2.45) to the data calculated by our MCRT code for 630 nm, gave:  $C_1 = 6.425$ ,  $C_2 = 1.083$ ,  $k_1 = 1.0$ , and  $k_2 = 12.966$ . For 420 nm gave:  $C_1 = 5.600$ ,  $C_2 = 0.838$ ,  $k_1 = 1.003$ , and  $k_2 = 9.846$ . These are in good agreement (within code differences) with Jacques *et al.* results.

## 2.4 Conclusion

There are various methods available to model the radiative transport equation. MCRT is the most flexible of the methods available, allowing arbitrary geometries, light sources, multiple anisotropic scattering, and various microphysics to be modelled. This chapter presented an overview of the MCRT algorithm that will be the basis of the results presented in the following chapters. The code described in this chapter is based upon K. Wood's MCRT code for light propagation in galactic dust clouds. It has been rewritten in modern Fortran and adapted so that the code can model biological tissue so that the code can be applied to various medical and biophotonic problems. The optical properties required in a MCRT simulation have been discussed, and will be utilised to subsequent chapters. A description of how the code has been parallelised and validated against a standard literature code has also been presented.

---

<sup>||</sup>The infinitely wide slab is implemented so that when a photon leaves one of the sides of the voxel grid, it is moved to the other side of the grid, retaining its original direction vectors.

# Chapter 3

## Computational Modelling of Tissue Ablation

### 3.1 Introduction and Background

This chapter uses MCRT techniques coupled to a heat transfer simulation, to study the thermal damage to tissue due to a laser, with its power spread over many beams to leave viable tissue around zones of damaged/necrotic tissue [67]. This class of laser is called a fractionated ablative laser. This chapter presents experimental work carried out on porcine tissue by our collaborators at the University of Dundee and the photobiology department at Ninewells Hospital, alongside my computational model of tissue ablation.

Ablative lasers are used in a wide variety of medical procedures including: coagulating scalpels, port wine stain removal, tattoo removal, hair removal, and skin rejuvenation [68–72]. One class of laser used in these procedures are ablative lasers. Ablative lasers are usually high powered lasers ( $>30\text{ W}$ ) targeted at a specific chromophore in the skin, to partially or fully remove layers of skin. These types of lasers are commonly used for aesthetic procedures such as: skin rejuvenation [72], and removal of various diseases such as Rhinophyma [73] or lesions/nodules [74]. Ablative lasers have also been recently investigated as a means of better drug penetration into the skin for various therapies such as photo-dynamic therapy (PDT). The ablative laser “drills” holes in the skin, which allows topical treatments to better diffuse into the skin [75].

One downside to using lasers to remove tissue, is that unlike a scalpel where the surgeon has full control of the depth of the incision, ablative lasers are not as predictable. Lasers can cause thermal damage to the surrounding areas, leading to potentially unwanted effects, though some applications of ablative lasers utilise the thermal damage, particularly aesthetic procedures [76].

Currently, the standard method to measure the depth of the ablative holes is via a biopsy which is an invasive procedure. In this work an optical coherence tomography (OCT) system is used to measure the ablative crater non-invasively *in-vivo*. The OCT measurements are then compared to a computational model developed as part of this project. It is hoped this computational model could be used to predict the depth of the ablative crater when using a certain laser power for various different applications such as: laser assisted drug delivery, and various cosmetic applications.

## 3.2 Methods

To replicate the experimental work *in silico*, the numerical model has three main portions. The first is the MCRT code that models light transport through tissue so that we can calculate the laser energy deposited as a function of time and space. The second, a finite difference method (FDM) which is used to calculate the heat diffusion within the tissue due to the absorbed laser energy. Finally, a tissue damage model to track the tissue damage caused by the laser. All these individual functions are connected together to create a full numerical model.

### 3.2.1 Monte Carlo radiation transport (MCRT)

MCRT is used here to calculate the energy deposited by the laser. This is then passed to the heat transport simulation, which calculates the heat diffusion in the medium. The algorithm for the three coupled simulations is presented in Fig. 3.1.

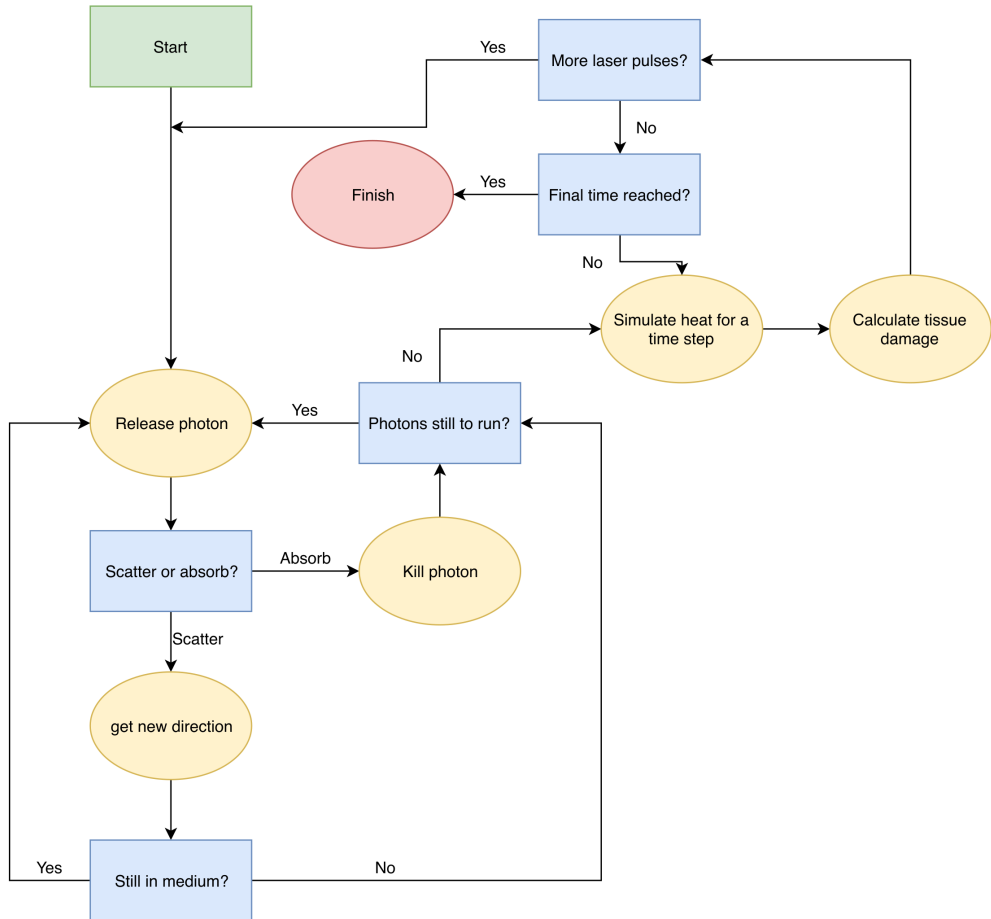


**Figure 3.1:** Flowchart of the tissue ablation algorithm.

The MCRT algorithm is largely the same as described in Chapter 2, with some important adjustments.

The first adjustment is that the path length counter for fluence is changed to track absorbed energy. This is achieved by multiplying the pathlength in a voxel by the absorption coefficient of that voxel. Figure 3.2 show this process graphically, and Equation (3.34) shows the mathematical expression:

$$E_i^{abs} = \frac{P}{NV_i} \sum \mu_{a,i} s \quad (3.1)$$

Where:

- $E_i^{abs}$  is the energy absorbed in the  $i^{th}$  voxel [ $J s^{-1} m^{-3}$ ];
- $P$  is power [W];
- $N$  is the number of packets, representing a power,  $P_i$ ;
- $V_i$  is the volume of the  $i^{th}$  voxel [ $m^{-3}$ ];
- $\mu_{a,i}$  is the absorption coefficient of the  $i^{th}$  voxel [ $cm^{-1}$ ];
- and  $s$  is the pathlength of a packet through the  $i^{th}$  voxel [cm].

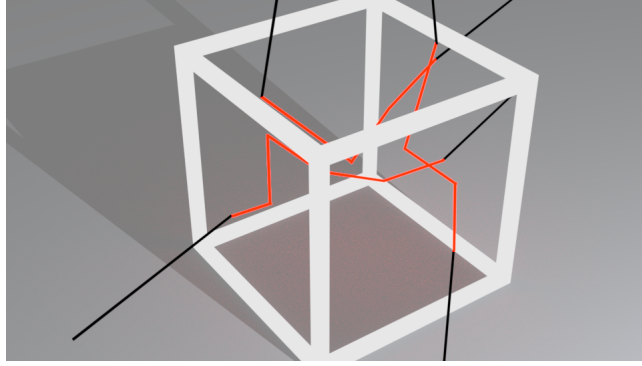


**Figure 3.2:** Red lines are packet paths within a voxel. Black lines packet paths out with the voxel. Red packet paths, weighted by  $\mu_a$ , are summed up to calculate the absorbed energy within each voxel.

This grid of absorbed energy is then passed to the heat transport portion of the simulation, so that the heat diffusion in the porcine tissue can be calculated.

The next adjustment to the MCRT algorithm is that the MCRT algorithm is run for every heat simulation time step, as the medium could change at every time step due to the optical, and thermal properties changing as a function of tissue damage.

Finally, to match the experiment undertaken the medium and laser for the *in-silico* experiments must match the practical experiments. As the laser used in the experiments emits an infra-red wavelength ( $10.6 \mu m$ ), the optical properties are dominated by the water content of the tissue. Due to this it is assumed that there is just absorption in the medium, with no scattering. Further discussion can be found in Section 3.3.1. The laser in some of the *in silico* modelling, has multiple beams and the source photon packet routine is adjusted to accommodate this when needed.

### 3.2.2 Heat Transport

The diffusion of heat can be modelled using the heat equation (Eq. (3.2)), which is derived from Fourier's law and the principle of conservation of energy [77]. The standard heat equation is a partial differential equation of the parabolic form. Solutions and analytical methods are readily

available for lower dimensions (i.e. 1D heat diffusion), but for higher dimensions, numerical models must be used for all except the simplest problems. The simplest form of the heat equation is shown below:

$$\rho c_p \frac{\partial T}{\partial t} = \nabla \cdot (\kappa \nabla T) + \dot{q} \quad (3.2)$$

Where:

- $T(x, y, z, t)$  is the temperature as a function of time and space [ $K$ ];
- $\kappa$  is the thermal conductivity [ $Wm^{-1}K^{-1}$ ];
- $\rho$  is the density [ $kgm^{-3}$ ];
- $c_p$  the specific heat capacity [ $JK^{-1}$ ];
- $\dot{q}(x, y, z, t)$  is the source/sink term as a function of time and space [ $Wm^{-3}$ ].

Equation (3.2) is for a homogeneous system where the thermal properties do not change as a function of time, space and temperature. However, to model a moving ablation front the nonlinear heat equation must be used, where the thermal properties can be a function of time, space and temperature (Eq. (3.3)).

$$\frac{\partial T}{\partial t} = \frac{1}{(\rho c_p)_\xi} (\nabla k_\xi T + k_\xi \nabla^2 T) + \dot{q}, \quad \text{where } \xi = (i, j, k) \quad (3.3)$$

Included in Eq. (3.3) is a source and sink term,  $\dot{q}$ , to allow the modelling of heat loss/gain from external sources/sinks. The heat source in this simulation is due to the laser, and it is assumed that the only loss of heat to the surrounding medium is via conduction.

The medium is considered to be at a constant temperature of 5°C, as the porcine skin was kept cooled prior to experimental work and the simulation volume is smaller than the porcine tissue samples.

As Eq. (3.3) is generally hard to solve in arbitrary geometries with complex boundary conditions, a numerical method is employed to solve it. The numerical method employed is a finite difference method (FDM), derived from the Taylor series, see Eq. (3.4).

A function  $f(x)$  is discretised onto a grid with  $N$  nodes a distance  $\Delta x$  apart. Equation (3.4) is then truncated and rearranged and it is assumed that the remainder term  $R_1$  is sufficiently small enough, to yield an approximation for the first derivative of a function  $f(x)$  at a point  $x_0 + \Delta x$ , see Eq. (3.5). Equation (3.5) is the so called “forward” difference, due to it using a point in the “forward” direction. The “backward” and “central” difference terms can be calculated by using a node at  $x_0 - \Delta x$  for the backward difference Eq. (3.6b). The central difference (Eq. (3.6c)) is an average of the forward and backward differences. Expressions can also be given for the 2<sup>nd</sup> derivatives for backward, forward and central (forward and backward 2<sup>nd</sup> order equations omitted for brevity) Eq. (3.6d).

$$f(x_0 + \Delta x) = f(x_0) + \frac{f'(x_0)}{1!} \Delta x + \frac{f''(x_0)}{2!} \Delta x^2 + \dots + \frac{f^{(n)}(x_0)}{n!} \Delta x^n + R_n(x) \quad (3.4)$$

$$f'(x_0) \approx \frac{f(x_0 + \Delta x) - f(x_0)}{\Delta x} \quad (3.5)$$

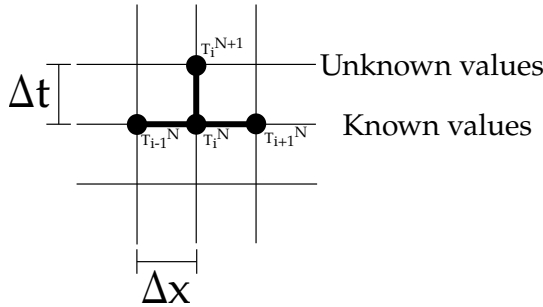


**Figure 3.3:** Finite difference method stencil for simple explicit scheme.

$$\frac{df}{dx} = \frac{f_{i+1} - f_i}{\Delta x} * \quad (forward) \quad (3.6a)$$

$$\frac{df}{dx} = \frac{f_i - f_{i-1}}{\Delta x} \quad (backward) \quad (3.6b)$$

$$\frac{df}{dx} = \frac{f_{i+1} - f_{i-1}}{2\Delta x} \quad (central) \quad (3.6c)$$

$$\frac{d^2f}{dx^2} = \frac{f_{i-1} - 2f_i + f_{i+1}}{\Delta x^2} \quad (central) \quad (3.6d)$$

Thus, the linear heat equation Eq. (3.2), in 1D, taking a 1<sup>st</sup> order forward time derivative, and a 2<sup>nd</sup> order central spatial derivative gives:

$$\frac{T_i^{n+1} - T_i^n}{\Delta t} = \alpha \frac{T_{i-1}^n - T_i^n + T_{i+1}^n}{\Delta x^2} + \frac{\dot{q}}{\rho c_p} \quad (3.7a)$$

$$T_i^{n+1} = \alpha \Delta t \frac{T_{i-1}^n - 2T_i^n + T_{i+1}^n}{\Delta x^2} + \frac{\Delta t \dot{q}}{\rho c_p} \quad (3.7b)$$

Where  $\alpha = \frac{\kappa}{\rho c}$ .

Equation (3.7b) is called the “simple explicit form of finite-difference approximation” [78]. Figure 3.3 shows the “stencil” of this scheme, where there are three known points at time  $N$ , and just one unknown at time  $N+1$ . There are various other schemes that can be used to calculate the temperature at the next time step. However, the simple explicit scheme is used here due to its ease of implementation despite there being a constraint on the time step used in comparison to an implicit method where there is none. This method is also easily scaled up to 3D with little difficulty.

For the more complicated nonlinear heat equation there is a possibility that the medium is not continuously smooth between nodes, in terms of optical and thermal properties. The two easiest methods [78] of achieving this are: (1), lag the value behind by one step, i.e  $c_p^{n+1} = c_p^n$ . (2), average  $\kappa$ ,  $\rho$ , and  $c_p$  using a half difference scheme where the thermal property used in the calculation is the thermal property halfway between two nodes, i.e the average of the two nodes:

---

\*For brevity  $f(x_0 + \Delta x)$  is defined as  $f_{i+1}$ , and  $f(x_0 - \Delta x)$  as  $f_{i-1}$ , etc.

$$\kappa^\pm = \frac{\kappa_i + \kappa_{i\pm 1}}{2} \quad (3.8)$$

$$\rho^\pm = \frac{\rho_i + \rho_{i\pm 1}}{2} \quad (3.9)$$

$$c_p^\pm = \frac{c_{p,i} + c_{p,i\pm 1}}{2} \quad (3.10)$$

Thus, for the simple 1D case as in Eq. (3.7b), the thermal properties are averaged between nodes when computing the coefficients of the temperature nodes, and lag the thermal properties when adding the heat from the laser:

$$T^{N+1} = \Delta t (AT_{i-1}^N - 2BT_i^N + DT_{i+1}^N) + T_i^N + \frac{\Delta t}{\rho c_p} q_L \quad (3.11)$$

Where (in the  $x$  direction):

$$\begin{aligned} A &= \frac{\kappa^-}{\rho^- c_p^- 2\Delta x^2} \\ B &= \frac{\kappa^+}{\rho^+ c_p^+ 2\Delta x^2} \\ D &= \frac{(A + B)}{2} \end{aligned} \quad (3.12)$$

Equation (3.11) is straightforward to generalise to higher dimensions. The 3D case gives:

$$U_{xx} = (AT_{i-1,j,k}^N - 2BT_{i,j,k}^N + DT_{i+1,j,k}^N) \quad (3.13)$$

$$U_{yy} = (AT_{i,j-1,k}^N - 2BT_{i,j,k}^N + DT_{i,j+1,k}^N) \quad (3.14)$$

$$U_{zz} = (AT_{i,j,k-1}^N - 2BT_{i,j,k}^N + DT_{i,j,k+1}^N) \quad (3.15)$$

$$T_{i,j,k}^{N+1} = \Delta t (U_{xx} + U_{yy} + U_{zz}) + T_{i,j,k}^N + \frac{\Delta t}{\rho c_p} q_L \quad (3.16)$$

Where:

$T_{i,j,k}^{N+1}$  is the new temperature at node  $i, j, k$  [K];

$T_{i,j,k}^N$  is the temperature at node  $i, j, k$  at the current time step [K];

$\alpha$  is the thermal diffusivity [ $m^2 s^{-1}$ ];

$\kappa$  is the thermal conductivity [ $W/mK$ ];

$\Delta x$  etc. is the size of the grid element in the  $p^{th}$  direction [m];

and  $A, B, D$  are the coefficients in their respective dimension (Eq. (3.12)).

Equation (3.16) gives the full numerical solution to the nonlinear heat equation with a laser heat source. This will allow the calculation of the heat diffusion in the porcine tissue due to laser heating.

As the laser used in the experimental work operates in a pulsed mode, this is accounted for in the simulation. The laser pulse shape is a triangular pulse, with the peak power,  $P_{peak}$ , and pulse length,  $\tau$  [79]. In the heat simulation there has to be an additional variable in the term  $laserOn(t) \cdot \frac{\alpha \Delta t}{\kappa} q_L$  in Eq. (3.16). This additional variable,  $laserOn(t)$ , is a boolean value and a function of time, which is defined as:

$$laserOn = \begin{cases} 1, & \text{Laser on} \\ 0, & \text{Laser off.} \end{cases}$$

In the instance where there is a train of laser pulses, the laser is turned on and off based upon the pulse frequency.

Due to a simple explicit FDM being used, the time step is constrained to make the solution stable. For a cubic 3D FDM without prescribed flux boundary conditions, this yields the constraint:  $\Delta t \leq \frac{1}{\delta\alpha}$  where  $\delta = \frac{1}{\Delta x^2} + \frac{1}{\Delta y^2} + \frac{1}{\Delta z^2}$ . Along with this time constraint, the pulse length of the laser also has to be considered. If the time step of the heat simulation is too large it will not account for the heat deposited by the laser. Thus, the timestep has to be at least an order of magnitude smaller than the shortest laser pulse.

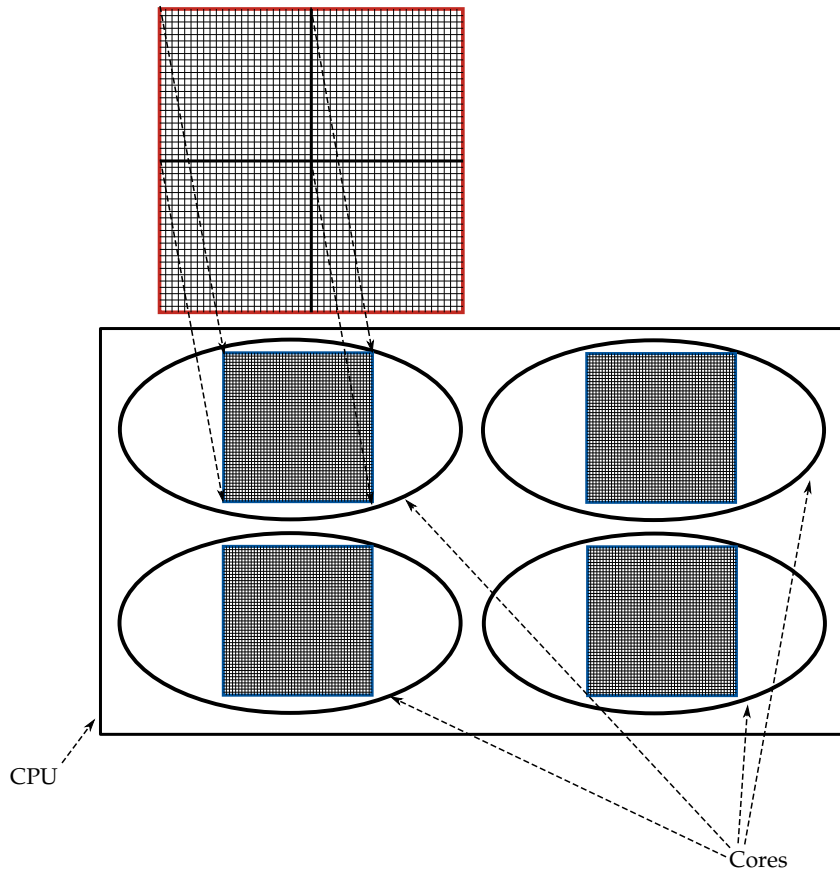
As the time step is small, and the grid resolution large the resultant simulation is slow. Thus, the code has been fully parallelised to improve performance. Both the MCRT and heat simulation are independently parallelised.

Parallelisation of the heat simulation is more involved than the “embarrassingly parallel” class of problems where MCRT belongs. This is due to the heat simulation being dependent on neighbouring nodes to update the temperature at the current node. Thus, if the medium were to be split up on to separate cores, there would have to be communication between the cores, in order for the simulation to be completed successfully. Therefore it is not possible to take the “easy” route of running the simulation concurrently  $N$  times and collating the result at the end of all the simulations.

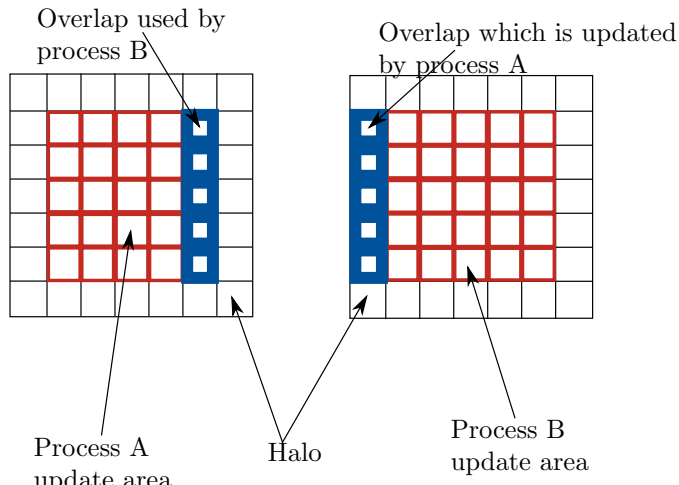
The heat simulation is parallelised using a technique called “halo swapping”. This involves splitting up the computational domain (see Fig. 3.4), in this case the tissue medium, and doing the calculations on each domain on a separate core. The “halo swapping” comes in when cores need to communicate with each other about updating their boundary temperature nodes (see Fig. 3.5).

Figure 3.6 shows the speed up gained from using the technique. The “halo swapping” technique is efficient for situations where the computational domain can be split up with large “chunks” being calculated on each core. However, if the computational domain is small, and the number of cores large then bottlenecks occur due to too much communication between cores taking place. Thus, to efficiently use “halo swapping” careful thought has to be given to the size of the computational domain, and the number of cores running the simulation. Evidence of this bottlenecking can be seen in Fig. 3.6 for problems where the size of the grid, in voxels, is  $40^3$  and  $24^3$ . These problems also show superlinear speed up, for a certain number of cores. This is not unfeasible, due to several reasons, in particular the underlying computer architecture [80].

After one time step of the heat simulation has been completed, the temperature grid is passed to the tissue damage portion of the simulation to calculate the tissue damage that may have accrued during the heat simulation time step.



**Figure 3.4:** Computational domain decomposition. Total computational domain (red outline) is evenly divided between cores in the CPU. This is done via layers of the domain in the z direction. Information is passed to/from cores via the “halo swap” process (see Fig. 3.5).



**Figure 3.5:** Halo swapping. Process A updates the area in red and blue on the left. It updates the blue area which is sent to process B as B’s “halo”. Process B cannot update its own halo, but rather updates the halo for process A.

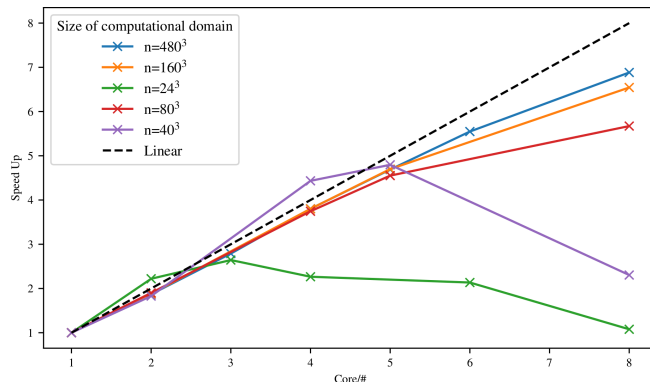


**Figure 3.6:** Figure shows the speed up gained by parallelisation of the heat simulation using the “halo swapping” technique, for various sizes of computational domain (voxels). Data taken from a Intel Xeon E3-1245 v5, 8 cores @ 3.5GHz machine.

### 3.2.3 Tissue Damage

#### Introduction

The final portion of the simulation is the tissue damage model. To be able to model the tissue damage process, the physical reality of this process must be understood. When the laser is turned on, the temperature starts to rise within the tissue due to the absorption of photons by the tissue. The temperature rise causes damage to the tissue when above a threshold temperature,  $T_d$ , approximately  $43^\circ\text{C}$  [81]. From the temperature,  $T_d$ , four main areas of tissue damage are defined:

$$T = \begin{cases} \text{coagulation,} & T_d \leq T \leq 100^\circ\text{C} \\ \text{water boils,} & T = 100^\circ\text{C} \\ \text{carbonisation,} & 100^\circ\text{C} \leq T \leq T_a \\ \text{ablation,} & T = T_a. \end{cases} \quad (3.17)$$

The area of tissue damage termed “coagulation” is a multifaceted process. At  $43^\circ\text{C}$  -  $50^\circ\text{C}$ , bonds break within cell membranes, causing ruptures and some cell death [81,82]. This process is usually termed *hyperthermia*. Around  $50^\circ\text{C}$ , enzyme activity decreases, cells become immobile, and various cell repair mechanisms are disabled, leading to increased cell death. When temperatures exceed  $60^\circ\text{C}$ , proteins become denatured. Thermal denaturation is a structural and functional change in a protein due to the heating it undergoes. This means they change from a highly organised structure with specific purposes, to disorganised structures with little to no function at all [83].

The next stage in the tissue damage process is the vaporisation of water. As the temperature of the tissue starts to approach  $100^\circ\text{C}$  (at 1 atm), water starts to vaporise. If the vaporised water cannot escape the tissue it forms steam vacuoles, small pockets of steam. These vacuoles can easily been seen when viewing tissue samples after tissue has been treated with a high powered laser (see Fig. 3.7). In certain conditions these steam pockets can explode [84].

The third stage of tissue damage is carbonisation of the tissue. This occurs when most of the water has boiled off, leaving the remaining tissue to heat up and reduce to its elemental carbon form. This carbonisation of tissue, when it occurs, is generally only a thin layer of 5-20  $\mu\text{m}$  [81,85].

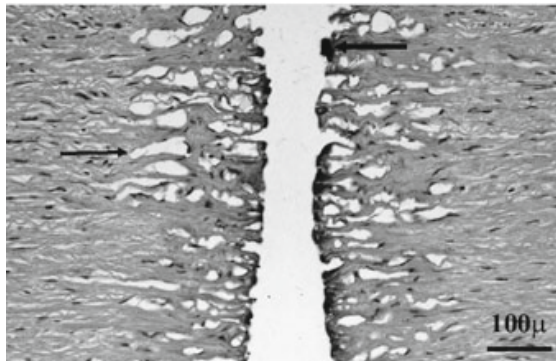


**Figure 3.7:** Ablation of a dog aorta, as viewed under a microscope. Steam vacuoles are clearly visible on either side of the ablation area. Carbonisation is also evident at the edges of the ablation fronts. Adapted from [81].

The final stage of tissue damage is the removal of the remaining tissue, i.e tissue ablation. There is no agreement in the literature how tissue undergoes ablation with several methods proposed. The three main methods are: photochemical, thermal, and explosive [86–88]. Photochemical ablation is when the energy of a photon from the irradiating laser, is sufficient enough that it excites the electronic state of the tissues molecules into an anti-boding state, leading to broken bonds and conversion from electronic energy into kinetic energy, and thus ablation. Thermal ablation is where tissue is heated sufficiently so that tissue vaporisation takes place. Finally, explosive ablation is an extreme version of thermal ablation. Explosive ablation occurs when large amounts of energy is deposited in a small time scale, so that none of the energy can thermally diffuse away, resulting in explosive ablation. Photochemical ablation, is usually applied to UV laser ablation, whereas thermal and explosive ablation regimes are the more likely candidates for IR ablation which is considered here.

The theoretical models behind explosive and thermal ablation models are also not well understood, with many models proposed to try and explain experimental results. These models range from heuristic models to sophisticated models that relate the underlying physical mechanisms to ablation damage. The two main heuristic models are: the blow off model, and the steady state model. The blow off model assumes that there is thermal confinement (i.e no propagation of heat in time  $t$ ), and that material is removed after the laser irradiation. There is a radiant threshold that has to be met to ablate material, and that Beer-Lambert's law describes the spatial distribution of light. For laser pulses of  $< 10$  ns, these conditions are normally met. However, for lasers with pulse length larger than this, these conditions are not usually met [89–91].

The steady state heuristic model, assumes that the pulse length is of the order of  $ms$  or larger, that material starts to be removed shortly after laser irradiation begins, and that some radiant threshold exists in order for ablation to begin. The steady state model also assumes that a fixed energy is required to remove a unit of tissue [89]. However, this does not always hold, as there are many circumstances where there is no one fixed energy, but rather many energies (due to various phase changes) that must be met in order for ablation to occur. There are also many other sophisticated models that try to describe what happens physically when ablation occurs [92–94].

Due to the above mentioned reasons, there is no defined ablation temperature. The literature, however, does suggest that it takes place when the tissue temperature is between 177 °C and 500 °C [93, 95, 96].

To model all these tissue damage processes the tissue damage model is split into two sections: coagulation damage and “physical” damage. Coagulation damage has no effect on the tissue’s

bulk optical or thermal properties. “Physical” damage changes the tissue optical and thermal properties.

### Modelling coagulation damage

With the description of the various processes that tissue undergoes during ablation, a numerical model of these processes can be created. First to model the full extent of the damage done under 100°C, i.e in the coagulation regime, the Arrhenius damage model is used. The Arrhenius damage model was originally used as a kinetic model of reaction products in chemistry [97]. It has since been adapted by various authors for modelling tissue damage, and is the *de facto* standard [98, 99]. These authors and various others, adapted this model by fitting Eq. (3.18) to experimental data for burn damage. The two parameters fitted are A, the frequency factor, and  $\Delta E$ , the activation energy.

$$\Omega(t) = \int_{t_i}^{t_f} Ae^{(-\frac{\Delta E}{RT})} d\tau \quad (3.18)$$

Where:

- $\Omega$  is the damage value [-];
- A is “frequency factor” [ $s^{-1}$ ];
- $\Delta E$  is activation energy [ $Jmol^{-1}$ ];
- R is the universal gas constant [ $Jmol^{-1}K^{-1}$ ];
- T is the temperature [K];
- and  $t_i$  and  $t_f$  are the initial time and final time at  $t_{crit}$ .

It is reported that a value of  $\Omega$  of 0.53, 1.0, and 10<sup>4</sup> relate to first, second, and third degree burns respectively [100]. The Arrhenius damage model is used to better understand the amount of damage caused by the laser in the non-ablated areas of tissue. Values of  $A = 3.1 \times 10^{98}$  and  $\Delta E = 6.3 \times 10^5$  are adopted [96, 98, 101].

### Modelling physical tissue damage

As tissue mostly consists of water [102] when the temperature of the tissue approaches 100°C (at 1 atm), water in the tissue begins to boil off. This acts as a large heat sink for the absorbed laser energy, slowing down the rate of ablation. The energy required to boil the water is  $Q_{vapor} = m_v \cdot L_v$ , where  $m_v$  is the mass of a voxel, and  $L_v$  is the latent heat of vaporisation. The energy to boil off the water is provided via the laser and heat diffusing into the voxel:

$$Q_{vapor} = \underbrace{laserOn(t) \cdot \dot{q} \cdot \Delta t \cdot V_{i,j,k}}_{\text{laser heating}} + \underbrace{c \cdot M_{i,j,k} \cdot \Delta T}_{\text{heat diffusion}} \quad (3.19)$$

Where:

- $Q_{vapor}$  is the current energy in Joules that has been used to boil off the water in the voxel [J];
- $laserOn$  is a boolean variable that determine if the laser is on or off [-];
- $\dot{q}$  is the energy absorbed by the voxel due to the laser [ $Wm^{-3}$ ];
- $\Delta t$  is the timestep [s];
- $V_{i,j,k}$  is the volume of the voxel labelled  $i, j, k$  [ $m^3$ ];
- $c$  is the heat capacity of the voxel [ $JK^{-1}$ ];
- $M_{i,j,k}$  is the mass of the voxel labelled  $i, j, k$  [ $kg$ ];

and  $\Delta T$  is the change in temperature the voxel would undergo, if the water was not boiling off.

As water boils off, the water content of each voxel changes. This affects the absorption coefficient, density, thermal conductivity, and heat capacity. Each of these vary with water content per voxel [103];

$$W = W_{init} - \left( W_{init} \cdot \left( \frac{Q_{current}}{Q_{vaporisation}} \right) \right) \quad (3.20)$$

$$\rho = \frac{1000}{W + 0.649 \cdot P} \quad (3.21)$$

$$c_p = 4.2 \cdot 10^3 \cdot W + 1.09 \cdot 10^3 \cdot P \quad (3.22)$$

$$\kappa = \rho \cdot (6.28 \cdot 10^{-4} \cdot W + 1.17 \cdot 10^{-4} \cdot P) \quad (3.23)$$

$$\mu_a = W \cdot \mu_{water} + \mu_{protein} \quad (3.24)$$

$$(3.25)$$

Where:

$W$  is the water content (i.e  $W = 0.7$  equates to 70% water content);

$W_{init}$  is the initial water content;

$Q_{current}$  is the total energy absorbed by the  $i^{th}$  voxel since the temperature reached 100°C [J];

$P$  is the protein content (i.e  $P = 1.0 - W$ );

$\kappa$  is the Thermal conductivity [ $Wm^{-1}K^{-1}$ ];

$c_p$  is the heat capacity [ $Jkg^{-1}K^{-1}$ ];

and  $\mu_a$  is the total absorption coefficient, and  $\mu_{water}$  and  $\mu_{protein}$  are the absorption coefficients of water and protein respectively.

$T_a$  is defined as occurring between 177 and 500 °C [93, 95, 96]. At  $T_a$  the tissue is removed and the thermal, optical, and physical properties set to that of air.

The updated damaged tissue structure is then fed back to the MCRT model and the whole process repeats until the predefined time limit is reached. This whole process of photon propagation, heat diffusion and tissue damage is outlined in Fig. 3.1.

### 3.2.4 Validation

#### Heat transport validation

To thoroughly validate the numerical method employed to solve the heat equation, the numerical method is compared against an easily solvable analytical case. The heat equation is solved on a cube, side L, in a surrounding medium of 0°C. The cube is initially at temperature 20°C and the temperature is calculated at various times. Thus, the boundary conditions are:

$$T(0, y, z, t) = T(x, 0, z, t) = T(x, y, 0, t) = 0^\circ\text{C} \quad (3.26)$$

$$T(L, y, z, t) = T(x, L, z, t) = T(x, y, L, t) = 0^\circ\text{C} \quad (3.27)$$

The thermal diffusivity ( $\alpha$ ), density ( $\rho$ ), and heat capacity ( $c_p$ ) are all set to 1. This corresponds to a material which has the thermal diffusivity between copper and aluminium [104, 105]. Assuming a separable solution in Cartesian coordinates yields:

$$\begin{aligned} T(x, y, z, t) = & (A_1 \cos(\alpha x) + A_1 \sin(\alpha x)) \cdot \\ & (B_1 \cos(\beta y) + B_1 \sin(\beta y)) \cdot \\ & (C_1 \cos(\gamma z) + C_1 \sin(\gamma z)) \cdot e^{-\alpha \mu^2 t} \end{aligned} \quad (3.28)$$

$$\mu^2 = \alpha^2 + \beta^2 + \gamma^2 \quad (3.29)$$

Applying the boundary conditions (Eqs. (3.26) and (3.27)) gives:

$$A_1 = B_1 = C_1 = 0 \text{ and } \alpha = \frac{\pi n}{L}, \beta = \frac{\pi m}{L}, \gamma = \frac{\pi p}{L} \quad (3.30)$$

$$\therefore T_{nmp}(x, y, z, t) = A_{nmp} \cdot \sin\left(\frac{\pi n x}{L}\right) \cdot \sin\left(\frac{\pi m y}{L}\right) \cdot \sin\left(\frac{\pi p z}{L}\right) \quad (3.31)$$

This yields the following solution for the heat equation using the principle of superposition, and solving Eq. (3.32) with  $f(x, y, z)$  as the initial temperature profile of the cube:

$$A_{nmp} = \frac{8}{L^3} \int_0^L \int_0^L \int_0^L f(x, y, z) \cdot \sin\left(\frac{\pi n x}{L}\right) \cdot \sin\left(\frac{\pi m y}{L}\right) \cdot \sin\left(\frac{\pi p z}{L}\right) dx \cdot dy \cdot dz \quad (3.32)$$

$$T(x, y, z, t) = \sum_{n=1,3,\dots}^{\infty} \sum_{m=1,3,\dots}^{\infty} \sum_{p=1,3,\dots}^{\infty} \frac{2368}{\pi^3 nmp} \cdot \sin\left(\frac{\pi n x}{L}\right) \cdot \sin\left(\frac{\pi m y}{L}\right) \cdot \sin\left(\frac{\pi p z}{L}\right) \cdot e^{(-\lambda^2 t)} \quad (3.33)$$

Where:

$$\lambda^2 = \alpha \pi^2 \left( \frac{n^2}{L^2} + \frac{m^2}{L^2} + \frac{p^2}{L^2} \right);$$

$n, m, p$  are odd integers;

and  $L$  is the length of the cube.

A slice through the middle of the cube,  $L = 50 \text{ cm}$ , yields Fig. 3.8, which shows that the numerical method matches the analytical solution closely.

### MCRT and heat transport validation

As a first test of the code, both MCRT and heat simulation, is compared to a simple analytical model of ablation. The simple model of ablation is as: the ablation energy ( $E_a$ ), is defined as the minimum energy required to raise the temperature of the medium to  $100^\circ\text{C}$ , and then boil off the water in a volume  $dV$ , mass  $M$ . Thus, in one dimension Eq. (3.34), where the symbols have their usual meanings. If the energy for ablation is delivered in a time  $dt$  by a laser of intensity ( $\text{Wcm}^{-2}$ ),  $P$ , this gives Eq. (3.35). Equation (3.35) can be rearranged to give an ablation front velocity, Eq. (3.36).

$$E_a = c_p \rho dx \Delta T + L_v \rho dx \quad (3.34)$$

$$P \cdot dt = \rho dx (c_p \Delta T + L_v) \quad (3.35)$$

$$u = \frac{P}{\rho(c_p \Delta T + L_v)} \quad (3.36)$$

Assuming the ablation front moves with constant velocity during the ablation, and using  $L_v = 2.53 \cdot 10^6 \text{ Jkg}^{-1}$ ,  $c_p = 4181 \text{ J} \cdot \text{kg}^{-1} \cdot \text{K}^{-1}$  and the medium is a cube side  $2 \text{ mm}$ , with a

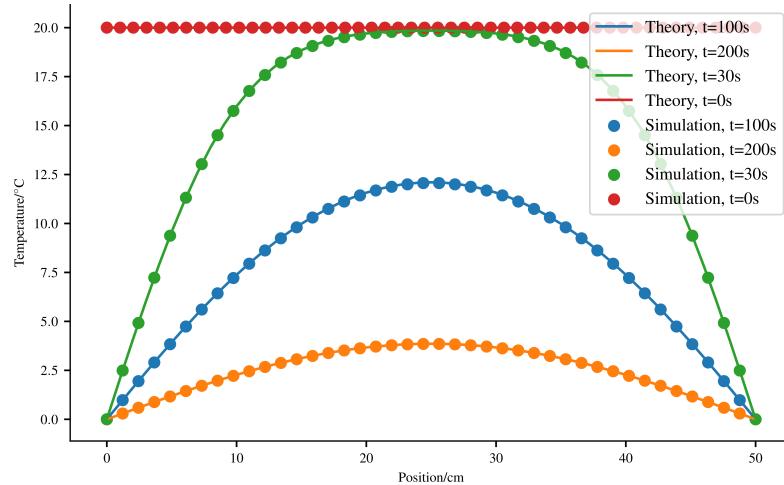


**Figure 3.8:** Temperature profiles of the cube for various times, comparing between analytical solution and numerical method.

starting temperature is  $37\text{ }^{\circ}\text{C}$  with a water content of 70% giving a density of  $700\text{ kg}\cdot\text{m}^{-3}$ . For these parameters this gives an ablation velocity,  $u \simeq 0.77\text{ cm}\cdot\text{s}^{-1}$ , and a time to ablate through 2 mm of tissue of  $\simeq 0.26\text{ s}$ . As the code developed in this chapter simulates the diffusion of heat in a medium due to an incident laser, the expected time to ablate through the same medium should be slightly larger as heat diffuses away from the voxel while it is being heated. When the full heat + MCRT code is used to simulate this experiment, it gives a time,  $t \simeq 0.33\text{ s}$ .

### 3.3 *In silico* results

#### 3.3.1 Introduction

To match the experimental results, an accurate model of the experimental setup *in silico* must be created. However, due to computational constraints, such as memory and time available, some approximations to the experimental set-up have to be made. The porcine skin was a large thin slice of the top most layers of the skin. However, as the area of interest is where the ablation occurs, initially the porcine skin is modelled as a cuboid, dimensions:  $1.1 \times 1.1 \times 0.5\text{ cm}$ . The initial temperature of the porcine skin is assumed to be around  $5\text{ }^{\circ}\text{C}$ , as the tissue was kept on ice or was kept cooled. As mentioned in the previous sections, there are several unknowns in the model:  $T_a$ , water content, temperature of air after ablation, and the exact thermal and optical properties of the porcine tissue. Therefore several models are run so that the full parameter space of these unknowns can be explored. Results from these *in silico* experiments are presented in this section along with a comparison of the model to the experimental work carried out in collaboration with the University of Dundee and the Photobiology department at Ninewells Hospital.

#### Optical & thermal properties

The thermal and optical properties of porcine tissue are not known exactly for any given tissue sample. As such the thermal and optical properties used in this section are taken from various literature sources.

	Thermal conductivity, $\kappa$	Density, $\rho$	Heat capacity, $c$
Tissue	$\rho \cdot (6.28 \cdot 10^{-4} \cdot W + 1.17 \cdot 10^{-4} \cdot P)$	$\frac{1000}{W+0.649 \cdot P}$	$4.2 \cdot 10^3 \cdot W + 1.09 \cdot 10^3 \cdot P$
Air	$a e^{-b(T-273.15)} + c$	$\frac{p_{atm}}{R_{spec}T}$	1006

**Table 3.1:** Optical and thermal properties for porcine tissue and air.  $W$  and  $P$  are the percentage of water and protein respectively.  $\rho$  is the density of the skin,  $p_{atm}$  is the pressure of air at 1 atmosphere, and  $R_{spec}$  is the gas constant.  $a$ ,  $b$ , and  $c$  are constants.

The laser used in the experimental work is an CO<sub>2</sub> laser operating at 10.6  $\mu m$ . This means that the optical properties of the tissue are dominated by water absorption. The laser used in the experiment is the Pixel CO<sub>2</sub> [106]. The Pixel CO<sub>2</sub> laser has a wavelength 10.6  $\mu m$  which corresponds to an absorption coefficient in water of  $\sim 850\text{ cm}^{-1}$ . As the absorption coefficient is large, it is assumed that scattering is negligible at these wavelengths. Table 3.1 summarises the thermal properties for tissue and air used in the simulations.

The laser was used in “Pixel beam” mode. This means that the laser beam is split into an array of smaller beams. The laser used an array  $9 \times 9$  of 81 pixel beams, each with a diameter of 250  $\mu m$ . The Pixel CO<sub>2</sub> rated laser power is  $\sim 70\text{ W}$ .

The laser delivered one single pulse of varying total energy delivered over the range 50  $mJ$  to 400  $mJ$ , in so called “super pulsed mode”. The experiment consisted of ablating the porcine tissue, as a function of energy per “pixel” beam. This was achieved by adjusting the pulse length of the laser,  $\tau$ , so that the energy per pulse was varied over a range 50  $mJ$  to 400  $mJ$ .

### Computational speed up:

As discussed in the Section 3.1, the volume of interest is the area around the ablation craters. The volume is  $1.1\text{ cm} \times 1.1\text{ cm} \times 0.5\text{ cm}$ . However, for the simulation to have good resolution of the ablation craters this volume would require many voxels for the tissue model. This is unfeasible due to: the memory required to store the various counters, grids, and variables, and the time that would be required to carry out the computation. Thus, the volume of interest is reduced to focus on just one of the ablation craters that is created by the laser (a volume of  $0.06\text{ cm} \times 0.06\text{ cm} \times 0.18\text{ cm}$ ) As a check to ensure that no physical phenomena are omitted by focusing on just one ablation crater, an initial simulation that models the full volume of interest was carried out to investigate the possibility of overlapping craters or other related phenomena. The simulation, as shown in Fig. 3.9, gives reassurance that the shrinking of the volume of interest is a valid approximation to make as there is no overlap between the separate ablation crater.

### 3.3.2 Results

#### Investigating ablation temperature, $T_a$

Various literature sources report the ablation temperature ranging widely from 177° to 500° [93, 95, 96]. Thus, several models are run over this range to establish the  $T_a$  which fits the experimental results. Figures 3.10 and 3.11 show how  $T_a$ , and beam profile affect the crater depth as a function of pixel beam energy for the CO<sub>2</sub> laser. The data suggests that a  $T_a$  around  $T_a = 500\text{ }^\circ C$  is appropriate for the studies carried out, the upper limit of  $T_a$  from the literature.

Increasing the ablation temperature has the obvious effect of requiring more energy to be deposited by the laser before ablation takes place. This also allows more heat to diffuse away from the ablation crater increasing the thermal damage done to the surrounding tissue. Decreasing the ablation temperature has the converse effect, and allows the ablation crater to become deeper.

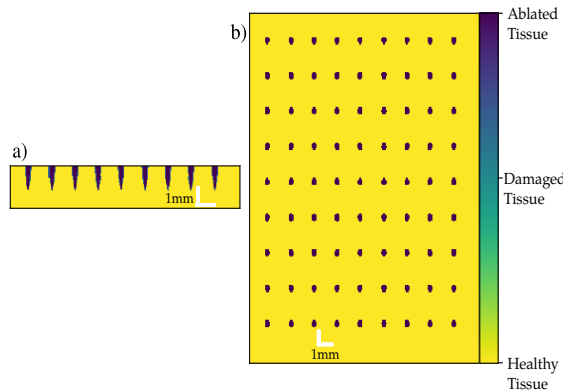


**Figure 3.9:** Simulation of 81 pixel beams. Figure a) shows a slice through the optical properties at the end of the simulation in the  $z$ - $y$  plane. Figure b) shows the optical properties in the  $x$ - $y$  plane at the top surface. Yellow is unchanged tissue, and purple is completely ablated tissue. Figure shows that the ablation craters do not overlap one another.

Over the full range of  $T_a$ , as the energy per pixel beam increases, there is a trend that at higher energies the crater depth begins to taper off. This is potentially due to several reasons. As the ablation craters grows the volume of tissue that is ablated is replaced with air, allowing more heat loss from the tissue to the environment. As well as heat loss to the environment, more heat is diffused away into the surrounding tissue as the crater grows, due to the availability of more tissue for the heat to diffuse into.

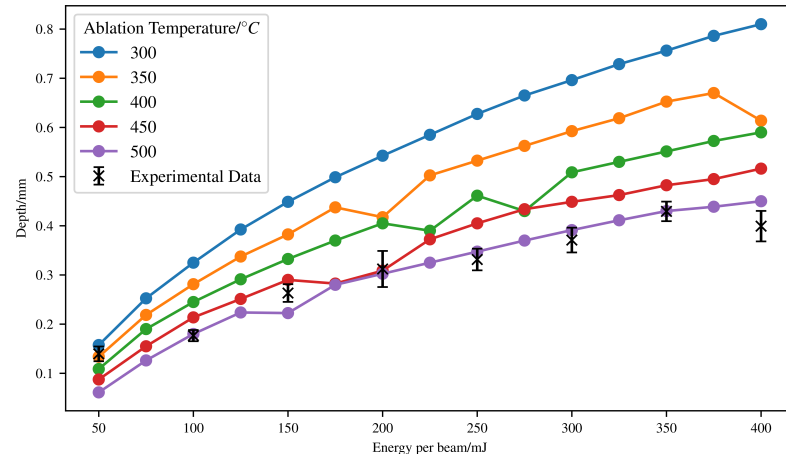


**Figure 3.10:** Simulation of 70 W  $CO_2$  ablative laser, with a circular beam profile. Crater depths as a function of pixel beam energy for various  $T_a$ 's.

### Investigating beam type

As the manufacturer does not provide information on the beam profile of the pixel beams and the lack of equipment available to measure the beam profile, the shape of the beam profile has to be assumed. Two different beam types are tried: Gaussian and circular (top-hat). Figures 3.10

and 3.11 show the result of these *in-silico* experiments. The Gaussian beam ablates deeper holes than the circular beam type, which is to be expected due to the distribution of power in the Gaussian beam. The beam that best fits the data is the circular beam. For the Gaussian beam to fit the data ablation would have to take place at temperatures above 500 °C which does not fit with the literature. Without knowing the exact profile of the beam, it is assumed for the rest of the *in-silico* experiments that the beam profile is circular.

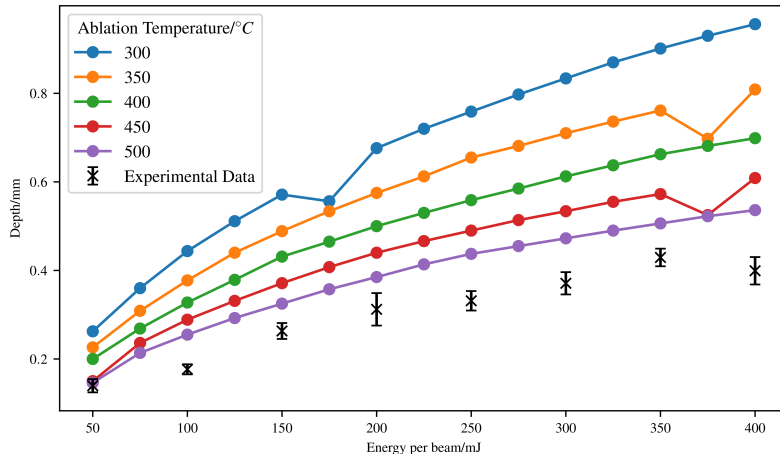


**Figure 3.11:** Simulation of 70 W CO<sub>2</sub> ablative laser, with a Gaussian beam profile. Crater depths as a function of pixel beam energy for various T<sub>a</sub>'s.

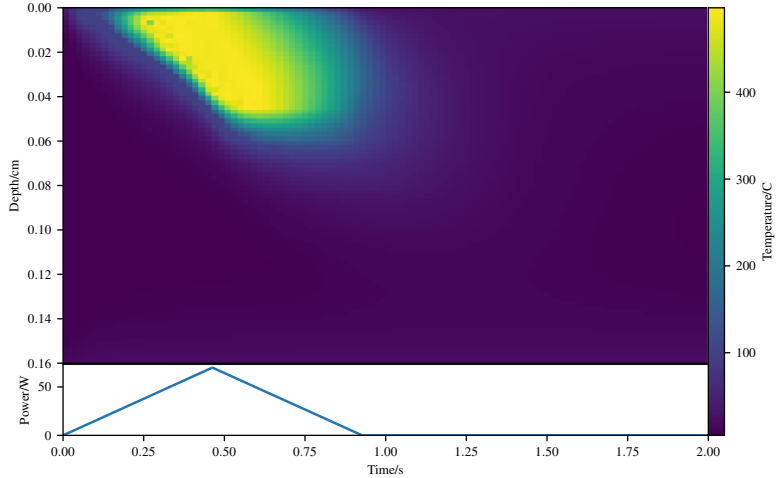
### Temperature during ablation

Figure 3.12 shows slices of temperature as a function of time during a simulation for T<sub>a</sub> = 500 °C. This means that every column of pixels shows a bore hole through the medium (along the z axis) for a given time. Figure 3.12 also shows the laser pulse profile as a function of time as a reference so that knowledge of when the laser is on or off is easily elucidated. The figure shows that the temperature reaches a maximum temperature which is equal to T<sub>a</sub>, regardless of ablation progress. This maximum temperature is researched roughly 0.25 s into the simulation, and lasts until ~0.75 s. The maximum temperature reaches a depth of around 0.04 cm into the tissue. The region where water is boiling can be seen by the evidence of the “dark valley” before the abrupt jump in temperature to the maximum temperature.

The cause of this dark valley is due to the water in the tissue acting as a heat sink. The water needs a large amount of energy to boil off, thus it stops the temperature from increasing until it boils off, giving rise to this dark valley. This temperature maximum extends for a small distance into the tissue, before diffusion spreads it out. Once the tissue ablates the ablated volume cools over the period of around 0.5 s. Ablation continues until around 0.6 s, where the laser power has past its maximum value and no more ablation occurs.

### Investigating thermal damage

As stated in Section 3.2.3, the Arrhenius damage integral is used to estimate the thermal damage due to the laser. To calculate the tissue damage around the ablation craters, Eq. (3.18) is first transformed into a summation:



**Figure 3.12:** Temperature bore hole through centre of medium as a function of time, for  $T_a=500\text{ }^{\circ}\text{C}$ . Laser power is also plotted for comparison.

$$\Omega(t) = \int_{t_p}^{t_f} Ae^{-\frac{\Delta E}{RT}} d\tau \quad (3.37)$$

$$\Omega(t) = \sum_{m=m_p}^{m_f} Ae^{-\frac{\Delta E}{RT_\xi^m}} \Delta t \quad (3.38)$$

Where:

$\Delta E$ ,  $R$ ,  $T$ , and  $A$  have the same meanings as before;

$\xi$  is the  $i^{th}, j^{th}, k^{th}$  node;

and  $m_p$  is the  $p^{th}$  timestep when the  $\xi^{th}$  node is above the threshold temperature.

Using Eq. (3.38) it can thus be estimated that the damage to the tissue on a voxel basis. Figure 3.14 shows how far the thermal damage extends around the ablation crater. For ease of visualisation 1-3 is mapped to their respective burns via the following scheme, with  $\eta$  as burn severity:

$$\eta = \begin{cases} 3, & \Omega \geq 10000 \\ 2, & 1 \leq \Omega < 10000 \\ 1, & 0.53 \leq \Omega < 1 \\ 0, & 0.0 \leq \Omega < 0.53. \end{cases} \quad (3.39)$$

As shown in Fig. 3.14, the thermal damage zone extends for a small distance around the ablation crater, due to the diffusion of heat into these areas. Figure 3.13 shows the maximum horizontal thermal damage distance as a function of  $T_a$ , and pixel beam energy. For values of  $T_a$  less than  $\sim 425\text{ }^{\circ}\text{C}$ , it appears that the maximum horizontal extent of the thermal damage tapers off. This is most likely because for lower values of  $T_a$ , there is a larger ablation crater, meaning that the energy from the laser is deposited deeper in the tissue in comparison to higher values of  $T_a$ . The higher values of  $T_a$  allow greater diffusion of the heat, thus yielding larger

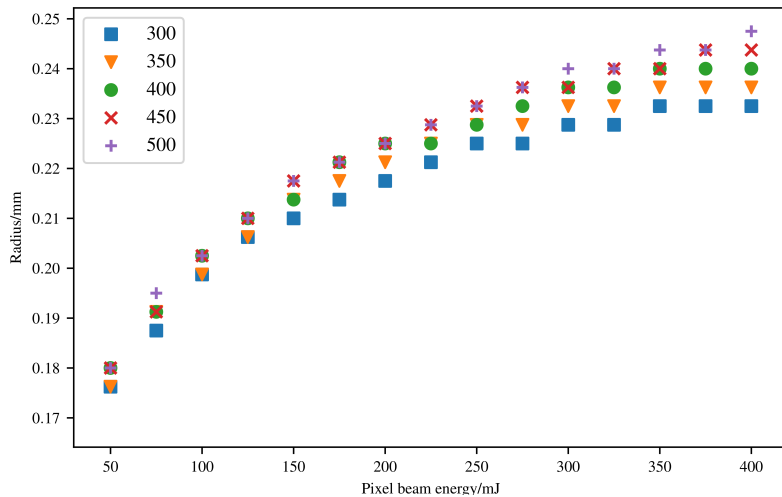


**Figure 3.13:** Figure shows the maximum horizontal extent of thermal damage as a function of energy per pixel beam, for different  $T_a$ 's.

zones of damage. Overall there is little difference in the maximum horizontal extent of thermal injury, when using different energies (of the order of  $\sim 0.01$  mm).

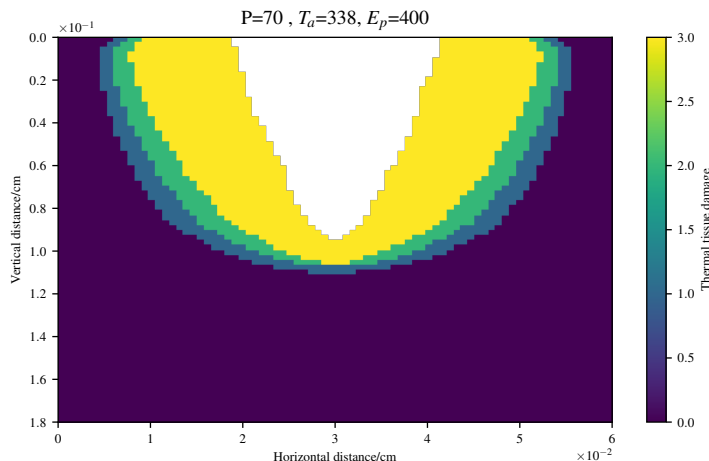


**Figure 3.14:** Tissue thermal damage around the ablation crater (white). Thermal tissue damage values of 3 refer to 3<sup>rd</sup> degree burns, 2 to 2<sup>nd</sup>, and 1 to 1<sup>st</sup> degree burns respectively.  $P$  is the power in Watts,  $T_a$  is the ablation temperature in Kelvin, and  $E_p$  is the energy per pixel beam in mJ.

Investigations for the time it takes for different areas of the tissue to become thermally damaged, were also carried out. This can be easily achieved by saving the time each voxel passes one of the damage boundaries in Eq. (3.39). Figures 3.15 and 3.16 show the minimum time taken for 1<sup>st</sup>, 2<sup>nd</sup>, and 3<sup>rd</sup> degree burns to occur as a function of depth. Figure 3.15 shows that there is little to no time (upon the order of 0.5 ms) between 1<sup>st</sup> and 2<sup>nd</sup>, and 3<sup>rd</sup> degree burns. Figure 3.16 shows there is a slightly greater time difference between 1<sup>st</sup> and 2<sup>nd</sup>, and 3<sup>rd</sup> degree

burns, however this is almost as negligible as the 400 mJ case.

The reason that there is almost no time between 1<sup>st</sup> and 2<sup>nd</sup>, and 3<sup>rd</sup> degree burns, is most likely because there is little time for heat to diffuse, whilst the laser is still illuminating the medium. The laser pulses are on the order of seconds, and tissue is not thermally conductive. This leads to the results presented here.

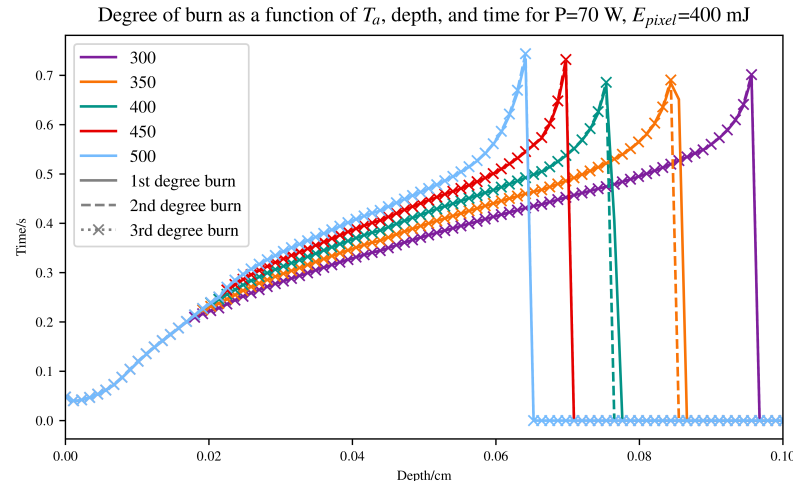


**Figure 3.15:** Figure show the time taken for 1<sup>st</sup>, 2<sup>nd</sup>, and 3<sup>rd</sup> to occur as a function of depth, for a range of  $T_a$ 's at 400 mJ.

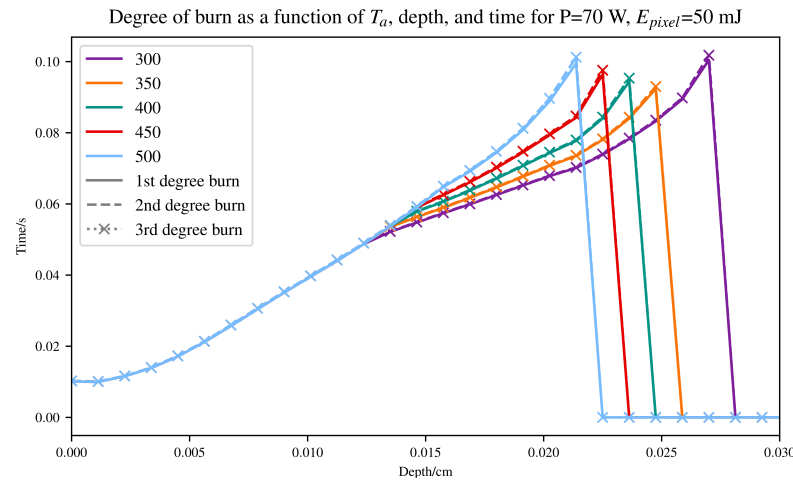


**Figure 3.16:** Figure show the time taken for 1<sup>st</sup>, 2<sup>nd</sup>, and 3<sup>rd</sup> to occur as a function of depth, for a range of  $T_a$ 's at 50 mJ.

### Investigating laser pulse profile

Pulsed lasers have a variety of pulse profiles. The pulse profiles are usually modelled as triangular, tophat, or Gaussian. However, the pulse profiles in reality are normally less well defined, and rather the pulse profile is something in between these perfect models.

The laser used in the above experiments, the Pixel CO<sub>2</sub>, states that it has a triangular pulse profile for the laser pulses. Thus, in this section the effect of the laser pulse profile has on ablation

and the surrounding thermal injury is investigated.

Three different laser pulses profiles are investigated: tophat, triangular, and a Gaussian profiles. The Gaussian profile used has approximately the same area as the two other pulses.

Figure 3.17 show the pulse profiles for a pulselength of 0.2 s. From Fig. 3.18 the tophat pulse profile causes the most ablation, where as the Gaussian pulse causes the least. This can be explained by the fact that the Gaussian pulse delivers energy over a longer time span, thus letting heat diffuse away before it can “build” up and cause damage, and thus ablation.

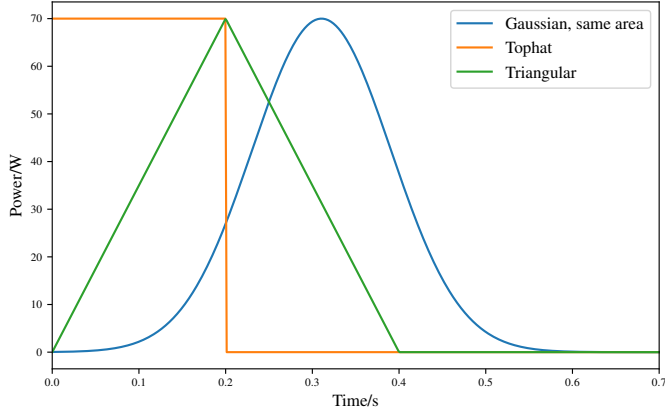


**Figure 3.17:** Comparison of the different pulse profiles trialled for a pulselength of 0.2 s.

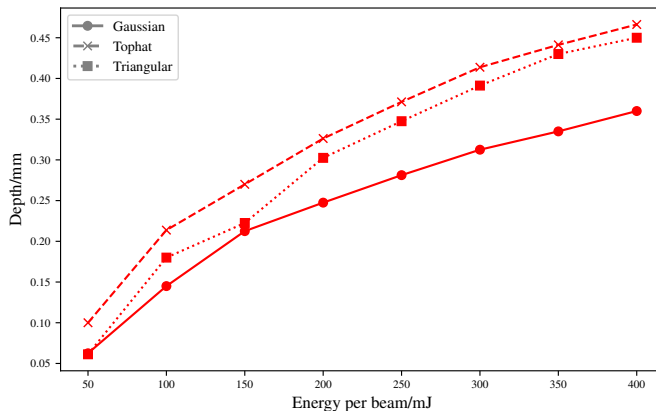


**Figure 3.18:** Comparison of various pulse shapes for the pixel beams. Figure shows ablation depths for  $T_a=500\text{ }^{\circ}\text{C}$ .

### Investigating Initial Temperature

As the experiment was carried out on porcine tissue that was kept on ice before the experiment was conducted, we assumed that the initial temperature of the porcine tissue was around  $5\text{ }^{\circ}\text{C}$ . This section investigates whether this is an accurate assumption.

To investigate this, three different temperatures were trialled:  $0\text{ }^{\circ}\text{C}$ ,  $5\text{ }^{\circ}\text{C}$ , and  $25\text{ }^{\circ}\text{C}$ . These temperatures correspond to room temperature, the temperature of ice and the original temperature we assumed. Figure 3.19 shows the results of this *in-silico* investigation.

As expected, the hotter the porcine skin is initially the larger the ablation depth. This occurs as less energy is required to bring the porcine skin to its ablation temperature. In the previous

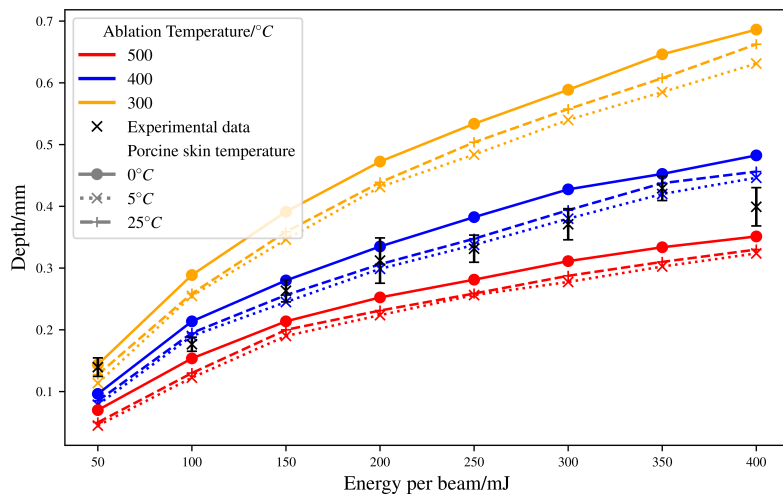


**Figure 3.19:** Comparison of ablation depths for different initial temperatures in porcine skin.

subsections it was assumed that the temperature of the porcine skin was around  $5\text{ }^{\circ}\text{C}$ . This assumption was based upon the fact that the porcine skin was kept on ice before the experiment, thus the temperature of the skin must be between 0 and room temperature. This investigation shows that over small variations of temperature ( $\lesssim 5\text{ }^{\circ}\text{C}$ ), the ablation depth does not vary too much (on the order of  $\approx 0.01\text{ mm}$ ).

However, there is a greater difference in the maximum extent of thermal damage to the skin for different initial temperatures in porcine skin. Figure 3.20 shows this difference.

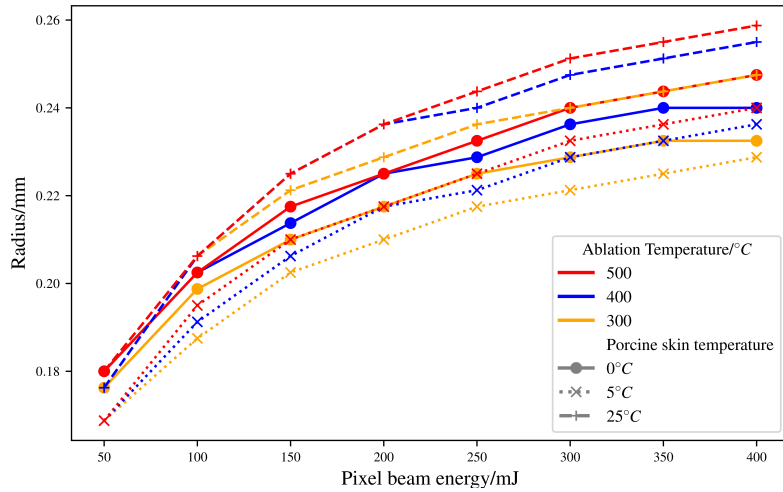


**Figure 3.20:** Comparison of maximum horizontal damage distance for different initial porcine skin temperatures.

## Investigating Voxel Temperature After Ablation

In the previous section it is assumed that the temperature of a voxel remains unchanged after the tissue is removed from that voxel via ablation. However, this assumption may not be accurate. To test if the temperature of the voxel after ablation affects the depth of ablation or thermal injury to the surrounding tissue various voxel temperature were tried. Two different temperatures were tried: half the ablation temperature and room temperature ( $\approx 25^{\circ}\text{C}$ ). Figure 3.21 shows the effect of the voxel temperature after ablation has on the ablation depth.

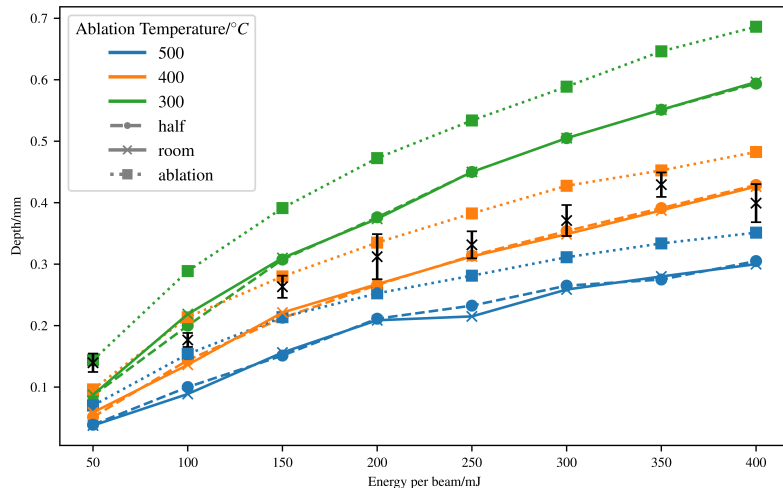


**Figure 3.21:** Comparison of different voxel temperatures after ablation. Half refers to setting the temperature of a voxel to half that of the ablation temperature. Room refers to room temperature, and ablation leaves the temperature at the ablation temperature.

Setting the voxel temperature to either half the ablation temperature or to room temperature has a large effect on the ablation depth, with a difference of  $\approx 0.1\text{ mm}$ . However, there is a small difference between setting the voxel temperature to room temperature and to half of the ablation temperature though.

## 3.4 Application of Model for Spy Disposal

In the 1964 James Bond film Goldfinger, James Bond is threatened with a laser by the titular antagonist (see Fig. 3.22). Would this laser actually cut Bond in half as the film implies, and could Goldfinger be more humane<sup>†</sup> in his choice of laser for the task?

As the first laser was demonstrated in 1960 was a ruby laser of  $694\text{ nm}$ , with the film being released in 1964 and the “laser”<sup>‡</sup> shown on screen being red, the likely laser portrayed is a ruby laser.

To assess whether Bond would die due to the laser we used the model outlined in this chapter with the following parameters.

As Auric Goldfinger uses this laser to cut sheets of gold, we assumed the power of the laser was around 1 kW, as industrial lasers used to cut metal, are high powered continuous operation lasers. We assumed that the Bond is completely made of skin, with no organs or bones. We ran

<sup>†</sup>i.e could Goldfinger use a laser that would lessen Bond’s suffering.

<sup>‡</sup>A laser was not used on set, but rather was added in post-production.

two simulations, one for the Ruby  $694\text{ nm}$  and one for the  $CO_2$   $10.6\text{ }\mu\text{m}$ . For the  $CO_2$  as before there is no scattering due to high absorption coefficient. The Ruby laser's wavelength is highly scattering, so we model both scattering and absorption. The medium we model is a  $2\text{ cm}^3$  cube of homogeneous skin.

We found that the  $CO_2$  takes  $22\text{ ms}$ , and Ruby takes  $11\text{ s}$  to ablate through the  $2\text{ cm}$  medium. From timing the movie, the laser moves at a round  $1\text{ cms}^{-1}$ . Therefore the Ruby laser used by Goldfinger would only give Bond some serious burns, but would leave him in one piece. If Goldfinger used a  $CO_2$  laser then Bond would have been cleanly cut in two.



**Figure 3.22:** Still image of the iconic laser scene in the film Goldfinger. Copyrights Eon Productions.

### 3.5 Conclusion

Using MCRT and a finite difference method, a fully 3D model of photon and heat transport within tissue has been created. This model can be used to simulate the heat deposited by laser, the ablation craters formed via high powered lasers and the resultant thermal damage surrounding the ablation crater.

The model has been fully compared with both analytical solutions and experimental results. The model was found to match with experimental results that a tissue ablation temperature  $T_a$  of around  $500\text{ }^\circ\text{C}$  has to be adopted, toward the higher end of the range previously observed in the literature.

The simulations allow us to predict for a given laser power and pulse length, how much thermal damage is caused in the tissue, and how deep an ablation crater that will form. The computational model could be used in future to help develop treatment regimes for both aesthetic and medical procedures. For example, currently there is considerable amount of “down time” after skin rejuvenation, in which the patient displays inflammation, erythema, edema, pain, and crusting [107–109]. Simulations of thermal damage due to fractional ablation could help design treatment regimes that minimise these effects, whilst still delivering skin rejuvenation. The model can also be applied to help optimise laser assisted drug delivery. Laser assisted drug delivery uses lasers to drill holes into the skin to help promote topical drug diffusion into the skin. Our model can help predict the laser parameters needed to reach a certain hole depth, thus minimising thermal damage and pain to patients.

There are many avenues available with regards to future work on this model. The model presented here in this chapter was on an initially homogeneous skin model. In reality skin is composed of several distinct layers, with each layer containing varying amounts of different

chromophores. Our model can easily incorporate an multi-layered skin model complete with various fractions of chromophores. However, as the laser used in these studies is an infra-red laser, water is the highest absorbing chromophore, meaning that a physically accurate model, with various chromophores is not need for this application. The current model is a voxel based model, where all the voxels are the same size. This allows the model presented in this chapter to be easily set-up, with regards to parallelisation, optical/thermal properties and ease of programming. However, voxel models, where all the voxels are the same size, are not computationally efficient. Particularly in order to achieve good resolution, many voxels are needed, which requires large amounts of RAM, due to a  $\sim n^3$  scaling of voxels to memory in 3D. A more efficient way, would be to allow different sizes of voxels, depending on parts of the model which need high resolution, and parts that do not need high resolution. Such a voxel model is called an adaptive mesh refinement (AMR). There are downsides to AMR: complex implementation for parallelisation and set-up of optical/thermal properties, slower optical depth integration routines due to neighbour lookups.



## Chapter 4

# Quasi-wave/particle Monte Carlo Algorithm, $\varphi MC$

### 4.1 Introduction

Complex shaped light beams have been used in a wide variety of applications in biophotonics and medicine. From using Airy beams to move particles and cells [110], Bessel beam “tractor beams” [111], Airy and Bessel beams for better field of view in light-sheet microscopy [112], and utilising Laguerre-Gaussian beams to optical trap optically reflective particles [113].

However, simulation techniques for modelling complex shaped beams in biological tissue is lacking. Currently there are several techniques that can model these beams in biological tissue, however they all have downsides. These methods include diffusion approximation to the RTE, finite difference time domain (FDTD), pseudo-spectral time-domain (PSTD), beam propagation methods (BPM), and MCRT.

As discussed in [Diffusion Approximation](#) section, the diffusion approximation has many issues when it comes to modelling light propagation in biological tissue. FDTD involves using a finite difference method to solve Maxwell’s equations. This is computationally intensive and requires a grid resolution of  $\sim \lambda/20$  and thus most models are restricted to 2D [114, 115]. PSTD like the FDTD is also computationally intensive, though to a lesser extent [114]. Beam propagation method (BPM) is a fairly computational efficient method of propagating light beams, compared to FDTD or PSTD. However, the BPM uses the slowly varying envelope approximation, which limits some of the problems it can be applied. BPM is also generally a uni-directional propagation method, though it can be adapted to model bidirectional propagation, this can lead to issues in the model’s accuracy [114, 116].

The final method, MCRT, in general, cannot model complex beams where the wave-like behaviour of photons is required to form, or propagate the beam. For example, traditional MCRT methods cannot model Gaussian beams, as Gaussian beams have a finite beam waist at their focus (see Fig. 4.6). MCRT (along with geometric optics) predicts that Gaussian beams have an infinitely small waist.

Various authors have tried to model complex beams that require wavelike behaviours using MCRT. Some of the techniques used by these authors include: artificial beam steering [117], generating skew rays [118], complex ray tracing [119], decomposition [120], electric field Monte Carlo [121], and wavefront tracing [122]. However, all these techniques either inaccurately model Gaussian beams, can model Gaussian beams but are complex to implement or computational

intensive (more so than MCRT usually is). There have been some attempts at using the techniques presented in this chapter, to modify MCRT algorithms into algorithms that can model diffraction and interference [123–127]. These authors have good results, but either do not detail their methods, do not attempt to treat scattering or are in the x-ray regime.

This chapter modifies the MCRT method, from a “ballistic” photon method into a quasi-ballistic/wave photon method so that the wave behaviour of photons can be modelled. This algorithm,  $\varphi MC$ , allows the modelling of complex shaped beams such as Bessel beams and Gaussian beams, without much modification of the underlying MCRT code.

We present a thorough investigation of the method used to turn a ballistic regime MCRT method in to a quasi-wave/ballistic method. The method is validated against theoretical and experimental data for various different beam types including: Bessel (including higher orders), and Gaussian beams. Treatment of the propagation through scattering media is also discussed.

## 4.2 Theory

To convert a MCRT simulation to be able to model wave-like behaviour of photons, we introduce two concepts: tracking the complex phase of packets and the Huygens-Fresnel principle. This section presents a description of the modifications to the traditional MCRT algorithm, alongside the theoretical background to both the concepts.

### 4.2.1 Complex Phase Tracking

The first concept we add to the MCRT method is assigning a complex phase to each packet. The phase is given to a packet at the beginning of the simulation depending on the input field. The packet is also given an initial electric field of the form:

$$E_0 = \frac{1}{N} \sqrt{\frac{P}{A}} \quad (4.1)$$

Where  $N$  is the number of packets run in a simulation,  $P$  is the power of the incident beam, and  $A$  is the area of the beam. This initial electric field is needed to compare different beams as in Section 4.6, and to normalise for number of packets run.

The phase is then tracked as the packet moves through the medium, over a distance  $l$ . Equation (4.2) shows how the phase is calculated.

$$\varphi = \cos\left(\frac{2\pi l}{\lambda}\right) + i \sin\left(\frac{2\pi l}{\lambda}\right) \quad (4.2)$$

Where  $\varphi$  is the complex phase of a photon packet,  $l$  [m] is the distance the packet has travelled,  $\lambda$  [m] is the wavelength of the packet. Now we can calculate the complex phase of a packet at a position  $P_o$ , if we know the distance it has travelled, and its original phase, see Fig. 4.1.

To model interference, we let the photon packets interfere with one another in a volume or area element. We do not model the interference at a point in space where photon packets cross, due to the ballistic nature of the MCRT simulation this does not occur with enough frequency to give a good signal to noise ratio. Therefore, interference takes place in a volume,  $dV$ , or area element,  $dA$ , instead. To calculate the intensity from the complex phase, the absolute value of the phase is squared. Therefore, to calculate the intensity for a given voxel or area, the phase is first summed in each voxel or area before the absolute value is squared. Equation (4.3) shows the equation for intensity for a volume element  $dV$ . A similar relation for calculating the interference on an area element  $dA$  also exists.

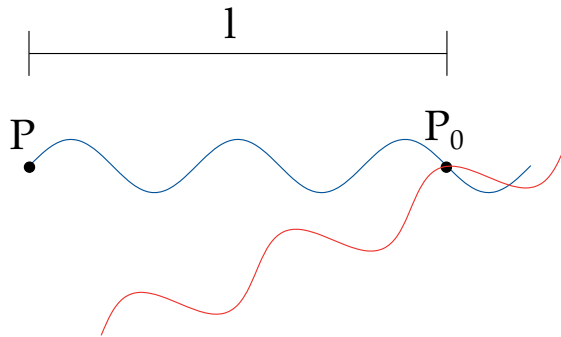


**Figure 4.1:** Example of phase calculation when a photon has travelled a distance  $l$ . The figure also shows an example of interference between two photons via addition of the complex amplitudes at the point  $P_0$ .

$$I(\zeta) = \left| \sum_{\zeta} E_0 \cos\left(\frac{2\pi l}{\lambda}\right) + i \sum_{\zeta} E_0 \sin\left(\frac{2\pi l}{\lambda}\right) \right|^2, \quad \zeta = (x, y, z) \quad (4.3)$$

Where:

- $l$  is the total distance travelled by a photon [m];
- $\lambda$  is the wavelength of the photon [m];
- $I$  is the intensity at the  $\zeta^{th}$  cell [ $Wm^{-2}$ ];
- $E_0$  is the initial electric field of the packets as in Eq. (4.1) [ $Vm^{-1}$ ]
- and  $\zeta$  is the  $x^{th}$ ,  $y^{th}$ ,  $z^{th}$  cell, volume  $dV$ .

In addition to tracking the phase, the next principle needed to simulate the wave behaviour of light in MCRT is the Huygens-Fresnel principle.

#### 4.2.2 Huygens-Fresnel Principle

The Huygens-Fresnel principle is a method that is used to help model the propagation of waves in the far field limit and the near field limit. The Huygens principle was first postulated in 1678 and states [128–130]:

*“Every point on a propagating wavefront serves as the source of spherical secondary wavelets, such as the source at some time later is the envelope of these wavelets.”*

The principle is illustrated in Fig. 4.2. The principle allowed Huygens to derive laws of refraction and reflection, but it failed to describe diffraction effects. This led to Augustin-Jean Fresnel in 1818, combining the Huygens principle with his own theory of interference [130, 131]. This Huygens-Fresnel principle, gave an accurate description of the propagation of light and diffraction effects. This was achieved by allowing the secondary wavelets to self interfere, giving rise to an accurate description of the physical phenomena. Later, Gustav Kirchhoff gave a rigorous mathematical description of the Huygens-Fresnel principle, which is the basis of diffraction theory [132, 133].

The Huygens-Fresnel principle allows the modelling of diffraction in both the near and far field. As the principle states that every point on the wavefront is a source of secondary spherical waves, this implies that there are “backward” waves. These “backward” waves are un-physical, and there is no experimental evidence of their existence. Thus, Fresnel introduced an inclination

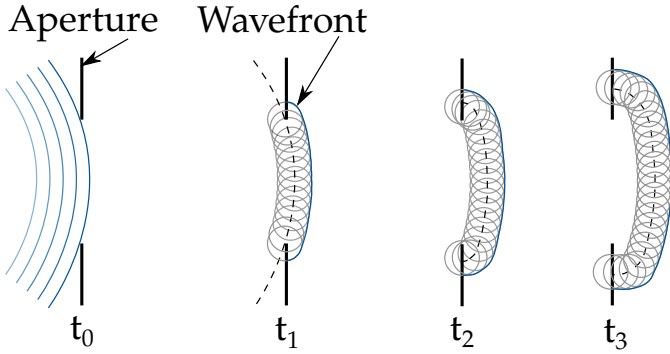


**Figure 4.2:** Illustration of the Huygens-Fresnel principle. At  $t_0$  a wave is incident on an aperture. Times  $t_1$ ,  $t_2$ , and  $t_3$  show the evolution of the wavefront using the Huygens-Fresnel principle. Dashed lines illustrate the wavefront position at the previous time step, and is the source of the Huygens-Fresnel wavelets.

factor to eliminate these “backward” waves. This inclination factor was later put on a rigorous mathematical standing by Kirchoff, as it naturally fell out of his theory [132,133]. Equation (4.4), the Rayleigh-Sommerfeld diffraction integral of the first kind\*, shows the equation for the complex field at a point on a plane.

$$u(\mathbf{r}_1) = \frac{1}{i\lambda} \int \int u(\mathbf{r}_0) \frac{\hat{s}_0 \cdot (\mathbf{r}_1 - \mathbf{r}_0)}{|\mathbf{r}_1 - \mathbf{r}_0|^2} e^{ik|\mathbf{r}_1 - \mathbf{r}_0|} dS_0 \quad (4.4)$$

Where:

- $u$  is the complex electric field [ $Vm^{-1}$ ];
- $\lambda$  is the wavelength [ $m$ ];
- $S_0$  is a plane with surface normal  $\hat{s}_0$  [-];
- $k$  is the wavenumber [ $m^{-1}$ ];
- and  $\mathbf{r}_n$  are spatial coordinates [-].

The Huygens-Fresnel principle is implemented by sampling the light source on the surface of any lens or in a slit. In practise this means when for example, a plane wave is incident on a slit width  $a$ , and length  $b$ , the slit area is uniformly sampled for the initial position of the photon packets. The packets are then given a random direction, sampled toward the detector thus avoiding the non-existent “backward” waves. For the case of modelling propagation through a lens, the usual geometric optics approach is taken to propagate the packets through the lens. When the packet lies on the surface of the lens, the Huygens-Fresnel principle is invoked, and the packet is given a random direction (in the direction of the medium) and propagated as usual.

Our algorithm uses the Huygens-Fresnel principle and the tracking of complex phase to simulate diffraction effects, that would otherwise be absent from the simulation. The principle allows the algorithm to calculate the complex amplitude at a point, and thus the intensity at that point, essentially numerically simulating Eq. (4.4). These two concepts underpin the algorithm that allows various complex beams, and wave phenomena to be simulated within a ballistic method. The following sections validate the method against the theory and experimental data for propagation of various complex beams.

---

\*If diffraction occurs in a plane, the Kirchoff diffraction integral can be modified to this

### 4.2.3 Validation of Phase Tracking Algorithm

#### Double Slit Experiment

The first test of our quasi-wave/particle MCRT algorithm<sup>†</sup>,  $\varphi MC$ , is to compare our simulation to a double slit experiment. The double slit experiment, is a simple experiment where a monochromatic plane wave of light is incident on two slits distance apart  $d$ , and width  $b$ , and an interference pattern is observed on a screen a distance  $L$  away from the slits. The experiment is usually carried out with the detector screen in the far field (the so called Fraunhofer regime). The intensity pattern on the detector screen is as in Eq. (4.5):

$$I(x) \propto \cos^2\left(\frac{kdx}{2\sqrt{L^2 + x^2}}\right) \operatorname{sinc}^2\left(\frac{kax}{\sqrt{L^2 + x^2}}\right) \quad (4.5)$$

Where the  $\operatorname{sinc}$  function is defined as  $\frac{\sin(x)}{x}$ , for  $x \neq 0$ ,  $k$  is the wavevector,  $k = \frac{2\pi}{\lambda}$ , and  $x$  is the horizontal position on the detector screen.

The simulation was carried out for a wavelength,  $\lambda$ , of 488 nm, a slit width of  $10\lambda$ , slit separation of  $80\lambda$ , and the detector screen positioned  $10000\lambda$  away from the slits. Using the Huygens-Fresnel principle, each slit is a source of Huygens wavelets. The detector screen has dimensions,  $1 \text{ mm}^2$  and there are  $2051^2$  bins, giving a bin an effective size:  $\sim 488 \text{ nm}$  or  $\sim \lambda$ . The initial position of the photon packets is sampled uniformly from the slit area, after randomly choosing one of the slits to emit from. A random direction is then chosen to ensure that the packets will hit the detector screen. The simulation was run with  $10^9$  packets, which took  $\approx 10 \text{ mins}$  to run on an 8 core Intel Xeon machine. This gave an accurate match to the theoretical expression, as seen in Fig. 4.3.

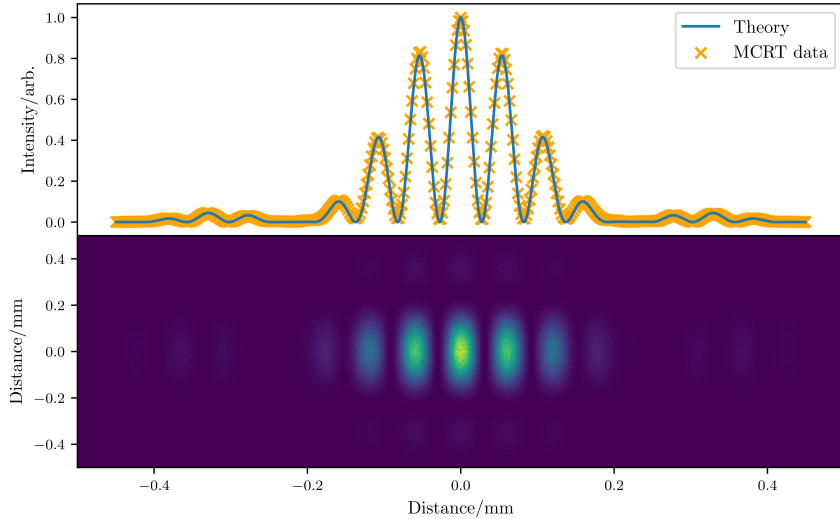


**Figure 4.3:** Comparison of theory and simulation for the double slit experiment. Top image shows a slice through the computed image and the expected profile from theory. For clarity only every 5<sup>th</sup> MCRT data point is plotted. Bottom image shows the computed image.

---

<sup>†</sup>Though this example is not strictly MCRT, but rather ray tracing, as it involves no scattering. The full MCRT method will be used in later sections.

### Diffraction by a Square Slit

$\varphi MC$  is also validated by simulating diffraction from a square aperture in the far and near field. Fresnel diffraction occurs in the near field when the *Fresnel number*, Eq. (4.6), is greater than 1.0. Fraunhofer diffraction occurs when the *Fresnel number* is less than 1.0.

$$F = l \sqrt{\frac{2}{\lambda r_0}} \quad (4.6)$$

Equation (4.6) is the Fresnel number, where  $l$  is the slit width,  $\lambda$  is the wavelength of the incident radiation, and  $r_0$  is the distance from the aperture to the detector screen, as shown in Fig. 4.4.

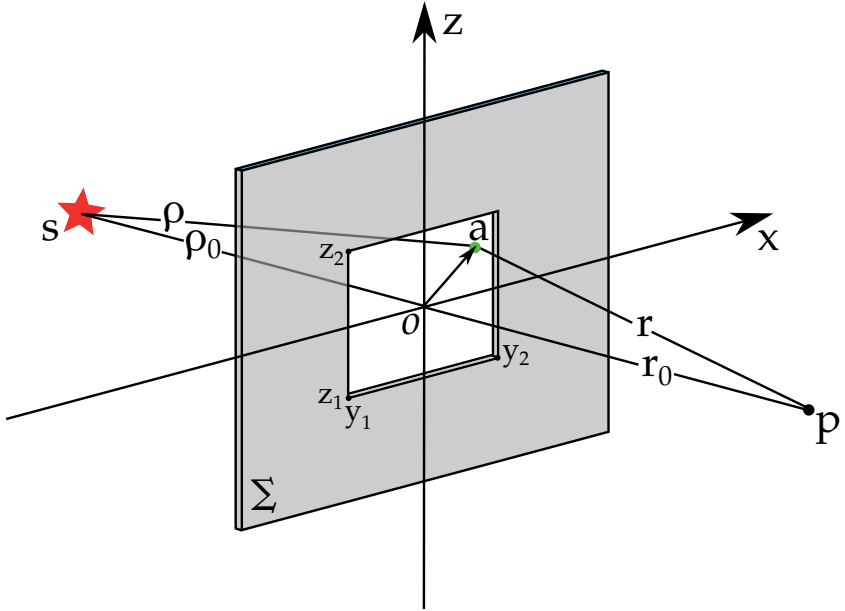


Figure 4.4: Geometry of the square aperture used in the validation.

To compare  $\varphi MC$  to the theory, the theory must first be discussed. Consider the setup as shown in Fig. 4.4, to calculate the intensity at a point  $P$  the contribution by an area element  $dS$  at the point  $a$ , to the optical disturbance at a point  $P$  is considered. Accounting for the unobstructed optical disturbance from  $S$  as well and using Eq. (4.4), yields:

$$U(P) = \frac{1}{i\lambda} \iint_{\Sigma} \frac{A e^{i(k\rho - \omega t)}}{\rho} \frac{e^{ikr}}{r} \cos(\theta) dS \quad (4.7)$$

In the case where  $\rho_0$  and  $r_0$  are large compared to the size of the aperture, then  $\cos(\theta) = 1$  and  $\frac{1}{\rho r} = \frac{1}{\rho_0 r_0}$ . The lengths of  $r_0$  and  $\rho_0$  are:

$$r = \sqrt{r_0^2 + y^2 + z^2} \quad (4.8)$$

$$\rho = \sqrt{\rho_0^2 + y^2 + z^2} \quad (4.9)$$

Using the binomial theorem to expand Eqs. (4.8) and (4.9) yields:

$$\rho + r \approx \rho_0 + r_0 + (y^2 + z^2) \frac{\rho_0 r_0}{2\rho_0 r_0} \quad (4.10)$$

Substituting Eq. (4.10) into Eq. (4.7) with  $k = 2\pi/\lambda$

$$U(P) = \frac{Ae^{-i[k(\rho_0+r_0)\omega t]}}{i\lambda\rho_0 r_0} \iint_{\Sigma} e^{i2\pi y^2 \frac{(\rho_0+r_0)}{2\lambda\rho_0 r_0} + i2\pi z^2 e^{\frac{i\pi u^2}{2}} \frac{(\rho_0+r_0)}{2\lambda\rho_0 r_0}} dS \quad (4.11)$$

Introducing the dimensionless variables  $u$  and  $v$

$$u = y \sqrt{\frac{2(\rho_0 + r_0)}{\lambda\rho_0 r_0}} \quad (4.12)$$

$$v = z \sqrt{\frac{2(\rho_0 + r_0)}{\lambda\rho_0 r_0}} \quad (4.13)$$

and substituting them into Eq. (4.11).

$$U(P) = \frac{\tilde{E}_u}{2} \int_{u_1}^{u_2} e^{\frac{i\pi u^2}{2}} du \int_{v_1}^{v_2} e^{\frac{i\pi v^2}{2}} dv \quad (4.14)$$

Equation (4.14) describes the optical disturbance at the point  $P$ , with  $\tilde{E}_u$  the unobstructed disturbance at  $P$ . Equation (4.14) can be evaluated using the Fresnel integrals,  $C(w)$  and  $S(w)$ :

$$\int_0^w e^{i\pi w'^2/2} dw' = C(w) + iS(w) \quad (4.15)$$

$$S(w) = \int_0^w \sin\left(\frac{\pi w'^2}{2}\right) dw' \quad (4.16)$$

$$C(w) = \int_0^w \cos\left(\frac{\pi w'^2}{2}\right) dw' \quad (4.17)$$

Using Eq. (4.15), where  $C(w)$  and  $S(w)$  are the Fresnel integrals as in Eqs. (4.16) and (4.17). Equation (4.14) can then be transformed into an intensity, by taking the absolute value and squaring, yielding Eq. (4.18):

$$I_p = \frac{I_u}{4} \{ [C(u_2) - C(u_1)]^2 + [S(u_2) - S(u_1)]^2 \} \times \{ [C(v_2) - C(v_1)]^2 + [S(v_2) - S(v_1)]^2 \} \quad (4.18)$$

Equation (4.18) gives the intensity of the field at the point  $P$  on axis for a square aperture where  $I_u$  is the unobstructed intensity at the point  $P$ .

As the mathematics of calculating the optical disturbances at all points on a plane at point  $P$  is difficult, instead the aperture is moved by small displacements, with  $\overrightarrow{SOP}$  fixed. This effectively achieves the translation of the origin,  $O$ , with respect to the fixed aperture. Thus, for each displacement new aperture coordinates  $y_1$ ,  $y_2$ ,  $z_1$ , and  $z_2$  are generated and therefore new  $u_1$ ,  $u_2$ ,  $v_1$ , and  $v_2$ . Therefore, the intensity at a point  $P + \delta d$ , where  $\delta d$  is the displacement,

can be calculated. This approximation holds for displacements that are small compared to the  $\rho_0$  [129, 133, 134]. Using this method and Eq. (4.18) gives the theoretical curves in Fig. 4.5.

In  $\varphi MC$ , the above experiment is simulated. A square slit is uniformly sampled in the  $x$ , and  $z$  direction to get the packets initial position. A random direction is then sampled, by uniformly picking a point on the detector screen. This ensures the algorithm does not waste time by calculating packets trajectories that are not registered by the detector. We assume a plane wave is incident on the aperture and each photon is given the same initial complex electric field.

The distance between the detector screen and the aperture is varied and the intensity on the screen is measured for  $\sim 10^{10}$  photons released from the aperture as Huygens wavelets. For *Fresnel numbers* greater than 1.0, the number of bins is 300, covering a distance of  $600 \mu m$ . For the case of Fraunhofer diffraction, the number of bins is 100 covering a distance of  $6000 \mu m$ . The simulations take  $\sim 3$  minutes for  $10^{10}$  packets to be run on an Intel Xeon E3-1245 v5, 8 cores @ 3.5GHz machine. The number of bins, and photons packets simulated had to be increased for the cases where the Fresnel number was large (i.e the detector screen was near the aperture). This is due to the diffraction pattern becoming “noisy” and thus needs a higher resolution to accurately simulate. Fig. 4.5 shows the comparison between the theory and the  $\varphi MC$  simulations.

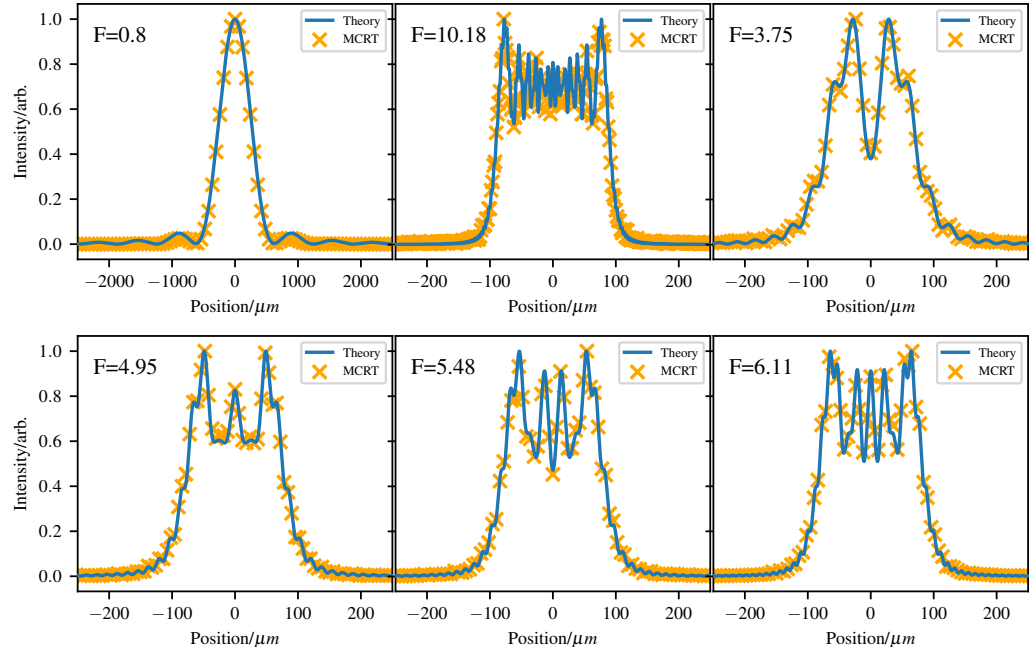


**Figure 4.5:** Comparison of theory and simulation for diffraction through a square aperture in the Fresnel and Fraunhofer regimes.

### 4.3 Gaussian Beams

Now that the method of tracking the complex phase of packets and using the Huygens-Fresnel principle has been verified against theoretical results, we can now turn our attention to modelling the propagation of beams that require the wave behaviour of light to either form or propagate. The first beam type we will examine is the Gaussian beam. Gaussian beams are important as most laser beams have the profile of the fundamental ( $\text{TEM}_{00}$ ) Gaussian mode. This section will show that  $\varphi MC$  can accurately model all the physical phenomena of Gaussian beams, within the MCRT regime.

Before discussing how  $\varphi MC$  can model a Gaussian beam, the theory and various physical parameters of the beam must be described. The electric field of a Gaussian beam can be defined as in Eq. (4.19) [135]:

$$E(r, z) = E_0 \frac{w_0}{w(z)} e^{\frac{-r^2}{w(z)^2}} e^{-i(kz + k \frac{r^2}{2R(z)} - \varphi(z))} \quad (4.19)$$

Where:

$r$  is the radial distance from the optical axis [m];

$z$  is the axial distance from the beams waist [m];

$k$  is the wavenumber,  $k = \frac{2\pi}{\lambda}$  [ $m^{-1}$ ];

$E_0$  is the electric field amplitude at the origin [ $V m^{-1}$ ];

$w(z)$  is the radius of the beam at which the amplitude has fallen to  $\frac{1}{e}$ , at the distance  $z$  along the beam, Eq. (4.20) [m];

$w_0$  is the waist radius [m];

$R(z)$  is the radius of curvature of the beams wavefronts at  $z$ , Eq. (4.21) [m];

and finally,  $\varphi(z)$  is the Gouy phase at  $z$ , Eq. (4.22) [-].

Equations (4.20) to (4.24) give the definitions of key physical properties as outlined above or as shown in Fig. 4.6.  $z_r$  is the Rayleigh range, Eq. (4.23), and defines the point at which the beams waist grows to  $\sqrt{2}$  times the size of the beam at its waist. The waist of the beam at the focal point is defined as Eq. (4.24), where  $f$  is the focal length and  $D$  is the  $\frac{1}{e^2}$  diameter of the beam at the lens.

$$w(z) = w_0 \sqrt{1 + \left(\frac{z}{z_r}\right)^2} \quad (4.20)$$

$$R(z) = z \left[ 1 + \left( \frac{z_r}{z} \right)^2 \right] \quad (4.21)$$

$$\varphi(z) = \arctan \left( \frac{z}{z_r} \right) \quad (4.22)$$

$$z_r = \frac{\pi w_0^2}{\lambda} \quad (4.23)$$

$$w_0 = \frac{2\lambda f}{\pi D} \quad (4.24)$$

$$(4.25)$$

With the physical properties of the Gaussian beam outlined, a Gaussian beam can now be modelled using our algorithm. To simulate a Gaussian beam, we set up the simulation as shown in Fig. 4.7. The simulated lens used is a convex-plano lens, with radius of curvature, 4.6 mm, thickness,  $L_t$ , of 2.2 mm, and working distance,  $W_d$ , 8.5 mm. A Gaussian beam wavelength

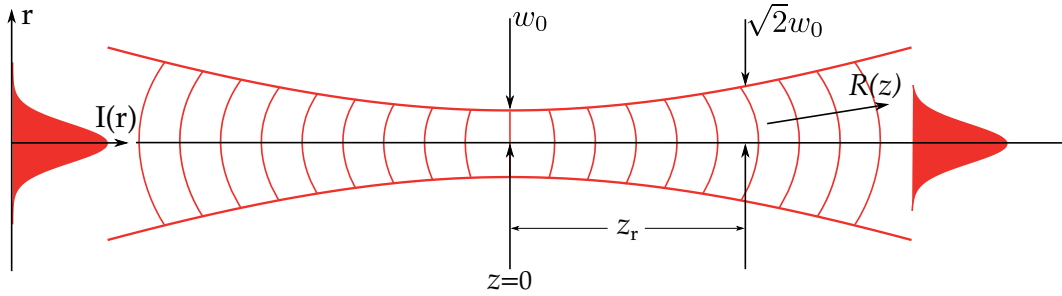


**Figure 4.6:** Illustration of a Gaussian beam focusing to its waist then diverging away. Image shows the various defined properties of a Gaussian beam along side the radius of curvature changing direction at the waist.

488 nm and  $\frac{1}{e^2}$  waist diameter 0.5 mm, is incident on the lens. Using Eq. (4.24) yields the size of the focal spot as 3.1  $\mu\text{m}$ .

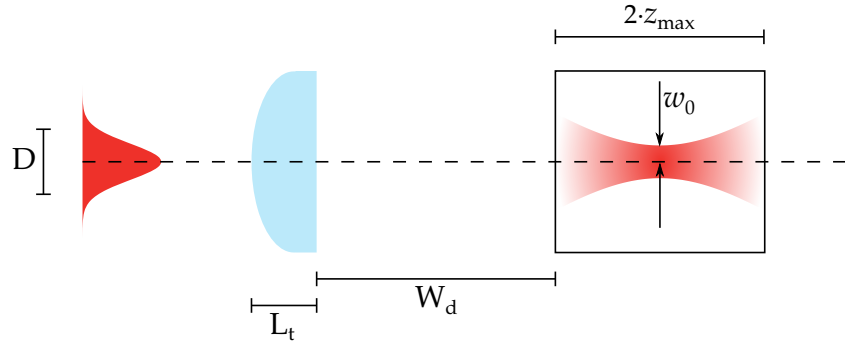


**Figure 4.7:** Simulation setup of focusing a Gaussian beam through a lens. Lens is convex-plano and is modelled on ThorLabs LA4249 UV fused silica lens [136].  $L_t$  is the lens thickness,  $D$  is the  $\frac{1}{e^2}$  input beam diameter,  $W_d$  is the working distance or back focal length,  $2 \cdot z_{\max}$  is the depth of the medium, and  $w_0$  is the beam waist.

To model the lens in  $\varphi MC$  the photons initial  $z$  position is set just in front of the lens. The  $x$  and  $y$  are randomly sampled from a Gaussian distribution with a waist of  $\sqrt{2}w_0$ . The factor of  $\sqrt{2}$  accounts for the conversion from intensity to electric field beam waist. This is because the electric field is  $\propto \exp\left(\frac{-r^2}{4\sigma'^2}\right)$ , and the intensity is  $\propto \exp\left(\frac{-r^2}{2\sigma^2}\right)$ . Thus, for the input electric field waist to be equal to the intensity,  $\sigma' = \sqrt{2}\sigma$ . The packet is given an electric field of the form Eq. (4.1), with  $P = 1 \text{ mW}$ , and  $A = \frac{1}{2}\pi w_0^2$ .

The packet is then propagated to the surface of the convex side of the lens. This is achieved by finding the intersection of a sphere, which represents the convex side of the lens, and the packets path. With the packet on the surface of the lens, Fresnel coefficients are calculated to determine if the packet is reflected or refracted. If the packet is reflected the packet is killed and the process starts again. If the packet is refracted, and moved in the new direction to the planar surface of the lens. The new direction vector is calculated using a vector version of Snell's law (see ?? for discussion of this). The packets are then uniformly sampled onto the surface of the voxel medium and the usual MCRT method is used to propagate the packet whilst tracking the phase.

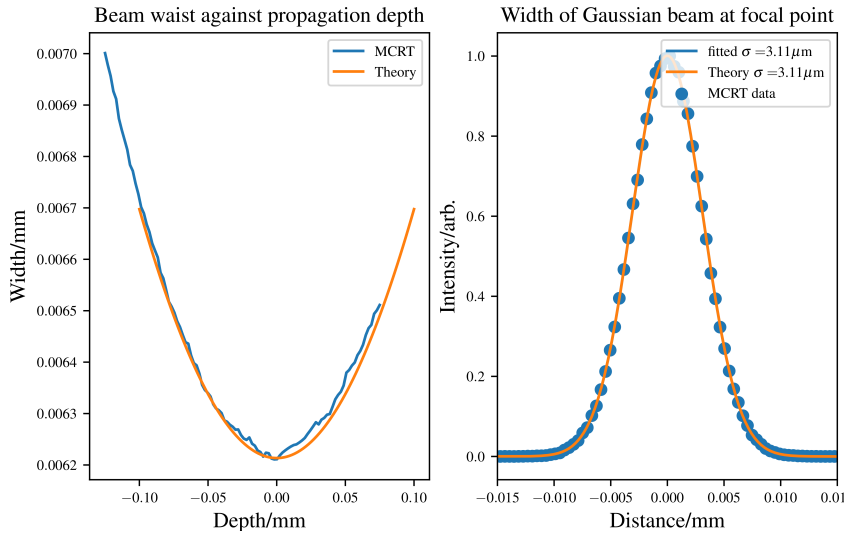


**Figure 4.8:** Results of *in-silico* experiment of focusing a Gaussian beam though a convex-plano lens.

Figure 4.8 shows the comparison of theory and *in-silico* experiment, with excellent agreement between the two.

$\varphi_{MC}$  also correctly models the change of direction of the radius of curvature,  $R(z)$ , as is predicted by theory. This process is described by Eq. (4.21), before the waist the curvature is negative, at the waist it is infinite, and past the waist its is positive. This can be seen in Fig. 4.9, where the beam (direction of propagation right to left) undergoes this:

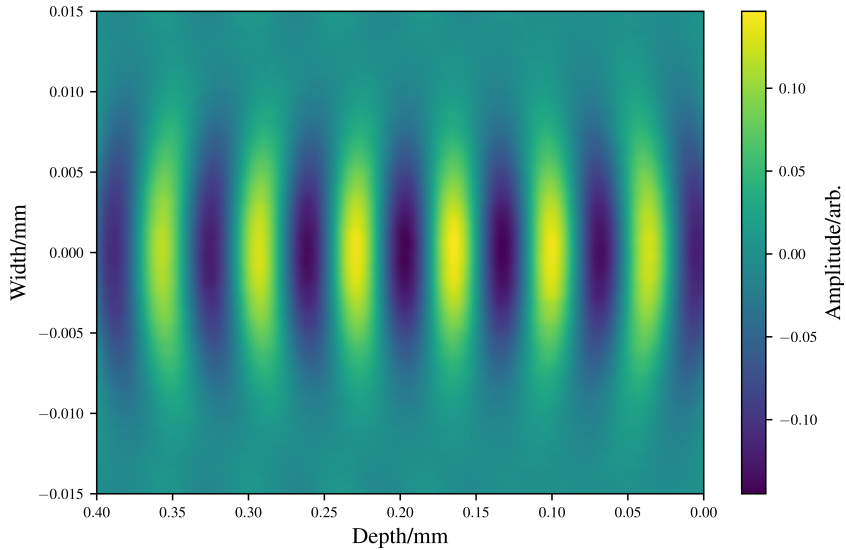


**Figure 4.9:** Slice through the real part of the complex electric field of the *in-silico* experiment as in Fig. 4.7. Figure shows the radius of curvature changing direction at the waist as predicted by theory.

$\varphi MC$  can also model spherical aberrations caused by lenses. Figure 4.10 shows aberrations caused by a plano-convex lens along side an illustration of the paths that light take through the imperfect lens, causing spherical aberrations.

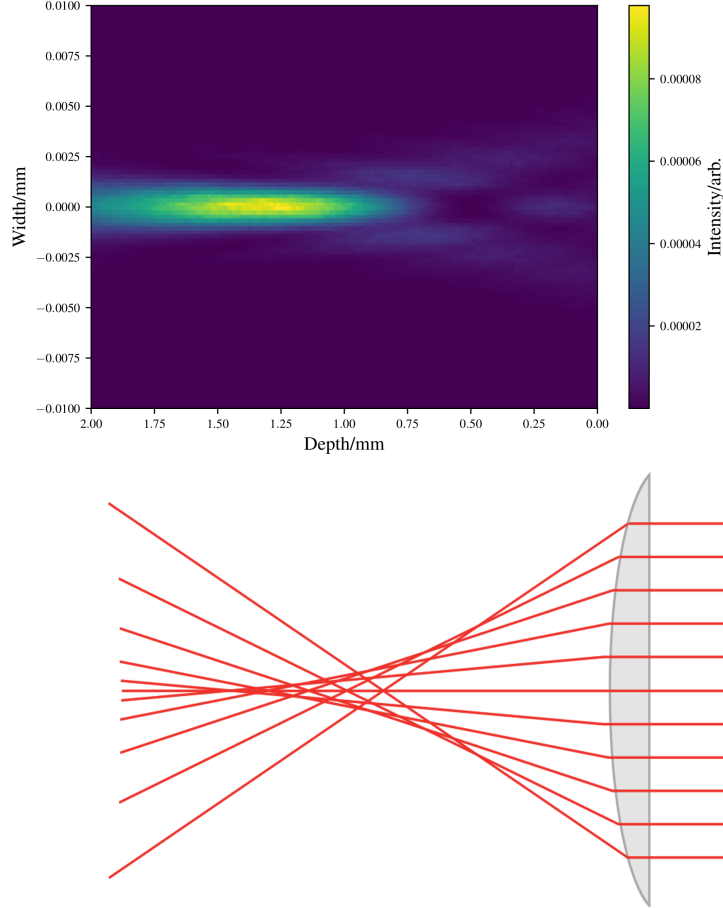


**Figure 4.10:** Illustration of  $\varphi MC$ 's ability to model spherical aberrations. Top image generated using same setup as in Fig. 4.7, but with  $D = 1.5$  mm within  $\varphi MC$ . Image shows the elongated focus and characteristic interference pattern behind the focus. Bottom image shows illustration of rays traced through a lens which suffers from spherical aberration.

This section has shown that Gaussian beams, and their physical phenomena can be accurately modelled using  $\varphi MC$ . A convex-plano lens was used to focus a Gaussian beam, but it is simple to implement other lenses given a triangulated mesh of the lens or an equation that describes the shape of the lens, e.g an aspheric lens.

## 4.4 Bessel Beams

Bessel beams have been the subject of intense research since their discovery in 1987 [137, 138]. Durnin noticed that the solution to the Helmholtz equation of the Bessel type were independent of the direction of propagation. This means that the central core of the beam is generally

more diffraction resistant when compared to a Gaussian beam with a similar spot size. Bessel beams also have a property of “self-healing”, this means if an obstruction is placed in the path of the central lobe of the Bessel beam, the Bessel beam can then “heal” and reform past the obstruction [139]. However, it is physically impossible to create a “real” Bessel beam as the Bessel beam can have infinite rings, which each carry the same amount of power, thus would require infinite amount of power [137]. Therefore, all Bessel beams that are created experimentally are quasi-Bessel beams which are similar to their theoretical counterpart over a finite distance [137].

These two properties make Bessel beams an attractive avenue of research, as novel solutions to imaging problems. There is also some debate among physicists as to whether these phenomena are justly labelled, or if they glib terms used to make Bessel beams seem better than they are [140–144].

#### 4.4.1 Theory

As before with the Gaussian beam, the theory behind the Bessel beam must be discussed before we can model the beam in  $\varphi MC$ . The electric field can be described using Eq. (4.26) [145]:

$$E(r, z) = E_0 \sqrt{\frac{2\pi k z w_0 \sin(\beta)}{z_{max}}} \exp\left(-\frac{z^2}{z_{max}^2} - \frac{i\pi}{4}\right) J_0(kr \sin(\beta)) \exp(ikz \cos(\beta)) \quad (4.26)$$

Where:

- $k$  is the wavevector,  $k = \frac{2\pi}{\lambda}$  [m];
- $z$  is the propagated distance [m];
- $\beta$  is the angle the wavefront propagates at (see Fig. 4.11) [rad];
- $w_0$  is the  $\frac{1}{e^2}$  width of the input Gaussian beam [m];
- $J_0$  is the Bessel function of the first kind, zeroth order;
- $r$  is radial distance from the optical axis [m].

Equation (4.26) gives the electric field for a Bessel beam. The intensity can be calculated using:

$$I(r, z) = \frac{c\epsilon_0 |E|^2}{2} \quad (4.27)$$

Using the definition total power transmitted by a beam as:

$$P = \frac{\pi I_0 w_0^2}{2} \quad (4.28)$$

Where  $I_0$  is defined as on axis intensity of the incident Gaussian beam.

$$I_0 = \frac{c\epsilon_0 E_0^2}{2} \quad (4.29)$$

Substituting Eqs. (4.26), (4.28) and (4.29) into Eq. (4.27) yields:

$$I(r, z) = \frac{4k_r P}{w_0} \frac{z}{z_{max}} J_0^2(k_r r) \exp\left(-\frac{2z^2}{z_{max}^2}\right) \quad (4.30)$$

Where:

- $k_r$  is the radial wavevector,  $k_r = k \sin(\beta)$ ;
- $P$  is the power of the incident Gaussian beam.

A Bessel beam can be formed by an axicon lens (see Fig. 4.11) or by diffraction through a ring, or through the use of a spatial light modulator. All the simulations of Bessel beams in this thesis use the axicon method of generating a Bessel beam, thus only axicons will be discussed. Figure 4.11 shows the geometry of a Bessel beam formed by an axicon. Using simple geometry and Snell's law the following equations can be derived to describe various properties of a Bessel beam formed by an axicon [146].

The propagation depth of a Bessel beam is defined as the distance from the tip of the axicon to the end of the "Bessel region". However, in reality the Bessel beam will continue to propagate slightly past this depth. Equation (4.31) shows the propagation depth of a Bessel beam where  $\cot$  is the cotangent function ( $\cot x = \frac{1}{\tan x}$ ).

$$z_{max} = R(\cot(\beta) - \tan(\alpha)) \quad (4.31)$$

The propagation angle of the conical waves,  $\beta$  can be calculated using Snell's law and  $\alpha$  the angle of the axicon:

$$\beta = \arcsin(n \sin(\alpha)) - \alpha \quad (4.32)$$

The central core of a Bessel beam is defined as the distance to the first zero of the Bessel beam. Equation (4.33) shows the radius of the core, where 2.405 is derived from the position of the first zero of the Bessel function.

$$r_o = \frac{2.405}{k \sin(\beta)} \quad (4.33)$$

Finally, the spacing between Bessel beam rings is:

$$\Delta\rho = \frac{\lambda}{2 \sin(\beta)} \quad (4.34)$$

#### 4.4.2 Validation

To ensure that the method described in Section 4.2 works as intended for Bessel beams several tests are compared to theoretical expressions and experimental data.

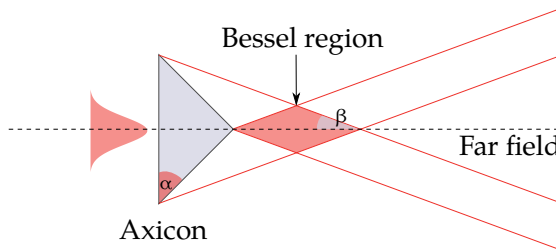


**Figure 4.11:** Geometry of a Bessel beam, generated by an axicon lens.  $\beta$  is the angle with the optical axis, and the angle of the conical waves.  $\alpha$  is the axicon angle.

#### Comparison to a theoretical Bessel beam

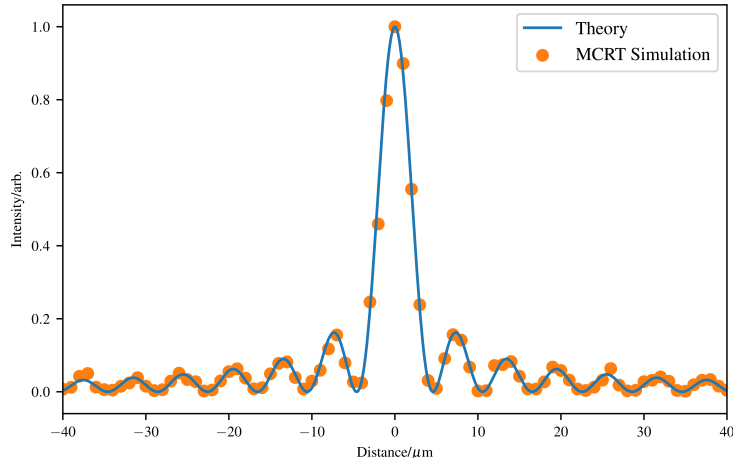
To compare with a theoretical Bessel beam, a Bessel beam is modelled in  $\varphi MC$ , and propagated through air into the "Bessel region" and then propagated into the far field to ensure the beam follows the theory in both these regions.

Figure 4.11 shows the set-up for the *in-silico* experiments. The Bessel beam is created with an axicon (conical) lens with an opening angle ( $\alpha$ ) of  $5^\circ$ , and a radius of  $12.7\text{ mm}$ . The input beam is Gaussian in profile with a  $\frac{1}{e^2}$  diameter of  $1\text{ mm}$ , and a wavelength of  $488\text{ nm}$ . The Bessel beam is then propagated to a detector screen  $10\text{ mm}$  away from the tip of the axicon, which is in the middle of the “Bessel region” for the first test. For the second test the Bessel beam is propagated past the “Bessel region” into the far field. The detector screen has a size of  $40\text{ }\mu\text{m} \times 40\text{ }\mu\text{m}$  with a bin resolution of  $1\text{ }\mu\text{m}$ .  $8 \times 10^{10}$  photon packets were simulated taking  $\sim 1$  hour on an 8 core Intel Xeon 3.5Ghz machine.

Equation (4.30) gives the profile of a theoretical Bessel beam at a depth  $z_{max}$ , this is plotted against the simulation setting the various constants to (see Eq. (4.35)), with the simulation similarly normalised to the maximum intensity of the image generated. Figure 4.12 shows this comparison.

$$\frac{4k_r P_z}{w_0 z_{max}} e^{-2\left(\frac{z}{z_{max}}\right)^2} = 1 \quad (4.35)$$

Figure 4.13 shows the profile of the Bessel beam in the far field, where the theory predicts it becomes a ring.  $\varphi$ MC can also model the self-healing property of Bessel beams, this is shown in Fig. 4.14.



**Figure 4.12:** Comparison of theoretical and MCRT simulation of a Bessel beam, with intensity normalised. The results from  $\varphi$ MC show good agreement with the theory.

### Comparison to experimental data

To ensure our algorithm works in turbid media, experiments were carried out by our collaborators, S. Reidt *et al.*, at the University of Dundee. These experiments allow us to test our algorithms ability to simulate scattering of Bessel beams in turbid media. S. Reidt *et al.* carried out an experiment where a Bessel beam was propagated through a medium of varying turbidity. A laser, wavelength  $488\text{ nm}$ , with a Gaussian profile is shone on an axicon lens, with angle  $5^\circ$ . The laser beam had a  $\frac{1}{e^2}$  diameter of  $2\text{ mm}$ .

The Bessel beam was allowed to propagate through the air for  $10\text{ cm}$  before entering a cuvette of side  $2\text{ mm}$ . The cuvette was filled with  $500\text{ }\mu\text{L}$  of water, and various volumes of a scattering agent added. Figure 4.15 shows the experimental set-up.

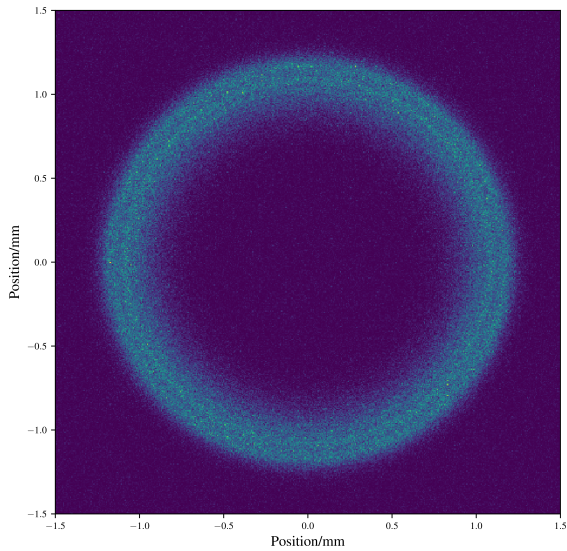


**Figure 4.13:** Bessel beam in the far field. Bessel beams in the far field becomes a ring beam. Image shows a slice of intensity through the medium.

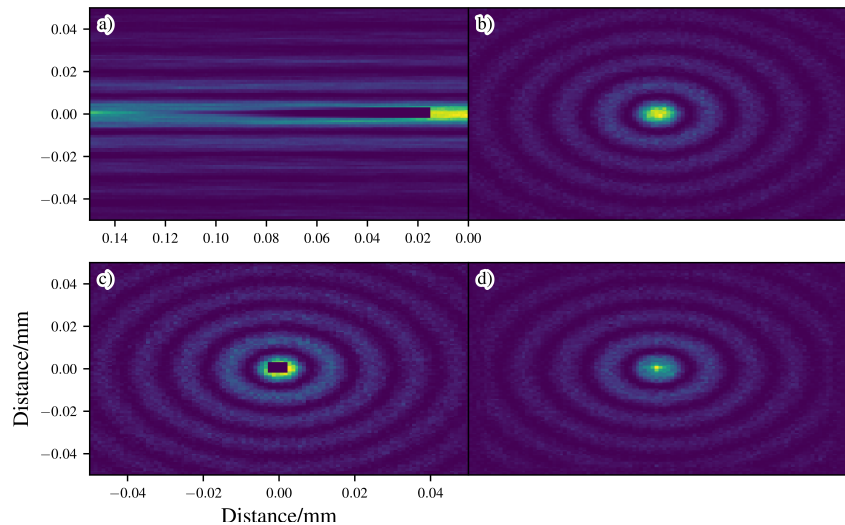


**Figure 4.14:** Illustration of the Bessel beams self-healing property. Highly absorbing cube placed near the top of the medium. Figure shows that the Bessel beam forms further down the optical axis. a) shows side on view with the obstacle at 0.02 mm, b) shows top down view at surface of the simulated medium before the obstacle, c) shows top down view in the middle of the obstacle, and d) shows the top down view after the Bessel beam has “healed”.

The scattering agent used is intralipid 20 % (Sigma-Aldrich), which is diluted as shown in Table 4.1. Figure 4.16 shows the optical properties of Intralipid 20 %. Dilutions of Intralipid are kept below 2% scattering particle concentration, so that the scattering exhibited by the

intralipid is in the independent scattering regime<sup>‡</sup>. This allows the linear scaling of the optical properties by concentrations [147, 149, 150]. Images of the Bessel beam as it emerges from the cuvette are taken for comparison with our algorithm.

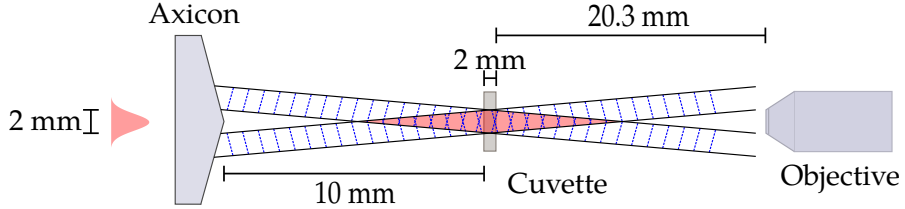


**Figure 4.15:** Experimental set-up for propagating a Bessel beam through a cuvette filled with varying concentrations of Intralipid 20%. Bessel beam is imaged by an 20× objective lens and a Grasshopper 3 camera.

Intralipid	$\mu L$	Intralipid concentration		Optical properties Scattering coefficient/ $m^{-1}$
		$H_2O$	Volume/%	
0	500	0.00	0.00	0.00
2	500	0.39841	0.0908	557.14
4	500	0.79365	0.1816	1114.28
6	500	1.18577	0.2724	1671.42
8	500	1.57480	0.3632	2228.56
10	500	1.96078	0.4534	2785.71
12	500	2.34375	0.5448	3342.84

**Table 4.1:** Intralipid solutions used for experiment, see also Fig. 4.16.

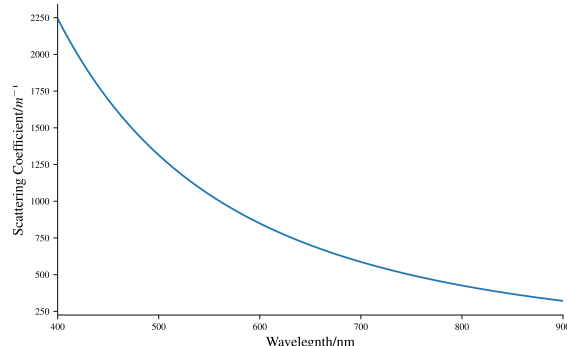


**Figure 4.16:** Scattering properties of 20% Intralipid [151].

To model within  $\varphi MC$ , we simplify the experimental setup considerably. The simulation models the propagation of photon packets through the axicon to its conical surface. On the conical surface the Huygens-Fresnel principle is invoked, and the packet is sampled onto the surface of the medium (cuvette). The sampling of the photon onto the surface of the medium,

<sup>‡</sup>The independent scattering regime is where  $g$  is dependent on the size, shape and material properties of the scattering particle, and the material properties of the bulk material, but not the number of scattering particles [147, 148].

speeds the algorithm up, as it does not need to simulate the photons that would “miss” the medium. From there the usual MCRT method propagates the packet through the medium while tracking its phase, and scattering the packet until it leaves the medium. If the packet leaves the medium to any side other than the far side of the cuvette (e.g any side of the cuvette not facing the objective lens), then it is discarded. If the packet leaves the medium on the objective lens facing side, then the packet is recorded by its phase onto an area element. For each intralipid concentration  $6.4 \times 10^{10}$  photons are run over 64 cores, taking  $\sim 3$  hours for the  $12\mu L$  intralipid volume. Once all the packets have been run, the phase is converted into intensity, as in Eq. (4.3), but in 2D.

Figures 4.17 and 4.18 show the results from the experiment and simulation. The simulation shows good agreement with experimental data within experimental and simulation uncertainty.

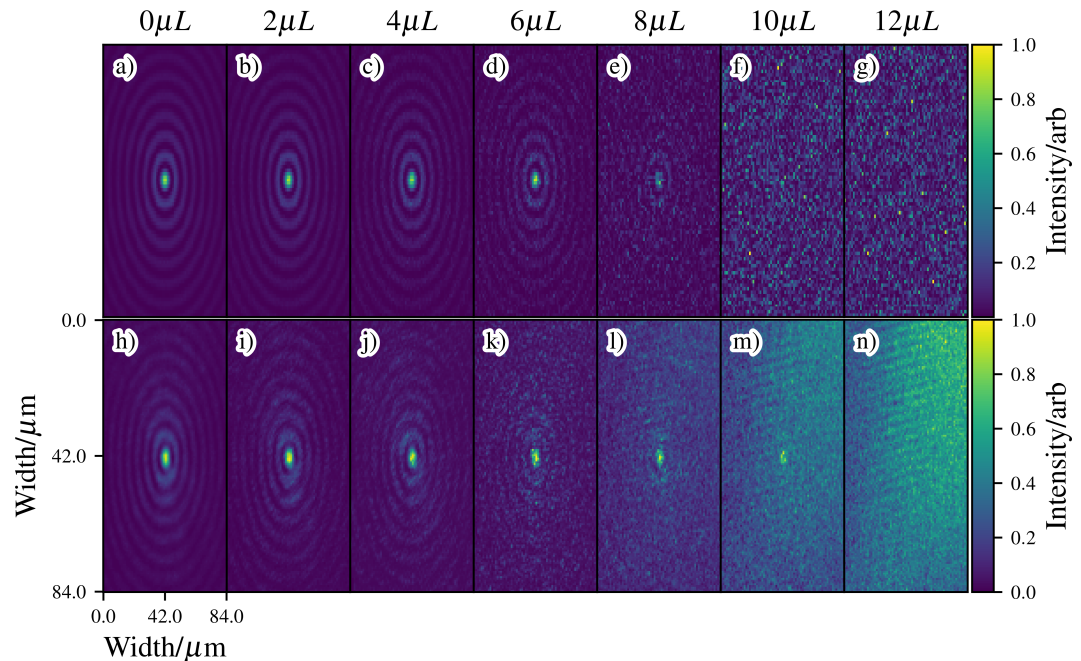


**Figure 4.17:** Comparison of experimental and simulation data for propagation of a Bessel beam produced by an axicon, through mediums of various turbidity. Images a) to g) is the data from  $\varphi$ MC, and h) to n) are the experimental data. Volumes along the top are the volume of Intralipid in each solution as in Table 4.1. All images are cropped so they are the same size and normalised to the maximum value in each image.

## Discussion

As mentioned in previous sections, the power of the MCRT method is that we can track virtually any quantity in the simulation. Alongside generating intensity images, we can also track the average number of scatterings per packet, a quantity that is hard to measure experimentally. Table 4.2 shows the average number of scatterings per packet alongside the optical depth of the medium from the source to the image plane. The simulations show that above  $\approx 2$  scatterings of a packet the Bessel beam is “destroyed” and the generated image becomes washed out with noise.

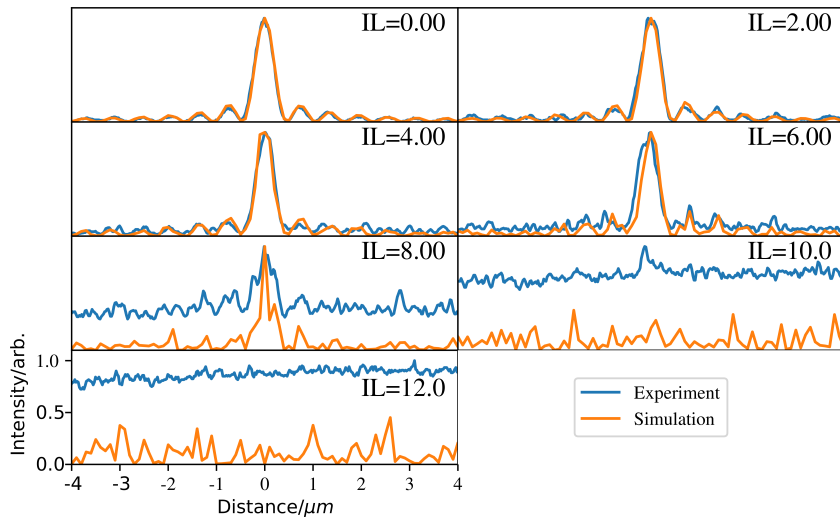


**Figure 4.18:** Line graph plots of slices taken through the generated and experimental images as shown in Fig. 4.17.

Volume IL/ $\mu L$	Avg # scatterings	Optical depth
2	0.734	1.114
4	1.225	2.229
6	1.594	3.342
8	1.899	4.457
10	2.168	5.571
12	2.417	6.686

**Table 4.2:** Average number of scattering per packet and the optical depths for different volumes of Intralipid.

Originally the medium was modelled as in the experiment, a  $2 \text{ mm}^3$  volume. The image created was thus a  $2001 \times 2001$  with a resolution of  $1 \mu\text{m}$ . To achieve a good signal to noise ratio for this set-up  $6.4 \times 10^{12}$  packets needed to be run, taking  $\sim 70$  hours on a computer cluster using 64 cores. This was sufficient to get a good signal to noise ratios for all the simulations up to  $6 \mu\text{L}$ . However, the number of packets needed to get a good signal to noise ratio for  $8 \mu\text{L}$  and above was prohibitively computationally costly. Therefore, the modelled medium was shrunk in the  $x$  and  $y$  directions giving:  $0.5 \text{ mm} \times 0.5 \text{ mm} \times 2.0 \text{ mm}$ . This allowed a smaller image ( $501 \times 501$ ), whilst keeping the same resolution. Shrinking the medium also has the benefit that the photons are confined closer to the image plane, thus ensuring more photons hit the plane in comparison to the larger medium.

Shrinking the medium's size does have some drawbacks. First, the Bessel beams propagation depth rely on the input beams width (see Eq. (4.31)). The input beams width was kept constant between the shrinking of the volumes size. However, shrinking the medium's size in the  $x$  and  $y$  directions gives the same effect as using a smaller input beam. Therefore, the  $x$  and  $y$  dimension were carefully chosen such that the Bessel beam would still form a Bessel beam at the image plane. The second issue with shrinking the medium is that some packets may be lost. This means that in the larger medium a packet may scatter toward an  $x$  or  $y$  medium wall and then scatter back into the centre of the medium and then is recorded. However, this same packet in

the smaller medium would be lost as the packet would exit the medium and cease to be tracked. It is not expected that this will cause much of an issue as any scattering event already degraded the quality of the beam, as that packet is no longer coherent with the rest of the packets, thus it will not contribute positively to the Bessel beam. To ensure this is not an issue, results from a larger medium are compared to that of the smaller medium in Fig. 4.19. The larger and smaller medium yield the same results (within Monte Carlo noise) for Intralipid volumes less than  $8 \mu\text{L}$ . At  $8 \mu\text{L}$  the smaller medium has a Bessel beams central core, whilst the larger medium is noisy, and forms no Bessel beam. This test has shown that shrinking the medium allows accurate modelling of the propagation of a Bessel beam through a turbid medium while using less computational resources.

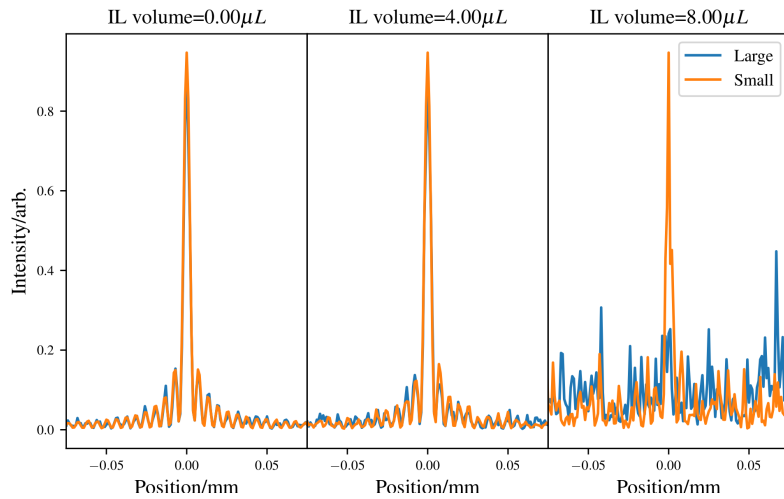


**Figure 4.19:** Comparison of a larger medium,  $2 \text{ mm}^3$  versus that of a smaller medium,  $0.5 \text{ mm} \times 0.5 \text{ mm} \times 2.00 \text{ mm}$ . The figure shows that the smaller medium gives a better signal to noise ratio, whilst still accurately modelling the experiment.

## 4.5 Higher Order Bessel Beams

Higher order Bessel beams (HOBBs), are Bessel beams where the electric field has an extra term of  $e^{-il\varphi}$ , as shown in Eq. (4.36), and  $l \neq 0$ . HOBBs have found use for optical trapping targets that are reflective/low refractive index, and optical manipulation [152,153]. Our technique outlined in the preceding sections, can also be applied to arbitrary higher order Bessel beams.

As before, the electric field of a  $l^{\text{th}}$  order Bessel beam is:

$$E(r, \varphi, z) = E_0 J_l(k_r r) e^{-ik_z z} e^{-il\varphi} \quad (4.36)$$

Where:

- 1 is the order of the beam [-];
- $k_z^2 + k_r^2 = k^2$ , where  $k^2$  is the wavevector [ $\text{m}^{-1}$ ];
- $r$ ,  $\varphi$ , and  $z$  are the cylindrical coordinates [ $\text{m}$ ,  $\text{rad}$ ,  $\text{m}$ ];
- and  $J_l$  is the l-order Bessel function of the first kind [-].

To generate higher order Bessel beam, a helicon is used. A helicon (shown in Fig. 4.20) is an axicon attached to a helix phase delay element. The helical element imparts a helical phase

delay to photon packets as they pass through the element.

The distance travelled though the helicon is shown in Eqs. (4.37), (4.38) and (4.40) [154].  $h_1$  is the path length travelled by a photon through the helical element.  $h_2$  is the path through an axicon, and  $\Delta h$  is the height of the helical discontinuity.

$$h_1 = \frac{l\phi\lambda}{(n-1)2\pi} \quad (4.37)$$

$$h_2 = r \tan(\alpha) \quad (4.38)$$

$$h_3 = h_1 + h_2 \quad (4.39)$$

$$\Delta h = \frac{l\lambda}{n-1} \quad (4.40)$$

Where  $\phi$  is the azimuthal angle,  $r$  is the radial position,  $l$  is an integer that describes the order of the Bessel beam, and  $\alpha$  is the axicon angle.

The path length in the above equations can be converted into a phase delay by considering the transmission functions of the individual elements [155–158]:

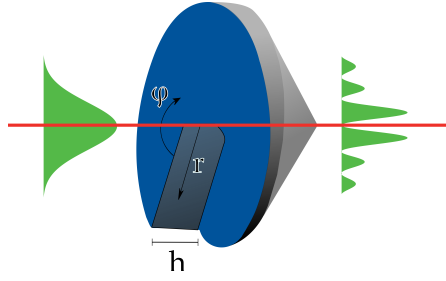


**Figure 4.20:** Helical delay element attached to an axicon. The Axicon introduces a radial delay in addition to that of the helical element. If the input beam is a Gaussian, the output beam is a higher order Bessel beam,  $l > 0$ .

$$T_1(\varphi) = e^{-ik(n-1)h_1} = e^{-il\phi} \quad (4.41)$$

$$T_2(r) = e^{-ik(n-1)h_2} = e^{-ik_r r} \quad (4.42)$$

$$T_3(r, \varphi) = T_1 * T_2 = e^{-ik_r r - il\phi} \quad (4.43)$$

Where  $T_1$  is the transmission function for the helical element,  $T_2$  is the transmission function for the axicon, and  $T_3$  is the total transmission function. Using the small angle approximation for  $\beta$  and Eq. (4.32), and knowing  $k_r = \sin(\beta)$  yields the phase delay as a function of angle and radial position:

$$\varphi(\phi, r) = k(n-1)r\alpha + l\phi \quad (4.44)$$

To implement a helicon in the  $\varphi MC$  algorithm, a helical phase delay is added. The additional delay is implemented by adding  $l\phi$  where  $0 < \phi < \frac{2\pi}{l}$ . An actual helix element is not modelled explicitly in the code, but rather just the phase delay. This method is similar to using a spatial light modulator in an experiment to impart a phase delay on a beam.

Figure 4.21 shows the comparison between theoretical higher order Bessel beam and the higher order beam simulated by  $\varphi MC$ .

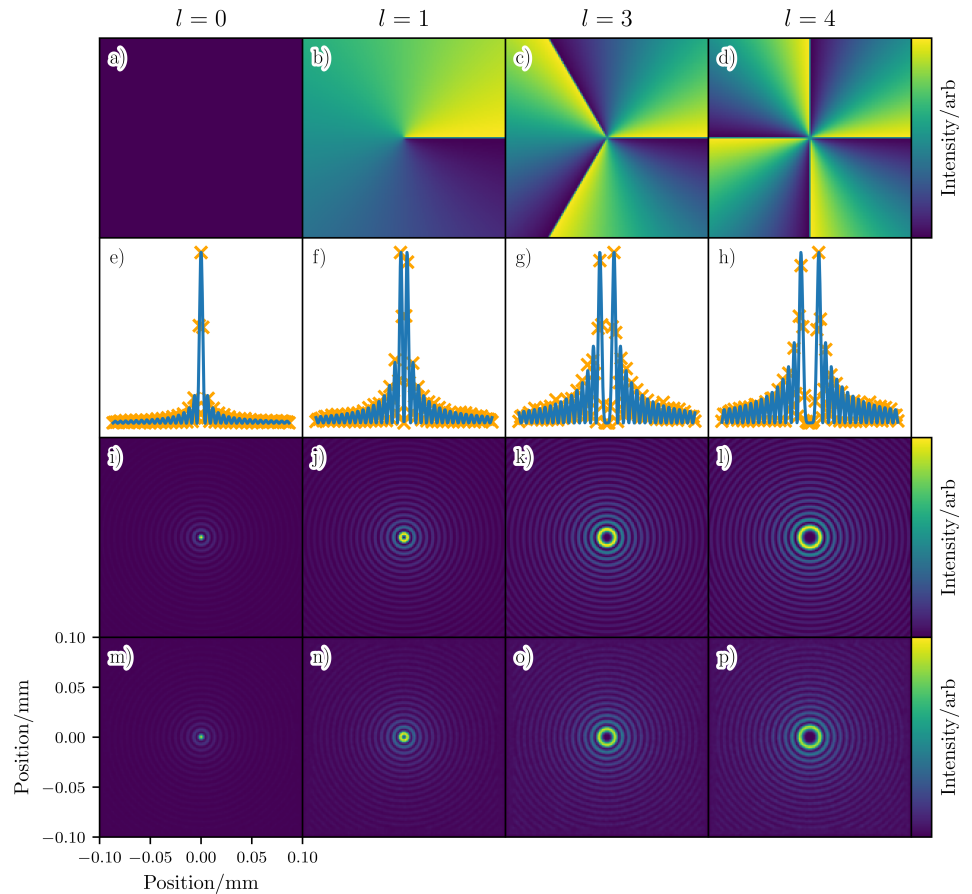


**Figure 4.21:** HOBBs. a) to d) show the phase shift due to the helical element. e) to h) show line plots of the simulation data compared to the theory. i) to l) and m) to p) show the higher order Bessel beam images for theory and simulation data respectively.

## 4.6 Comparison

As Bessel and Gaussian beams are radically different from one another it is hard to directly compare the two beams. Gaussian beams carry all their power in the “central core” of the beam, whereas in a Bessel beam, it carries the same amount of power in each ring. Bessel beams also have a much larger depth of focus than Gaussian beams. This section attempts to compare the two beams, to predict which beam performs better in a heavily scattering medium using  $\varphi$ MC. Bessel beams are expected to perform better than Gaussian beams, due to their self-healing properties and non-diffractive core, this section aims to quantify how this property may or may not help penetration through a highly scattering medium.

As mentioned, Bessel beams and Gaussian beams are not alike, so to ensure a fair comparison the Bessel beams central core width is set to that of the Gaussian beam’s waist.

$$r_0 = \frac{\kappa}{k \sin\beta} \quad (4.45)$$

Where  $\kappa$  is a constant that determines the metric used to measure the Bessel beam’s core, and the other symbols have the same meanings as before. For  $\kappa = 2.408$  the radius is measured from the maximum of the core to the first zero of the Bessel beam.  $\kappa = 1.75$  measures the Bessel beam’s core from the maximum to  $\frac{1}{e^2}$  of the maximum. For both beams central cores to be equal, the axicon used to generate the Bessel beam is adjusted. This is achieved by calculating the “correct”  $\alpha$  based upon the optical setup used to focus the Gaussian beam. Using the small angle approximation<sup>§</sup> and  $\kappa = 1.75$  we can compare the Bessel beam’s core radius to a Gaussian beam’s waist:

$$\frac{1.75\lambda}{2\pi\sin\beta} = \frac{2\lambda f}{\pi D} \quad (4.46)$$

$$\alpha = \frac{1}{n-1} \arcsin \left( \frac{1.75D}{4f} \right) \quad (4.47)$$

Where  $\alpha$  is the axicon angle as before,  $n$  is the refractive index of the axicon,  $D$  is the  $\frac{1}{e^2}$  diameter of the incident Gaussian beam on the lens, and  $f$  is the focal length of the lens used to focus the Gaussian beam. Both  $D$  and  $f$  are properties of the optical system used to focus the Gaussian beam. The lens used to focus the Gaussian beam is the same as used in the previous section to validate that  $\varphi$ MC can model a Gaussian beam, a convex-plano lens, with radius of curvature 4.6 mm, a working distance of 8.5 mm and thickness of 2.2 mm.

The first simulation comparisons carried out between the Bessel and Gaussian beams is to use the same power to generate both beams. The beams are then propagated through mediums of varying degrees of Intralipid solution. Volumes of 0.0, 26, 52, 78, and 104  $\mu L$  are used of Intralipid in 500  $\mu L$  of water. The medium has a volume of 0.1 mm  $\times$  0.1 mm  $\times$  0.2 mm, and voxel resolution of 1  $\mu m$ . For both beams a wavelength of 488 nm and a power of 1 mW is used. One hundred million packets are simulated for each simulation. The results of this are shown in Figs. 4.22 and 4.23

The results show that for the same power, Gaussian beams propagate deeper into the medium compared to Bessel beams. This is to be expected as in a Gaussian beam all the power is in its “central core”, whilst the power is evenly distributed between all the Bessel beam’s rings. Therefore, for a second comparison the power given to the Bessel beam is such that the central core maximum matches that of the Gaussian beam’s at its focus for the case where there is no

---

<sup>§</sup>for small  $\alpha$  and  $\beta$ :  $\beta = (n-1)\alpha$ .

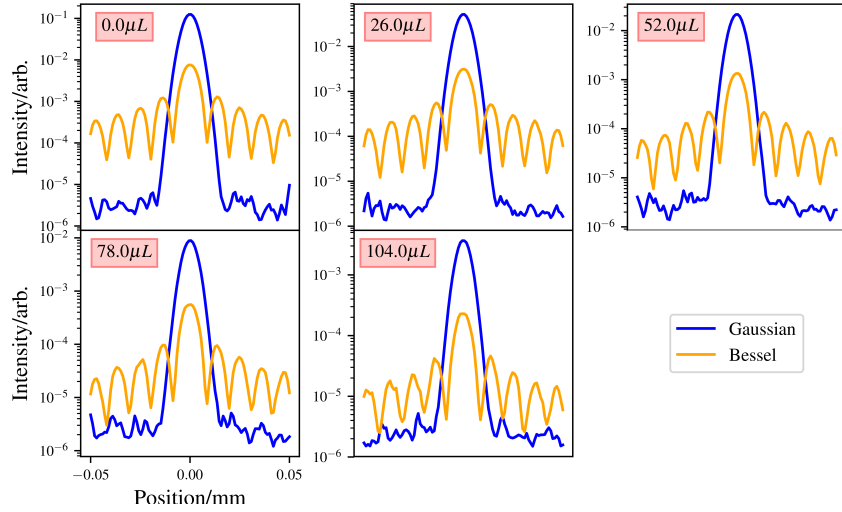


**Figure 4.22:** First comparison of Bessel and Gaussian beams with equal power used to generate both beams. Plots taken at the Gaussian beams focus. The maxima at the sides of the Gaussian beam in the  $0.0\mu\text{L}$  plot are due to simulation effects, mainly the small size of the medium not allowing photons from further off the optical axis to interfere destructively.

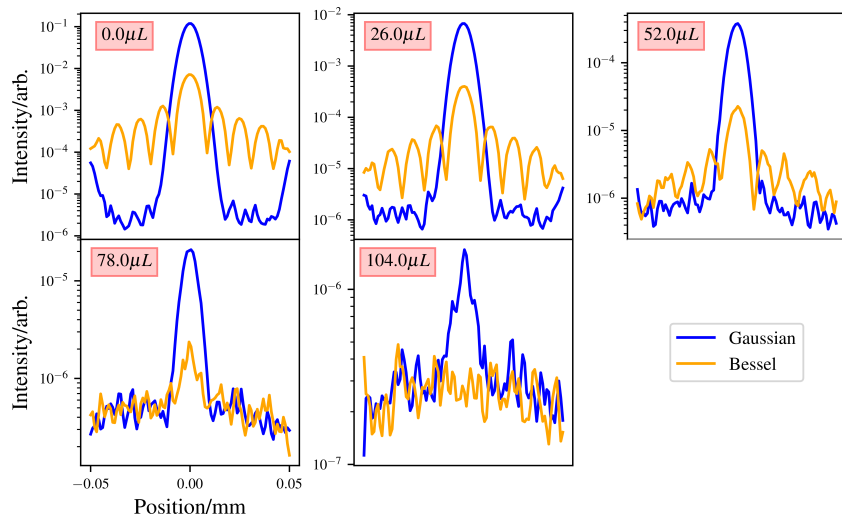


**Figure 4.23:** First comparison of Bessel and Gaussian beams, with equal power used to generate both beams. Plots taken at the bottom of the simulated medium.

scattering. To achieve this the Bessel beam was given  $\sim 15\times$  the power given to the Gaussian beam. The results of this comparison are illustrated in Fig. 4.24.

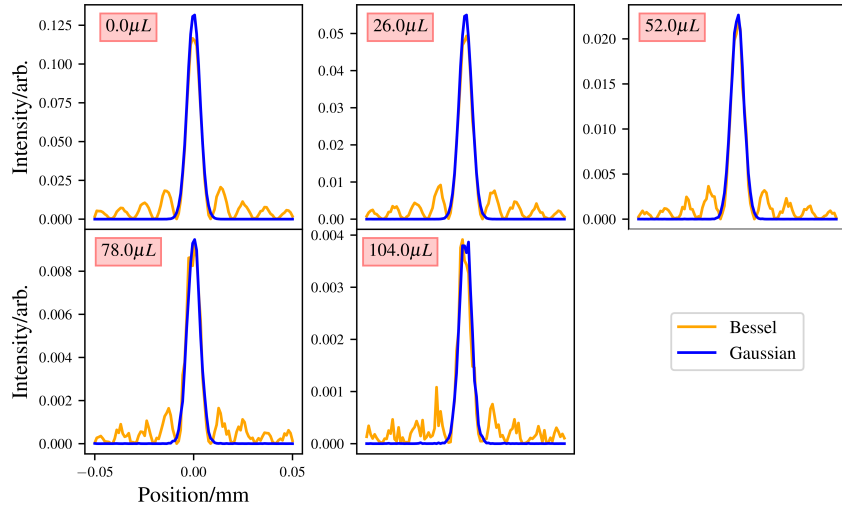


**Figure 4.24:** Second comparison of Bessel and Gaussian beams for the case where the power given to each beam, yields the same maximum at the Gaussian beams focus. These plots are taken from the Gaussian beams focus.

These results show as expected that the Bessel beam now performs comparably with the Gaussian beam in lower scattering media, with a drop off in performance in the higher scattering media.

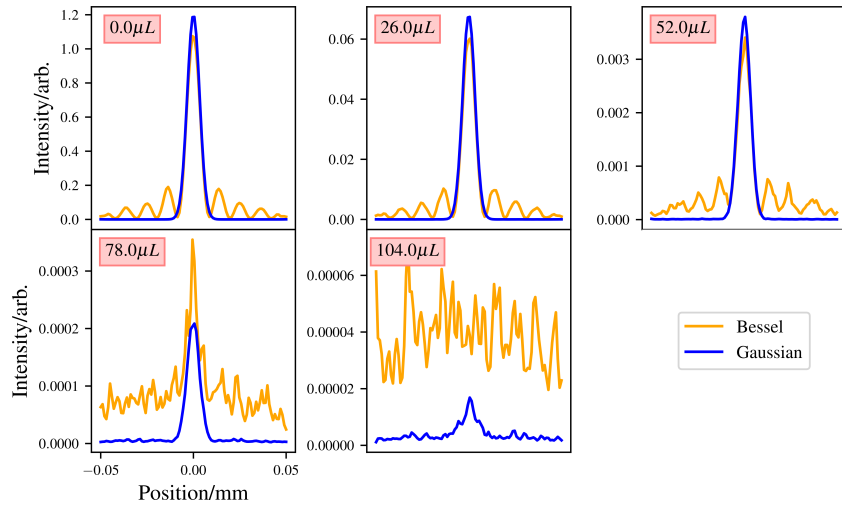


**Figure 4.25:** Comparisons of unequal powered beams at the bottom of scattering medium.

### 4.6.1 Discussion

For equal power beams in the previous section, Gaussian beams perform “better” in the highly scattering mediums. Though this is expected due to the Bessel beams property that the power in the beam is spread evenly over its rings. Thus, the power in the central lobe is much less than that of the Gaussian beam.

To give a slightly more fair comparison of intensity in the central lobes of the beams, the Bessel beam was given  $15\times$  more power than the Gaussian beam. This allows a better comparison between the Gaussian beams’ core and the Bessel beam’s core and gives a more comparable intensity between the beams at the location of the Gaussian beams focus. In this case, the Bessel beam appears to perform better in a highly scattering medium, as shown in Fig. 4.25. The Bessel beam shows comparable intensity with the Gaussian beam in the first three mediums, though the Gaussian beam out performs the Bessel beam in the higher scattering media. It would appear that the Bessel beams self-healing property does not help a Bessel beam propagate through a highly scattering medium. Figure 4.26 shows how the Bessel beam may become degraded due to scattering. As photons propagate though the medium they interfere with one another constructively and destructively to form a Bessel beam. However, if enough photons are scattered, then the Bessel beam becomes degraded and thus no longer is a Bessel beam, as these photons are no longer coherent with the rest of the beam, so they act as a negative factor in the beams formation. Another reason that the “self-healing” property of the Bessel beam does not “save” the beam from scattering is that the “self-healing” is not self-healing. The self-healing in reality is just photons from further off the optical axis forming the Bessel beam further down the optical axis, e.g the photons that are impeded by the blockage are stopped, but the photons that are not impeded form a Bessel beam as expected. If you placed a blockage in front of the Bessel beam larger than the width of the input beam, then the Bessel beam would not form at all.

Bessel beams do have their positives, their self-healing property does help “reform” the beam past small blockages, and their depth of field is superior to an equivalent Gaussian beam, as their central cores is “non-diffractive”.

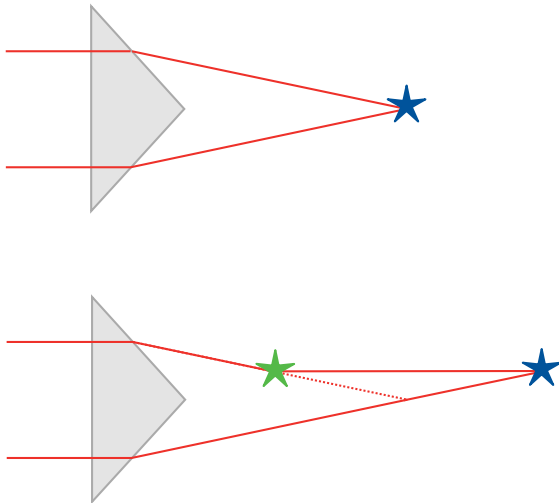


**Figure 4.26:** Illustration of how a Bessel beam becomes degraded due to scattering. Top image shows how two photons propagate through the axicon and constructively interfere to produce a Bessel beam. Bottom image shows how scattering can affect this process.

## 4.7 Conclusion

This chapter has shown that it is possible to transform a traditional particle behaviour MCRT method into a method that allows the simulation of quasi-wave/particle behaviour of photons. This is achieved by introducing two principles to the algorithm: the tracking of the complex phase of each packets and the Huygens-Fresnel principle. The tracking of the complex phase of each packet allows interference of the quasi-wave/particles to be simulated. The Huygens-Fresnel principle allows diffraction to be accurately modelled.  $\varphi MC$  has been thoroughly validated against several experiments where modelling the wave behaviour of light is vital to the experiment. Alongside the above, presented in this chapter is the modelling of complex beam types: Gaussian and Bessel beams. Both beam types have been validated against both theoretical and experimental results. Finally, Gaussian beams and Bessel beams were compared with one another in a highly scattering medium, where Bessel beams appear to give better performance. However,  $\varphi MC$  is not a silver bullet for modelling these complex beams in a scattering medium. Depending on the problem at hand, the computational load can be excessive. For example, if you want to know the intensity of the beam at all locations though a large ( $> 1mm^3$ ) scattering medium with a complex 3D structure, then the time taken to get a good signal to noise ration may be computationally prohibitive. Though it is expected that in most cases the intensity is not needed at all locations in a medium, and an image is all that is need to be calculated, then even in a complex 3D structure  $\varphi MC$  should perform better than the methods listed at the start of this chapter<sup>¶</sup>. Where  $\varphi MC$  excels is that it can accurately model scattering effects on the propagation of complex beams through scattering media.

---

<sup>¶</sup>Though to achieve better performance with the current code, adaptive mesh grids would have to be implemented.



# Bibliography

- [1] N. Metropolis. The beginning of the Monte Carlo method. *Los Alamos Science*, 15:125–130, 1987.
- [2] R. Eckhardt. Stan Ulam, John von Neumann, and the Monte Carlo method. *Los Alamos Science*, 15:131–136, 1987.
- [3] H.L Anderson. Metropolis, Monte Carlo, and the MANIAC. *Los Alamos Science*, 14:96–108, 1986.
- [4] S. Ulam, R.D Richtmyer, and J. Von Neumann. Statistical methods in neutron diffusion. *LAMS-551, Los Alamos National Laboratory*, pages 1–22, 1947.
- [5] W.H Ellett, A.B Callahan, and G.L Brownell. Gamma-ray dosimetry of internal emitters. monte carlo calculations of absorbed dose from point sources. *The British journal of radiology*, 37(433):45–52, 1964.
- [6] B.C Wilson and G. Adam. A monte carlo model for the absorption and flux distributions of light in tissue. *Medical physics*, 10(6):824–830, 1983.
- [7] L. Wang, S.L Jacques, and L. Zheng. Mcmlmonte carlo modeling of light transport in multi-layered tissues. *Computer methods and programs in biomedicine*, 47(2):131–146, 1995.
- [8] H. Key, E.R Davies, P.C Jackson, and P.N.T Wells. Monte carlo modelling of light propagation in breast tissue. *Physics in medicine & biology*, 36(5):591, 1991.
- [9] I.R.M Barnard, P. Tierney, C.L Campbell, L. McMillan, H. Moseley, E. Eadie, C.T.A Brown, and K. Wood. Quantifying direct dna damage in the basal layer of skin exposed to uv radiation from sunbeds. *Photochemistry and photobiology*, 94(5):1017–1025, 2018.
- [10] D.J Smithies and P.H Butler. Modelling the distribution of laser light in port-wine stains with the monte carlo method. *Physics in Medicine & Biology*, 40(5):701, 1995.
- [11] C.L Campbell, K. Wood, R.M. Valentine, C.T.A Brown, and H. Moseley. Monte carlo modelling of daylight activated photodynamic therapy. *Physics in Medicine & Biology*, 60(10):4059, 2015.
- [12] A. El Saddik. Digital twins: The convergence of multimedia technologies. *IEEE MultiMedia*, 25(2):87–92, 2018.
- [13] H. van Houten. The rise of the digital twin: how healthcare can benefit. In <https://www.philips.com/a-w/about/news/archive/blogs/innovation-matters/20180830-the-rise-of-the-digital-twin-how-healthcare-can-benefit.html>. Philips, Aug 2018.

- [14] P. Andreo. Monte carlo simulations in radiotherapy dosimetry. *Radiation Oncology*, 13(1):121, 2018.
- [15] P. Andreo. Monte carlo techniques in medical radiation physics. *Physics in Medicine & Biology*, 36(7):861, 1991.
- [16] E.D Cashwell and C.J Everett. A practical manual on the monte carlo method for random walk problems. 1959.
- [17] D.W.O Rogers and A.F Bielajew. Monte carlo techniques of electron and photon transport for radiation dosimetry. *The dosimetry of ionizing radiation*, 3:427–539, 1990.
- [18] L. Badger. Lazzarini’s lucky approximation of  $\pi$ . *Mathematics Magazine*, 67(2):83–91, 1994.
- [19] P. Beckmann. *A history of Pi*. St. Martin’s Griffin, 2015.
- [20] G.L Buffon. *Histoire naturelle générale et particulière*, volume 18. de l’Imprimerie de F. Dufart, 1785.
- [21] P. Jäckel. *Monte Carlo methods in finance*. J. Wiley, 2002.
- [22] D.B Hertz. Risk analysis in capital investment. *Harvard Business Review*, 42(1):95–106, 1964.
- [23] J.V Wall and C.R Jenkins. *Practical statistics for astronomers*. Cambridge University Press, 2012.
- [24] J.T Kajiya. The rendering equation. *SIGGRAPH Comput. Graph.*, 20(4):143–150, August 1986.
- [25] R.L Cook, T. Porter, and L Carpenter. Distributed ray tracing. *SIGGRAPH Comput. Graph.*, 18(3):137–145, January 1984.
- [26] T.P Robitaille. Hyperion: an open-source parallelized three-dimensional dust continuum radiative transfer code. *Astronomy & Astrophysics*, 536:A79, 2011.
- [27] T. Harries. Torus: Radiation transport and hydrodynamics code. *Astrophysics Source Code Library*, 2014.
- [28] R.M Valentine, C.T.A Brown, K. Wood, H. Moseley, and S. Ibbotson. Monte carlo modeling of in vivo protoporphyrin ix fluorescence and singlet oxygen production during photodynamic therapy for patients presenting with superficial basal cell carcinomas. *Journal of Biomedical Optics*, 16(4):048002, 2011.
- [29] M. Pharr, W. Jakob, and G. Humphreys. *Physically based rendering: From theory to implementation*. Morgan Kaufmann, 2016.
- [30] K. Wood and R.J Reynolds. A model for the scattered light contribution and polarization of the diffuse  $h\alpha$  galactic background. *The Astrophysical Journal*, 525(2):799, 1999.
- [31] D.W.O Rogers, B.A Faddegon, G.X Ding, C-M. Ma, J. We, and T.R Mackie. Beam: a monte carlo code to simulate radiotherapy treatment units. *Medical physics*, 22(5):503–524, 1995.

- [32] B.C Wilson and G. Adam. A monte carlo model for the absorption and flux distributions of light in tissue. *Medical Physics*, 10(6):824–830, 1983.
- [33] L.V Wang and H. Wu. *Biomedical optics: principles and imaging*. John Wiley & Sons, 2012.
- [34] S. Chandrasekhar. *Radiative transfer*. Courier Corporation, 2013.
- [35] V.DMZ Barbarić-Mikočević and K. Itrić. Kubelka-munk theory in describing optical properties of paper (i). *Technical Gazette*, 18(1):117–124, 2011.
- [36] M. Jasiński. Modelling of light and human skin interaction using kubelka-munk theory. *Scientific Research of the Institute of Mathematics and Computer Science*, 10(1):71–81, 2011.
- [37] WF. Cheong, S.A Prahl, and A.J Welch. A review of the optical properties of biological tissues. *IEEE journal of quantum electronics*, 26(12):2166–2185, 1990.
- [38] M. Gabriela. Mathematical methods in biomedical optics. *ISRN Biomedical Engineering*, 2013, 2013.
- [39] S.A Prahl. Light transport in tissue. 1990.
- [40] R. Graaff, J.G Aarnoudse, F.F.M de Mul, and H.W Jentink. Similarity relations for anisotropic scattering in absorbing media. *Optical engineering*, 32(2):244–253, 1993.
- [41] S.A Yoon, G.and Prahl and A.J Welch. Accuracies of the diffusion approximation and its similarity relations for laser irradiated biological media. *Applied Optics*, 28(12):2250–2255, 1989.
- [42] T.P Robitaille. On the modified random walk algorithm for monte-carlo radiation transfer. *Astronomy & Astrophysics*, 520:A70, 2010.
- [43] M. Min, C.P Dullemond, C. Dominik, A. de Koter, and J.W Hovenier. Radiative transfer in very optically thick circumstellar disks. *Astronomy & Astrophysics*, 497(1):155–166, 2009.
- [44] S.L Jacques. Origins of tissue optical properties in the uva, visible, and nir regions. *OSA TOPS on advances in optical imaging and photon migration*, 2:364–369, 1996.
- [45] S.L Jacques. Optical properties of biological tissues: a review. *Physics in Medicine & Biology*, 58(11):R37, 2013.
- [46] T. Lister, P.A Wright, and P.H Chappell. Optical properties of human skin. *Journal of biomedical optics*, 17(9):090901, 2012.
- [47] L.G Henyey and J.L Greenstein. Diffuse radiation in the galaxy. *The Astrophysical Journal*, 93:70–83, 1941.
- [48] S.L Jacques, C.A Alter, and S.A Prahl. Angular dependence of hene laser light scattering by human dermis. *Lasers Life Sci*, 1(4):309–333, 1987.
- [49] J.M Dixon, M. Taniguchi, and J.S Lindsey. Photochemcad 2: A refined program with accompanying spectral databases for photochemical calculations. *Photochemistry and photobiology*, 81(1):212–213, 2005.

- [50] S. Prahl. Photochemcad spectra. <https://omlc.org/spectra/PhotochemCAD/index.html>, 2017. [Online; Last accessed 4-February-2019].
- [51] D.J. Segelstein. *The complex refractive index of water*. PhD thesis, University of Missouri-Kansas City, 1981.
- [52] R.M Pope and E.S Fry. Absorption spectrum (380–700 nm) of pure water. ii. integrating cavity measurements. *Applied optics*, 36(33):8710–8723, 1997.
- [53] R.L.P van Veen, H.J.C.M Sterenborg, A. Pifferi, A. Torricelli, and R. Cubeddu. Determination of vis-nir absorption coefficients of mammalian fat, with time-and spatially resolved diffuse reflectance and transmission spectroscopy. In *Biomedical Topical Meeting*, page SF4. Optical Society of America, 2004.
- [54] I.S Saidi et al. *Transcutaneous optical measurement of hyperbilirubinemia in neonates*. PhD thesis, Rice University, 1992.
- [55] J.A Iglesias-Guitian, C. Aliaga, A. Jarabo, and D. Gutierrez. A biophysically-based model of the optical properties of skin aging. In *Computer Graphics Forum*, volume 34, pages 45–55. Wiley Online Library, 2015.
- [56] A.N Bashkatov, E.A Genina, and V.V Tuchin. Optical properties of skin, subcutaneous, and muscle tissues: a review. *Journal of Innovative Optical Health Sciences*, 4(01):9–38, 2011.
- [57] T. Sarna and H.A Swartz. The physical properties of melanins. *The pigmentary system: physiology and pathophysiology*, pages 311–341, 2006.
- [58] L.B. Lucy. Computing radiative equilibria with monte carlo techniques. *Astronomy and Astrophysics*, 344:282–288, 1999.
- [59] M. Metcalf, J. Reid, and M. Cohen. *Modern Fortran Explained*. Oxford University Press, 2011.
- [60] J.E Bjorkman and K. Wood. Radiative equilibrium and temperature correction in monte carlo radiation transfer. *The Astrophysical Journal*, 554(1):615, 2001.
- [61] W. Gropp, E. Lusk, and A. Skjellum. *Using MPI: Portable Parallel Programming with the Message-Passing Interface*. Scientific and Engineering Computation. MIT Press, 2014.
- [62] W. Gropp, T. Hoefler, R. Thakur, and E. Lusk. *Using advanced MPI: Modern features of the message-passing interface*. MIT Press, 2014.
- [63] G.M. Amdahl. Validity of the single processor approach to achieving large scale computing capabilities. In *Proceedings of the April 18-20, 1967, Spring Joint Computer Conference*, pages 483–485. ACM, 1967.
- [64] J. Bjorkman. Monte carlo radiation transfer. Presented as SAMCSS 2013, 2013.
- [65] C.M Gardner, S.L Jacques, and A.J Welch. Fluorescence and reflectance spectra specify intrinsic fluorescence spectrum corrected for tissue optics distortion. In *Advances in Fluorescence Sensing Technology*, volume 1885, pages 122–129. International Society for Optics and Photonics, 1993.

- [66] S.L Jacques, R. Joseph, and G. Gofstein. How photobleaching affects dosimetry and fluorescence monitoring of pdt in turbid media. In *Optical Methods for Tumor Treatment and Detection: Mechanisms and Techniques in Photodynamic Therapy II*, volume 1881, pages 168–180. International Society for Optics and Photonics, 1993.
- [67] D. Manstein, G.S. Herron, R.K. Sink, H. Tanner, and R.R. Anderson. Fractional photothermolysis: a new concept for cutaneous remodeling using microscopic patterns of thermal injury. *Lasers in Surgery and Medicine: The Official Journal of the American Society for Laser Medicine and Surgery*, 34(5):426–438, 2004.
- [68] S. Amini-Nik, D. Kraemer, M.L. Cowan, K. Gunaratne, P. Nadesan, B.A. Alman, and R.J. Dwayne Miller. Ultrafast mid-ir laser scalpel: protein signals of the fundamental limits to minimally invasive surgery. *PLoS One*, 5(9):e13053, 2010.
- [69] O.T. Tan, K. Sherwood, and B.A. Gilchrest. Treatment of children with port-wine stains using the flashlamp-pulsed tunable dye laser. *New England Journal of Medicine*, 320(7):416–421, 1989.
- [70] M. Kuperman-Beade, V.J. Levine, and R. Ashinoff. Laser removal of tattoos. *American Journal of Clinical Dermatology*, 2(1):21–25, 2001.
- [71] S.H. Liew. Laser hair removal. *American Journal of Clinical Dermatology*, 3(2):107–115, 2002.
- [72] C.A. Hardaway and E.V. Ross. Nonablative laser skin remodeling. *Dermatologic Clinics*, 20(1):97–111, 2002.
- [73] S.M. Shapshay, M.S. Strong, G.W. Anastasi, and C.W. Vaughan. Removal of rhinophyma with the carbon dioxide laser: a preliminary report. *Archives of Otolaryngology*, 106(5):257–259, 1980.
- [74] R. Valcavi, F. Riganti, A. Bertani, D. Formisano, and C.M. Pacella. Percutaneous laser ablation of cold benign thyroid nodules: a 3-year follow-up study in 122 patients. *Thyroid*, 20(11):1253–1261, 2010.
- [75] M. Hædersdal, F.H. Sakamoto, W.A. Farinelli, A.G. Doukas, J. Tam, and R.R. Anderson. Fractional CO<sub>2</sub> laser-assisted drug delivery. *Lasers in Surgery and Medicine: The Official Journal of the American Society for Laser Medicine and Surgery*, 42(2):113–122, 2010.
- [76] M.R. Alexiades-Armenakas, J.S. Dover, and K.A. Arndt. The spectrum of laser skin resurfacing: nonablative, fractional, and ablative laser resurfacing. *Journal of the American Academy of Dermatology*, 58(5):719–737, 2008.
- [77] D.V Widder. *The Heat Equation*, volume 67. Academic Press, 1976.
- [78] N. Ozisik. *Finite Difference Methods in Heat Transfer*. CRC press, 1994.
- [79] Alma Lasers GmbH. *PixelCO<sub>2</sub> Operator's Manual*. Alma Lasers GmbH.
- [80] S. Ristov, R. Prodan, M. Gusev, and K. Skala. Superlinear speedup in hpc systems: Why and when? In *Computer Science and Information Systems (FedCSIS), 2016 Federated Conference on*, pages 889–898. IEEE, 2016.
- [81] A.J Welch, M.J.C Van Gemert, et al. *Optical-thermal Response of Laser-irradiated Tissue*, volume 2. Springer, 2011.

- [82] N.T. Wright. Quantitative models of thermal damage to cells and tissues. In *Heat Transfer and Fluid Flow in Biological Processes*, pages 59–76. Elsevier, 2015.
- [83] M.H. Niemz. *Laser-tissue interactions: fundamentals and applications*. Springer Science & Business Media, 2013.
- [84] F. Petrella, S. Cavaliere, and L. Spaggiari. Popcorn effect. *Journal of Bronchology & Interventional Pulmonology*, 20(2):193–194, 2013.
- [85] R.M. Verdaasdonk, C. Borst, and M.J.C. Van Gemert. Explosive onset of continuous wave laser tissue ablation. *Physics in Medicine & Biology*, 35(8):1129, 1990.
- [86] W. Husinsky, G. Grabner, I. Baumgartner, F. Skorpik, S. Mitterer, and T. Temmel. Mechanisms of laser ablation of biological tissue. In *Desorption Induced by Electronic Transitions DIET IV*, pages 362–367. Springer, 1990.
- [87] M.S Kitai, V.L Popkov, V.A Semchischen, and A.A Kharizov. The physics of uv laser cornea ablation. *IEEE journal of quantum electronics*, 27(2):302–307, 1991.
- [88] A.A Oraevsky, R.O Esenaliev, and V.S Letokhov. Pulsed laser ablation of biological tissue: Review of the mechanisms. In *Laser Ablation Mechanisms and Applications*, pages 112–122. Springer, 1991.
- [89] A. Vogel and V. Venugopalan. Mechanisms of pulsed laser ablation of biological tissues. *Chemical Reviews*, 103(2):577–644, 2003.
- [90] G. Koren and J.T.C Yeh. Emission spectra, surface quality, and mechanism of excimer laser etching of polyimide films. *Applied Physics Letters*, 44(12):1112–1114, 1984.
- [91] J.E Andrew, P.E Dyer, D. Forster, and P.H Key. Direct etching of polymeric materials using a xocl laser. *Applied Physics Letters*, 43(8):717–719, 1983.
- [92] A.L. McKenzie. Physics of thermal processes in laser-tissue interaction. *Physics in Medicine & Biology*, 35(9):1175, 1990.
- [93] A.L. McKenzie. A three-zone model of soft-tissue damage by a CO<sub>2</sub> laser. *Physics in Medicine & Biology*, 31(9):967, 1986.
- [94] B. Majaron, P. Plestenjak, and M. Lukač. Thermo-mechanical laser ablation of soft biological tissue: modeling the micro-explosions. *Applied Physics B*, 69(1):71–80, 1999.
- [95] M. Gerstmann, Y. Linenberg, A. Katzir, and S. Akselrod. Char formation in tissue irradiated with a CO<sub>2</sub> laser: model and simulations. *Optical Engineering*, 33(7):2343–2352, 1994.
- [96] A. Sagi, A. Avidor-Zehavi, A. Shitzer, M. Gerstmann, S. Akselrod, and A. Katzir. Heating of biological tissue by laser irradiation: temperature distribution during laser ablation. *Opt. Eng.*, 31(7):1425–1431, 1992.
- [97] J.A. Pearce. Relationship between arrhenius models of thermal damage and the cem 43 thermal dose. In *Energy-based Treatment of Tissue and Assessment V*, volume 7181, page 718104. International Society for Optics and Photonics, 2009.
- [98] F.C. Jr Hendriques. Studies of thermal injury; the predictability and the significance of thermally induced rate processes leading to irreversible epidermal injury. *Arch. Pathol.(Chic)*, 43:489–502, 1947.

- [99] S.C. Jiang, N. Ma, H.J. Li, and X.X. Zhang. Effects of thermal properties and geometrical dimensions on skin burn injuries. *Burns*, 28(8):713–717, 2002.
- [100] K.R. Diller and L.J. Hayes. A finite element model of burn injury in blood-perfused skin. *Journal of Biomechanical Engineering*, 105(3):300–307, 1983.
- [101] J. Zhang and X. Zhang. Dynamic modeling of tissue ablation with continuous wave co<sub>2</sub> laser. In *2007 1st International Conference on Bioinformatics and Biomedical Engineering*, pages 1057–1060. IEEE, 2007.
- [102] I.V. Meglinski and S.J. Matcher. Quantitative assessment of skin layers absorption and skin reflectance spectra simulation in the visible and near-infrared spectral regions. *Physiological Measurement*, 23(4):741, 2002.
- [103] B.R. Loiola, H.R.B. Orlande, and G.S. Dulikravich. Thermal damage during ablation of biological tissues. *Numerical Heat Transfer, Part A: Applications*, pages 1–17, 2018.
- [104] V. Casalegno, P. Vavassori, M. Valle, M. Ferraris, M. Salvo, and G. Pintsuk. Measurement of thermal properties of a ceramic/metal joint by laser flash method. *Journal of Nuclear Materials*, 407(2):83–87, 2010.
- [105] E. MacCormack, A. Mandelis, M. Munidasa, B. Farahbakhsh, and H. Sang. Measurements of the thermal diffusivity of aluminum using frequency-scanned, transient, and rate window photothermal radiometry. theory and experiment. *International journal of thermophysics*, 18(1):221–250, 1997.
- [106] Alma Lasers. Pixel CO<sub>2</sub>, 2018.
- [107] M. Lapidoth, S. Halachmi, S. Cohen, and D.B. Amitai. Fractional co<sub>2</sub> laser in the treatment of facial scars in children. *Lasers in Medical Science*, 29(2):855–857, 2014.
- [108] M.A. Trelles, M. Shohat, and F. Urdiales. Safe and effective one-session fractional skin resurfacing using a carbon dioxide laser device in super-pulse mode: a clinical and histologic study. *Aesthetic Plastic Surgery*, 35(1):31–42, 2011.
- [109] E. Kohl, J. Meierhöfer, M. Koller, F. Zeman, L. Groesser, S. Karrer, U. Hohenleutner, M. Landthaler, and S. Hohenleutner. Fractional carbon dioxide laser resurfacing of rhytides and photoaged skin—a prospective clinical study on patient expectation and satisfaction. *Lasers in Surgery and Medicine*, 47(2):111–119, 2015.
- [110] J. Baumgartl, M. Mazilu, and K. Dholakia. Optically mediated particle clearing using airy wavepackets. *Nature photonics*, 2(11):675, 2008.
- [111] D.B Ruffner and D.G Grier. Optical conveyors: a class of active tractor beams. *Physical review letters*, 109(16):163903, 2012.
- [112] T. Vettenburg, H.I.C Dalgarno, J. Nylk, C. Coll-Lladó, D.E.K Ferrier, T. Čižmár, F.J Gunn-Moore, and K. Dholakia. Light-sheet microscopy using an airy beam. *Nature methods*, 11(5):541, 2014.
- [113] N.B Simpson, L. Allen, and M.J Padgett. Optical tweezers and optical spanners with laguerre–gaussian modes. *Journal of modern optics*, 43(12):2485–2491, 1996.
- [114] A.K Glaser, Y. Chen, and J.T.C Liu. Fractal propagation method enables realistic optical microscopy simulations in biological tissues. *Optica*, 3(8):861–869, 2016.

- [115] A. Elmaklizi, D. Reitzle, A.R Brandes, and A. Kienle. Penetration depth of focused beams in highly scattering media investigated with a numerical solution of maxwells equations in two dimensions. *Journal of biomedical optics*, 20(6):065007, 2015.
- [116] J. Van Roey, J. Van der Donk, and P.E Lagasse. Beam-propagation method: analysis and assessment. *Josa*, 71(7):803–810, 1981.
- [117] B.H Hokr, J.N Bixler, G. Elpers, B. Zollars, R.J Thomas, V.V Yakovlev, and M.O Scully. Modeling focusing gaussian beams in a turbid medium with monte carlo simulations. *Optics express*, 23(7):8699–8705, 2015.
- [118] J. Arnaud. Representation of gaussian beams by complex rays. *Applied optics*, 24(4):538–543, 1985.
- [119] J.E Harvey, R.G Irvin, and R.N Pfisterer. Modeling physical optics phenomena by complex ray tracing. *Optical Engineering*, 54(3):035105, 2015.
- [120] N.G Worku, R. Hambach, and H. Gross. Decomposition of a field with smooth wavefront into a set of gaussian beams with non-zero curvatures. *JOSA A*, 35(7):1091–1102, 2018.
- [121] F. Cai and S. He. Electric field monte carlo simulation of focused stimulated emission depletion beam, radially and azimuthally polarized beams for in vivo deep bioimaging. *Journal of biomedical optics*, 19(1):011022, 2014.
- [122] F.A Volpe, P-D. Létourneau, and A. Zhao. Huygens–fresnel wavefront tracing. *Computer Physics Communications*, 212:123–131, 2017.
- [123] C. Mignon, A.H. Rodriguez, J.A Palero, B. Varghese, and M. Jurna. Fractional laser photothermolysis using bessel beams. *Biomedical optics express*, 7(12):4974–4981, 2016.
- [124] S. Peter, P. Modregger, M.K Fix, W. Volken, D. Frei, P. Manser, and M. Stampanoni. Combining monte carlo methods with coherent wave optics for the simulation of phase-sensitive x-ray imaging. *Journal of synchrotron radiation*, 21(3):613–622, 2014.
- [125] J.R Mahan, N.Q Vinh, V.X Ho, and N.B Munir. Monte carlo ray-trace diffraction based on the huygens–fresnel principle. *Applied optics*, 57(18):D56–D62, 2018.
- [126] M. Mout, M. Wick, F. Bociort, J. Petschulat, and P. Urbach. Simulating multiple diffraction in imaging systems using a path integration method. *Applied optics*, 55(14):3847–3853, 2016.
- [127] D.G Fischer, S.A Prahl, and D.D Duncan. Monte carlo modeling of spatial coherence: free-space diffraction. *JOSA A*, 25(10):2571–2581, 2008.
- [128] C. Huygens. *Treatise on light*. tredition, 2012.
- [129] E. Hecht. *Optics*. Pearson Education, Incorporated, 2017.
- [130] C. Huygens, T. Young, A.J. Fresnel, and F. Arago. *The wave theory of light: memoirs of Huygens, Young and Fresnel*, volume 15. American Book Company, 1900.
- [131] A. Fresnel. Mémoire sur la diffraction de la lumière. *da p. 339 a p. 475: 1 tav. ft; AQ 210*, page 339, 1819.
- [132] G. Kirchhoff. Ann. d. physik. (2), 18:663, 1883.

- [133] M. Born, E. Wolf, and A.B. Bhatia. *Principles of Optics: Electromagnetic Theory of Propagation, Interference and Diffraction of Light*. Cambridge University Press, 2000.
- [134] J.W. Goodman. *Introduction to Fourier Optics*. W. H. Freeman, 2017.
- [135] P.W. Milonni and J.H. Eberly. *Laser Physics*. Wiley, 2010.
- [136] Thorlabs Inc. UV fused silica plano-convex lenses. <https://www.thorlabs.com/thorproduct.cfm?partnumber=LA4249>, 2019. [Online; accessed 18-April-2019].
- [137] J.M. Durnin, J.J. Miceli Jr, and J.H. Eberly. Diffraction-free beams. *Physical review letters*, 58(15):1499, 1987.
- [138] J.M. Durnin. Exact solutions for nondiffracting beams. I. the scalar theory. *JOSA A*, 4(4):651–654, 1987.
- [139] D. McGloin and K. Dholakia. Bessel beams: diffraction in a new light. *Contemporary Physics*, 46(1):15–28, 2005.
- [140] D. DeBeer, S.R Hartmann, and R. Friedberg. Comment on “diffraction-free beams”. *Physical review letters*, 59(22):2611, 1987.
- [141] J.E Harvey and J.L Forgham. The spot of arago: new relevance for an old phenomenon. *American journal of Physics*, 52(3):243–247, 1984.
- [142] J. Durnin, J.J Miceli, and J.H Eberly. Reply to d. debeer, sr hartmann and r. friedberg. *Phys. Rev. Lett.*, 59:2612, 1987.
- [143] P. Sprangle and B. Hafizi. Comment on nondiffracting beams. *Physical review letters*, 66(6):837, 1991.
- [144] J. Durnin, J.J Miceli Jr, and J.H Eberly. Durnin, miceli, and eberly reply. *Physical review letters*, 66(6):838, 1991.
- [145] T. Čižmár. *Optické pasti generované netradičními svazky*. PhD thesis, Masarykova univerzita, Přírodovědecká fakulta, 2006.
- [146] F. Merola, S. Coppola, V. Vespi, S. Grilli, and P. Ferraro. Characterization of bessel beams generated by polymeric microaxicons. *Measurement Science and Technology*, 23(6):065204, 2012.
- [147] B. Aernouts, E. Zamora-Rojas, R. Van Beers, R. Watté, L. Wang, M. Tsuta, J. Lamertyn, and W. Saeys. Supercontinuum laser based optical characterization of intralipid® phantoms in the 500–2250 nm range. *Optics express*, 21(26):32450–32467, 2013.
- [148] M.I Mishchenko. independent and dependent scattering by particles in a multi-particle group. *OSA Continuum*, 1(1):243–260, 2018.
- [149] M.Z. Vardaki, B. Gardner, N. Stone, and P. Matousek. Studying the distribution of deep raman spectroscopy signals using liquid tissue phantoms with varying optical properties. *Analyst*, 140(15):5112–5119, 2015.
- [150] P. Di Ninni, F. Martelli, and G. Zaccanti. Effect of dependent scattering on the optical properties of intralipid tissue phantoms. *Biomedical optics express*, 2(8):2265–2278, 2011.

- [151] R. Michels, F. Foschum, and A. Kienle. Optical properties of fat emulsions. *Optics Express*, 16(8):5907–5925, 2008.
- [152] V. Garcés-Chávez, K. Volke-Sepulveda, S. Chávez-Cerda, W. Sibbett, and K. Dholakia. Transfer of orbital angular momentum to an optically trapped low-index particle. *Physical Review A*, 66(6):063402, 2002.
- [153] V. Garcés-Chávez, D. McGloin, M.J Padgett, W. Dultz, H. Schmitzer, and K. Dholakia. Observation of the transfer of the local angular momentum density of a multiringed light beam to an optically trapped particle. *Physical review letters*, 91(9):093602, 2003.
- [154] X. Wei, C. Liu, L. Niu, Z. Zhang, K. Wang, Z. Yang, and J. Liu. Generation of arbitrary order bessel beams via 3d printed axicons at the terahertz frequency range. *Applied optics*, 54(36):10641–10649, 2015.
- [155] S.N. Khonina, V.V. Kotlyar, V.A. Soifer, M.V. Shinkaryev, and G.V. Uspleniev. Trochoson. *Optics Communications*, 91(3-4):158–162, 1992.
- [156] V.V. Kotlyar, A.A. Kovalev, S.N. Khonina, R.V. Skidanov, V.A. Soifer, H. Elfstrom, N. Tossavainen, and J. Turunen. Diffraction of conic and gaussian beams by a spiral phase plate. *Applied optics*, 45(12):2656–2665, 2006.
- [157] S. Topuzoski and L. Janicjevic. Conversion of high-order laguerre–gaussian beams into bessel beams of increased, reduced or zeroth order by use of a helical axicon. *Optics Communications*, 282(17):3426–3432, 2009.
- [158] S. Qiong-Ge, Z. Ke-Ya, F. Guang-Yu, L. Zheng-Jun, and L. Shu-Tian. Generalization and propagation of spiraling bessel beams with a helical axicon. *Chinese Physics B*, 21(1):014208, 2012.